# Plumes in two-layer stratified fluid with and without background rotation

by

## Yongxing Ma

A thesis submitted in partial fulfillment of the requirements for the degree of

Doctor of Philosophy

Department of Earth and Atmospheric Sciences

University of Alberta

# Abstract

This thesis experimentally and numerically examines the physical processes of a turbulent descending (ascending) plume in a two-layer stratified ambient fluid with and without background rotation. At the initial time, $t = 0$, the plume either penetrates through or spreads along the ambient interface. Whether one or the other behaviour occurs is determined by the ratio of the reduced gravity of the descending (ascending) plume at the interface as compared to the reduced gravity between the upper and lower ambient layers. In either case, transition processes are explored, in which the plume either evolves, for larger $t$, from penetration to spreading or vice versa.

The first component of the thesis investigates a line-source plume descending in a time-evolving two-layer stratified ambient fluid. The plume can penetrate through the interface for small $t$ when the upper layer is thin. However, over time, this layer thickens due to the outflow from the lower layer within the closed domain. This outflow is counterbalanced by an inflow in the upper layer that keeps the total ambient volume constant. As the upper layer thickens, there is a greater vertical distance over which the plume may entrain light fluid from the upper layer. The plume therefore becomes more and more diluted. A criterion is found to determine whether the plume will ultimately evolve from a penetrating to a spreading regime. A plume splitting phenomenon, namely a partial discharge of plume fluid along the ambient interface, is observed to occur during the transition process. This study provides new information for designing ventilation systems and marine outfall diffusers.

The second component of the thesis examines a point-source plume descend-

ing in a two-layer stratified ambient fluid with background rotation. Affected by the background rotation, the plume is observed to precess anticyclonically. The source and initial conditions are set so that the plume initially spreads at the interface of the two-layer ambient fluid instead of penetrating through it. The Coriolis force acts to constrain the discharged plume fluid, which forms a slowly expanding lens below the plume source. A transition from initial spreading to eventual penetration occurs due to the re-entrainment of this lens fluid back into the plume. The front position of the lens is measured from experiments and the relationship between this front position and time is determined. The resulting empirical equations show good agreement with the predictions made by simple scaling theory. Empirical formulae are also derived for the time required for discharged plume fluid to finally penetrate through the ambient interface and descend to depth.

The third component of the thesis revisits the case of a rotating ambient (consisting of either uniform or two-layer density-stratified fluid), but does so using numerical simulations rather than laboratory experiments. To this end, we employ a Large Eddy Simulation (LES) technique. The numerical simulations capture plume precession; both the frequency and polar angle of the precession are measured from the simulation results. The front position of the lens shows good agreement with that from experiments. These fundamental studies of a plume in rotating ambient elucidate the degree to which rotation may accelerate the process of deep vertical convection in the ocean.

*To my late father,*

*for always encouraging me in pursuing higher educations.*

# Acknowledgements

It has been an enjoyable and intensive period of writing this thesis. Many people have helped me throughout this period and four years of my Ph.D. study.

I would first like to express my sincere gratitude to my supervisors Dr. Bruce Sutherland and Dr. Morris Flynn for the continuous support of my Ph.D study, for their patience, immense knowledge and severe attitudes to research. The helpful supervision and assistance from my supervisors are such an important factor that I can successfully accomplish this thesis. To Bruce, thanks for providing me with the lab facilities and multiple hard drives, guiding me in English writing, and treating me drinks in the faculty club. Also to Morris, thanks for providing the experiment supplies and editing this thesis.

My sincere thanks also goes to Dr. Paul Myers, who permitted me to attend their group meeting where I gained more knowledge of oceanography. I want to say thanks to Dr Xianmin Hu for wonderful discussions about the ocean models. I would also like to thank my colleague Shuo Li for helping me fabricating the flanges of the nozzle.

Finally, I am grateful to my mother who alway cares my life so much. I have been staying out home for long time since I went abroad and maybe will not be able to accompany you much in future, but I am and will be always missing you.

# Contents

# List of Tables

# List of Figures

# Chapter 1

# Introduction

## 1.1 Background

The definition of a plume in the scope of this thesis is a vertical motion of a fluid within an ambient fluid being driven by a localized buoyancy force due to density differences. Plumes of different scales broadly exist in industrial and environmental contexts; the smoke rising from chimneys, heating or cooling from the floors or ceilings of buildings and the rising gases within explosive volcanic eruptions are all examples of plumes. Familiar to people's common sense and as in the above examples, plumes are usually turbulent. Through turbulent processes, plumes entrain ambient fluid, which may be either uniform in density or else density-stratified with the ambient density decreasing with height. Because of entrainment, the plume diameter increases and the density of the ascending (descending) plume increases (decreases). A light plume in a uniform ambient can always rise indefinitely if the ambient is unbounded, because the plume density is always smaller than the ambient fluid no matter how much entrainment occurs. However, in the presence of stratification the plume may reach its level of neutral buoyancy and, after a brief overshoot, stop rising vertically.

Besides stratification, another feature of fluids on geophysical scales is rotation. Because the Earth is rotating, the Coriolis force can act to modify the morphology of a plume's motion and also influence the pattern of outflow as-

sociated with fluid discharged by the plume as the plume reaches its neutral density level. In this thesis, turbulent plumes are examined in a two-layer stratified ambient fluid with and without background rotation, with a focus on how time-changing ambient conditions can alter whether a plume penetrates through or spreads at the ambient interface.

## 1.2 Plume studies

Due to the complexities of the Navier-Stokes equations and the turbulent behaviour of plumes, analytical solutions describing the instantaneous motions within the plumes have not been found. However one typically cares primarily about the macroscopic and/or statistically steady properties of turbulent plumes, such as the mean volume fluxes at different heights. Below the progress in understanding the dynamics of plumes in uniform and rotating environments is reviewed.

### 1.2.1 MTT model

In a seminal paper a theoretical model for turbulent plumes was proposed by Morton *et al.* (1956), referred to hereafter as the MTT model. Based on experimental observations of turbulent plumes, MTT made three major assumptions:

1. **Boussinesq approximation:** The maximum density variation between the plume and ambient fluid is small compared with the reference density chosen to be the ambient fluid density at the plume source level.

2. **Self-similarity:** If, at each height, the time-averaged vertical velocity, $w$, and reduced gravity, $g'$, of the plume are normalized with their corresponding centre-line values and the radial coordinate is normalized with the local plume radius, the horizontal distribution of $w$ and $g'$ at different heights follow the same profile. More precisely, evidence from experimental measurements (George *et al.*, 1977; Ramaprian & Chandrasekhara,

2

1989; Paillat & Kaminski, 2014; Ezzamel *et al.*, 2015) and numerical simulations (van Reeuwijk *et al.*, 2016) suggest that the profile is in either case well approximated by a Gaussian distribution. However, for conceptual convenience one often assumes a "top-hat" profile in which properties such as the vertical velocity are assumed to have compact support, i.e. $w$ is finite and constant within the plume but zero everywhere outside.

3. **Entrainment assumption:** The horizontal velocity at the edge of the plume induced by the turbulent entrainment is proportional to the characteristic vertical velocity within the plume at each height, usually taken to be the value at the centre line. Later research found that turbulent entrainment occurs through the two processes of eddy engulfment and nibbling (Mathew & Basu, 2002; Westerweel *et al.*, 2005; Burridge *et al.*, 2017), which are briefly discussed in Appendix A.

### 1.2.2 Filling box process

The MTT model was proposed for a turbulent plume presented in a semi-infinite ambient fluid, where the ambient was unaffected by the plume. Baines & Turner (1969) further considered a scenario of a plume in a confined region filled with an initially uniform density ambient fluid. As the descending (ascending) plume reached the bottom (top/free surface) of the closed region, its fluid spread laterally in the form of a gravity current. As the gravity current reached the side boundaries, a new ambient layer formed consisting of discharged plume fluid whose density was different from that of the initial ambient fluid. As time progressed, the process repeated but now a new and even more dense (buoyant) layer of discharged plume fluid appeared along the boundary. Over time, therefore, the ambient consisted of a diminishing ambient layer of constant density and an accumulating ambient layer whose density varied continuously with height. The dynamics just described is the "filling box" process and its essential details were further elaborated upon by Germeles (1975), Worster & Huppert (1983) and Caulfield & Woods (2002). Examples of the applications of the fill-

ing box process include modelling the natural ventilation of buildings (Linden *et al.*, 1990; Kaye & Flynn, 2012) and ocean overturning circulations (Mullarney *et al.*, 2004; Hughes & Griffiths, 2006). In addition to such inter-dependent processes between the plume and the ambient fluid, the stratification of the ambient fluid can also be time-dependent due to external influences, e.g. inflows into and outflows out of the domain. While well-studied in the context of steady processes, plume behaviour in a time-evolving stratified ambient fluid generally has not been so well examined.

### 1.2.3   Plumes in stratified fluid

Even though most extensions of the MTT model, including the filling-box model (Baines & Turner, 1969), assumed an initially uniform ambient fluid, some researchers have investigated plumes in initially stably stratified ambient fluids. Unlike plume evolution in a semi-infinite uniform ambient fluid, in which a light (dense) plume can rise (descend) indefinitely, ambient stratification alters the plume from ascending (descending) to horizontally spreading at a neutral density level. The plume can overshoot this level and then rebound in the form of a fountain. Valuable experimental and theoretical studies of plumes and fountains in linearly stratified ambient fluid have been performed by Fox (1970), Bloomfield & Kerr (1998, 2000) and Richards *et al.* (2014), who characterized the height of the neutral density and spreading levels in terms of the source momentum and buoyancy fluxes as well as the ambient stratification.

The case of a two-layer stratified ambient fluid is different (Kumagai, 1984; Mott & Woods, 2009; Shrinivas & Hunt, 2014). The plume can either spread at the interface or else penetrate through it. In the former scenario and assuming a descending plume in a horizontally confined region, the sharp ambient interface of the two-layer fluid acts as a false bottom so that a filling-box type flow is realized in the (bounded) upper layer. (Kumagai, 1984; Mott & Woods, 2009). Despite the ostensible similarities to a classical filling box flow, one difference pertains to plume-top entrainment, which occurs because the plume

overshoots the interface, entrains lower layer fluid and then brings some of this lower layer fluid back to the interface. The other difference is that, instead of spreading above the interface as if it was a rigid false bottom, the intrusion propagates within the interface between upper and lower layers. Due to the plume and plume-top entrainment, both the depths of the upper and lower layers are correspondingly modified. Chapter 2 of this thesis investigates a similar circumstance as in Kumagai (1984) and Mott & Woods (2009), with the added complication that the ambient stratification is modified by inflows into the upper layer and outflows from the lower layer. These can lead to regime transition, e.g. the plume might initially penetrate through the interface but later spread along it as a result of plume entrainment and changes to the upper and lower layer depths.

### 1.2.4   Rotating plumes

Because a plume is commonly a small spatial-scale and fast time-scale phenomenon, the influence of the Earth's rotation on the plume is usually neglected. However, some plumes are manifest in environments with large spatial scales, such as giant volcanic explosive eruptions (Baines & Sparks, 2005; Woods, 2010), long temporal scales, such as the sustained oil spill from the seafloor following the Deepwater Horizon accident (Frank *et al.*, 2017), or both, as in the case of vertical convection in the ocean from the surface (Jones & Marshall, 1993; Fernando *et al.*, 1998) or from a spring at the sea floor (Speer & Marshall, 1995). Plumes in rotating ambient fluid were studied laboratory experimentally (Fernando *et al.*, 1998; Yamamoto *et al.*, 2011; Frank *et al.*, 2017), with coarse numerical simulations (Speer & Marshall, 1995) and more recently with high resolution 3D simulations (Fabregat Tomàs *et al.*, 2016).

   The entrainment rates of turbulent thermals in a rotating ambient fluid were found to be suppressed if the local Rossby number[1], Ro, was small (Helfrich,

---

[1]The Rossby number is defined as Ro= $\frac{U}{fL}$, where $U$ is the characteristic value of horizontal velocity, $L$ is the characteristic length of the flow in the horizontal direction and $f = 2\Omega$ is the Coriolis parameter, where $\Omega$ is the background rotation rate.

1994; Fernando *et al.*, 1998). The influence of rotation on the entrainment of an isolated point-source plume with constant source buoyancy flux has not been well examined. The Coriolis force alters the direction of the ambient fluid inflow towards the plume. Consequently, a circular (cyclonic) flow around the plume develops, as observed by Fernando *et al.* (1998). This circular flow retards further ambient inflow towards into the plume. Fernando *et al.* (1998) also found that the circular flow was unstable in their experiments. As such, it broke up allowing the amount of entrainment to increase once more. In the study of rotating Rayleigh-Bénard convection (Julien *et al.*, 1999), a similar influence of rotation suppressing entrainment was drawn from statistical analyses of the convective elements, each regarded as individual plumes.

The impact of background rotation also acts upon lateral intrusions formed by a plume spreading at its neutral buoyancy level or at a top or bottom boundary. In comparison with the scenario without background rotation, where the intrusion can propagate infinitely far away, the Coriolis force alters the spreading direction of the intrusion to become an anticyclonic lens and hence confine the intrusion close to the region of plume discharge. If the latter scenario is applied to the intrusion formed by a plume discharging in a two-layer stratified ambient fluid, the lens modifies the local stratification of the ambient fluid and subsequently modifies the buoyancy of the plume, resulting in eventual penetration of the plume through the interface. The physical process associated with this eventual penetration is examined for the first time in this thesis (Chapters 3 and 4).

## 1.3 Examples

Below some of the circumstances mentioned above in which plumes are naturally manifest in stratified and rotating environments are reviewed in detail.

## 1.3.1  Natural ventilation

The ventilation system of a building is essential to keep good air quality indoors and so make people feel comfortable. Contaminated indoor air, caused by exhalation and body heat or electrical appliance heating, has a higher temperature and hence a smaller density than either the ambient air inside or outside of the building. Ventilation exhausts the contaminated warm air through outtakes at high levels and brings in fresh cool air through intakes located at low levels close to the floor. Various kinds of ventilation systems have been engineered and, broadly speaking, these can be categorized as natural, mechanical and hybrid according to the method by which air flow is driven. Mechanical ventilation employs equipment such as fans and blowers to maintain the air flows. In comparison, natural ventilation is mainly driven by the buoyancy force of the warm air. There is also a kind of hybrid ventilation, which combines aspects of both mechanical and natural ventilation. Of the different ventilation systems, natural ventilation is more economical and environmentally friendly than hybrid and mechanical ventilation, and so natural ventilation is adopted where possible e.g. in temperate climates that do not experience too large a seasonal swing (Linden, 1999).

The modelling of natural ventilation was idealized by Linden *et al.* (1990) as a single ascending plume within a cubic domain driven by a point source of heat at the bottom. The domain was closed but with two openings to the exterior, one each located at upper and lower levels. The plume of warm air rose up to the ceiling and spread to form an upper layer. Meanwhile some warm air exited through the upper opening to the external ambient and an equal volume of fresh air entered through the lower opening to replace the air that exited. This type of ventilation is referred to as displacement ventilation in contrast to mixing ventilation, in which the warm (cold) air enters into the domain from low (high) level openings. At steady state, the interface between upper and lower layers, both of which are uniform in density, reaches a time-invariant level as the result of the balance of inflows and outflows to either

of the cubic domain or the upper layer within this domain. This emptying filling box model, as referred to by Linden *et al.* (1990), was an extension of the classical filling box, proposed by Baines & Turner (1969). Though simple in concept, the model in question revealed the basic physical process of natural ventilation. Further complexities are involved by considering two or more non-interacting plumes with different strengths (Cooper & Linden, 1996; Linden & Cooper, 1996), interacting plumes (Linden & Kaye, 2006) and/or multiple building zones (Flynn & Caulfield, 2006).

The ambient air in a ventilated building is modified by plumes to be approximately two-layer or continuously stratified. Most studies focused on an equilibrium state wherein the stratification was steady (Linden *et al.*, 1990; Cooper & Linden, 1996; Linden & Cooper, 1996). Kaye & Hunt (2004) studied displacement ventilation in the context of the time evolution from the initial to the final state, in which the upper and lower layers of the two-layer stratified ambient both changed in thickness. Inspired by the work of Kaye & Hunt (2004), one may also expect the stratification to change after reaching the equilibrium state if one or several heating sources suddenly changed their strengths (Bolster *et al.*, 2008). Changing stratification can also occur due to external environmental factors or changes of mechanical forcing in hybrid ventilation systems. For example, the strength or direction of the winds in external environments can suddenly change or vent fans can be turned on. The impact of a time-dependent ambient stratification due to external factors on the behaviour of plumes have not been well addressed in literature.

## 1.3.2 Marine effluent discharge

Human activities in urban areas produce numerous effluents, the discharge of which is one important problem faced by every city. Coastal cities can take advantage of the ocean by discharging the effluent into it. However discharging the effluent offshore causes sea water pollution. A common way to minimize the impact on coastal ecosystems is to diffuse the effluent to a low concentration

through marine outfall diffusers. Because the effluent is usually less dense than sea water, the diffusers are built at the seafloor and the effluent plume is diluted by entraining ambient sea water during the ascent of the resulting plume. This simple observation has motivated several studies into the influence of ambient stratification on the ascending effluent plumes (Daviero & Roberts, 2006; Tian *et al.*, 2006; Tate *et al.*, 2016; Hunt *et al.*, 2010). Strong stratification of the ambient sea water suppresses the plume rise height and thus reduces dilution efficiencies. Furthermore, the stratification of the coastal sea has seasonal variations as well as potential rapid variations due to storms and internal waves. A question is raised as to how these variations impact the dynamics of plume rise and lateral spread.

### 1.3.3   Rising marine oil spill plume

Marine oil spills are environmental disasters for the petroleum industry. Such oil pollution harmfully impacts marine animals, such as sea birds, and also negatively impacts the economy, most especially those of tourism and fishing. One of the largest marine oil spills on record is the Deepwater Horizon drilling rig oil spill that occurred in the Gulf of Mexico in the summer of 2010. This accident injected 4.9 million barrels of oil into the ocean from the seafloor (McNutt *et al.*, 2011). Even though the Rossby number, estimated with the source buoyancy flux, vertical depth of the sea and the background rotation rate was found to be large, suggesting a plume unaffected by rotation, Frank *et al.* (2017) argued that the Rossby number of the ambient flow, which was induced by the plume entrainment, was small and hence influenced by the background rotation. Thus Frank *et al.* (2017) carried out laboratory experiments to examine the influence of background rotation on a plume in a uniform ambient. They found that, as a result of the background rotation, the plume near the source precessed anticyclonically with a precession frequency proportional to the background rotation rate. Such behaviour was also found in simulations of rotating plumes in linearly stratified fluid (Fabregat Tomàs *et al.*, 2016).

### 1.3.4 Explosive volcanic eruptions and hydrothermal plumes

One of the most dramatic examples of plumes in the atmosphere is that of explosive volcanic eruptions. These eruptions release gases, molten lava, solid particles and particulate matter into the atmosphere. Among such gases are water vapour, carbon dioxide and other toxic gases such as sulphur dioxide, carbon monoxide, hydrogen sulphide and hydrogen fluoride. These hot gases and the suspended particles can rise up to tens of kilometres into the stratosphere. During volcanic plume rise the plume dilutes due to entraining ambient air. On the other hand, the stratosphere is strongly stably stratified, i.e. the potential density of the air decreases with height (Lagzi *et al.*, 2013). Eventually, the volcanic plume overshoots the altitude of neutral density and then, in the absence of wind, falls back upon itself in a symmetric fashion. At the neutral density altitude, the mixed fluid of emitted gases, air and aerosols intrude laterally. During this lateral movement, some of the ash falls to the ground, potentially causing problems for people's health through ash inhalation, and causing damage to urban infrastructures and agriculture (Wilson *et al.*, 2015). Besides causing problems in areas nearby volcanoes, these gases and particles can also be transported by winds thousands of kilometres from their source. Consequential problems caused by these gases and ash are air pollution, acid rain, and threats to aviation as evidenced by the closure of the European airspace following the Icelandic volcanic eruption of Eyjafjallajökull in 2010. The aerosols emitted from the volcanoes or oxidized from sulphur dioxide can travel globally within a short time period of 22 days (Bluth *et al.*, 1992) and have an influence on the climate, for example by inhibiting solar radiation and depleting stratospheric ozone (Robock, 2000). The understanding of volcanic plume dynamics is essential to predict the rise height in different atmospheric conditions.

It is estimated that 85% of volcanism happens undersea (White *et al.*, 2015). Associated with submarine volcanoes, hydrothermal vents are found along the mid-ocean ridges. Along these ridges, seawater permeates through the fissures of the crust and then is heated by molten rocks before flowing back into the

ocean (German & Seyfried, 2013). This extremely hot seawater acts as a buoyancy source of plumes. It was estimated by Stein & Stein (1994) that 34% of the heat flux from the Earth's interior to the ocean occurs in such hydrothermal flows. The hot seawater not only provides heat but also carries chemicals and nutrients for microorganisms around hydrothermal vents in the deep ocean. Hydrothermal plumes in a rotating linearly stratified ambient fluid were examined experimentally by Helfrich & Battisti (1991) and numerically by Speer & Marshall (1995). They observed that the lateral intrusion that appeared at the neutral density level was confined to a limited region being manifest as an anticyclonic lens. In the experiments the lens became unstable after reaching a large radius set by the deformation radius. Even though a figure was given by Helfrich & Battisti (1991) which showed the experimental measurements of the time-evolution of the aspect ratio of the radius to the thickness of the lens, the physical mechanism underpinning this relation was not well understood.

### 1.3.5 Ocean convection

Vertical convection due to cooling at the surface of the oceans is part of the downwelling branch of the Meridional Overturning Circulation (MOC) (Lozier, 2011). Seawater in the upper ocean is transported from low latitudes to high latitudes in general. At high latitudes particularly in winter, cooling causes the surface water to descend into the deep ocean. This then flows back to low latitudes eventually upwelling again through long time turbulent diffusive processes (Munk, 1966). Because the surface water at low latitudes is much warmer than that at high latitudes, heat energy is also transported from the tropics to the polar regions. At high latitudes the heat is transferred from the ocean to the atmosphere, serving to regulate the climate system. Mullarney *et al.* (2004) performed a fundamental study of the MOC with laboratory experiments and numerical simulations. They simplified the MOC as a circulation developed in a long water channel where heating and cooling were each applied over one half of the bottom boundary corresponding to cooling and heating on the ocean

surface. In their experiments, they observed a rising plume formed at one end of the channel through the full depth of the ambient fluid. Following the work by Mullarney *et al.* (2004) and taking into account the Coriolis effect, Hughes & Griffiths (2006) adapted the filling box model to include distributed surface heating and single point cooling to capture the essential processes of the MOC, in which the downwelling was characterized as a slope plume (or slope current).

The Labrador Sea is one of the most important sites in the global oceans where deep ocean convection occurs (Clarke & Gascard, 1983; Holdsworth & Myers, 2015; Yang *et al.*, 2016*b*). The strongest deep convection occurs in the winter when southward and eastward cold winds remove heat and moisture from the surface of the Labrador Sea. As a consequence of deep convection, there appears in the Labrador Sea in winter a deep uniform mixed layer that can reach more than 1 km in depth (Yashayaev & Loder, 2009). In spring, the winds become less intense, the air temperature and solar radiation increases, and this reduces the source buoyancy flux of the convection. Moreover, warm and relatively fresh surface water is transported by eddies from boundary currents into the middle of the Labrador Sea thereby increasing the near surface stratification. These effects serve to suppress the deep convection, as a result of which the upper ocean is re-stratified and gas exchange between the atmosphere and the ocean interior is suppressed (Marshall & Schott, 1999).

As the above discussion makes clear and due to seasonal effects, the stratification of the ocean is time-dependent. In the Labrador Sea, seawater can be roughly regarded as a two-layer stratification with a uniform upper mixed layer and a weakly stratified lower layer. The mixed layer thickness varies from less than about 50 m in summer to more than 1 km in winter (Courtois *et al.*, 2017). Even though the vertical convection in the ocean is horizontally broad and includes much more complex processes than those of a descending localized plume, the physical process of ocean vertical convection is related to the work herein insofar as it involves vertical motion driven by buoyancy in a time-evolving stratified ambient fluid. To gain insight into the complex phenomenon of verti-

cal convection in ocean, it helps to know the fundamental physical processes of a plume in a time-evolving stratified ambient.

## 1.4   Scope of thesis

As in the examples above, there are many circumstances in industrial, environmental and geophysical flows where the ambient stratification evolves in time in the presence of a plume. However, the influence of the time-evolving ambient stratification on plumes is poorly understood. Furthermore, some of these examples show that rotation can have a significant influence on plume dynamics, though these have not been well-examined. In this thesis the investigation of a plume in an ambient fluid combining time-evolving stratification with and without background rotation aims to offer insight into our understanding of vertical convection in natural environments.

In Chapter 2, a descending line-source plume in a time-evolving two-layer stratified ambient fluid is investigated experimentally. Specifically, the experiments are designed so that the upper layer thickness between the plume source and the ambient interface increases in time. In some circumstances the plume, which initially penetrates through the two-layer ambient interface to depth, is found eventually to spread entirely along the ambient interface. During this transition process, a plume splitting phenomenon is observed in which both penetration and spreading occur. This work has been published in the Journal of Fluid of Mechanics (Ma *et al.*, 2017).

In Chapter 3, the influence of background rotation on a point-source plume is taken into consideration. The plume descends from the free surface into a two-layer stratified ambient fluid. In most experiments the plume initially spreads horizontally when it reaches the interface. Rotation not only alters the lateral intrusion process, resulting in eventual penetration, but it also causes the plume to precess anticyclonically near the source. This work is in preparation for submission to Environmental Fluid Mechanics.

In Chapter 4, numerical simulations are performed with conditions similar

to the experiments reported upon in Chapter 3. The results of simulations in a non-rotating uniform ambient fluid show good comparisons with the MTT model results. In simulations of plumes in a rotating uniform and two-layer stratified ambient fluid the rise and spread of the plume are found to be similar to that observed in our laboratory experiments. The work is in preparation for submission to Environmental Fluid Mechanics.

An overall summary that identifies the main contributions for the work as a whole is presented in Chapter 5.

# Chapter 2

# Convection from a line-source into a two layer stratified ambient fluid

## Summary

We experimentally investigate the behaviour of a line-source plume falling through a finite two-layer stratified ambient where the depth of the upper ambient layer increases in time. Laboratory observations suggest one of two possible flow regimes depending on the value of $\lambda$, which represents the relative loss of buoyancy experienced by the plume upon crossing the ambient interface. When $\lambda > 1$, a classical filling-box-type flow is realized and plume fluid always reaches the bottom boundary. By contrast, when $\lambda < 1$, we observe a transition by which an increasing fraction of plume fluid discharges along the interface. The approximate start time, $t_v$, and end time, $t_t$, of the transition process are well-determined by $\lambda$. After transition the ambient density evolves to form a three-layer fluid with an intermediate layer that grows in time. Measured densities of the intermediate layer in experiments with $\lambda < 1$ are well predicted using plume theory. We further characterize the horizontal speed of the intrusion that forms along the ambient interface, the mass of solute present in the intermediate layer at time $t_t$ and the rate of descent of the intrusion level for $t > t_t$. The significance of our findings are discussed in the context of the ventilation of natural and hybrid ventilated buildings and of effluent discharge through marine outfall

diffusers.

## 2.1 Introduction

Liquid waste from coastal cities is often discharged into the marine environment through outfall tunnels drilled into the seabed. At the point of discharge, the (buoyant) effluent emanates from multiple diffusers and then merges together to form a single line-plume. The plume continues to rise to the sea surface if the sea water has uniform density. More desirably, density stratification may cause the plume to spread at some intermediate depth along its level of neutral buoyancy. In the coastal ocean where ascending effluent plumes are situated, seawater can vary between states of uniform density and comparative strong stratification. This variation has an obvious impact on the height of rise of the effluent. For example, the waste water from Boston is discharged into Massachusetts Bay, which tends to be well mixed in winter because of surface cooling and wind forcing. In summer near surface waters become both fresher and warmer as a result of which the plume is trapped below this light surface layer (Hunt *et al.*, 2010).

At smaller scales, a plume in an evolving stratified environment is also relevant to naturally or hybrid ventilated buildings. Consider, for example, a building that contains internal sources of buoyancy in the form of heat-producing electrical equipment that creates vertically-ascending thermal plumes. This heat is vented to the exterior environment through high-level openings. The escaping buoyant air is, in turn, replaced with cool ambient air that enters the building through low-level openings (Linden *et al.*, 1990). An interior two-layer stratification thereby develops where, at steady state, the temperature of the buoyant upper layer matches the temperature of the plume at the interface. Any subsequent changes in the plume source conditions, for example due to an alteration of equipment operation (Bolster *et al.*, 2008), may lead, for example, to partial and eventual full detrainment of the plume below the ceiling.

Common to both of the above examples is vertical convection from an iso-

lated source that yields an (ascending) plume. Plume flow in a stratified or uniform ambient was investigated quantitatively by Morton *et al.* (1956), who developed a one-dimensional model to describe a statistically steady turbulent plume released from a point source into an unbounded uniform or stratified ambient. In particular, analytical solutions were found for the case of a uniform ambient. This model has since been tested and widely adapted to a variety of circumstances including effects of a finite-sized ambient (Baines & Turner, 1969; Germeles, 1975), plumes and fountains in stratified fluid (Morton, 1959; Bloomfield & Kerr, 1998, 2000), and line-plumes in two-layer stratified fluid (Noh *et al.*, 1992) – see Woods (2010) for further details.

In one particularly relevant application, Baines & Turner (1969) examined the evolution of the (initially uniform) ambient density in a finite control volume containing an ascending vertical plume: the so-called filling box model. Upon reaching the free surface, the plume fluid spread in the lateral direction to form a lighter upper layer that deepened in time. The "first front", the interface between the discharged plume fluid and the original ambient, descended against the direction of the rising plume and some fraction of this discharged plume fluid was re-entrained into the plume and carried again to the free surface. Although the lighter density of the upper layer diminished the plume vertical velocity, the density difference across the first front never became so strong that the plume could not arrive at the free surface.

Numerous other studies have expanded upon the seminal work of Baines & Turner (1969) by considering a nonuniform ambient at the initial time. For example, Kumagai (1984) generated a dense plume through a nozzle placed at the free surface of a two-layer stratified ambient, in which the plume could not initially fall through the lower layer. The plume evolved to become a fountain below the ambient interface rising back to the interface and then spreading horizontally. Kumagai (1984) adapted the filling box model by parameterizing the entrainment from the lower layer fluid below the interface. This so-called fountain top entrainment had the effect of progressively deepening the interface

as a result of the transport of entrained lower layer fluid returning upwards. Following Kumagai (1984), Mott & Woods (2009) considered plume impingement from above upon an ambient interface as an intense mixing process that thickened the interface instead of deepening it. In collapsing their data, Mott & Woods (2009) found it helpful to introduce a parameter $\Lambda$, which was the ratio of the reduced gravity of the plume just above the interface with respect to the upper layer ambient to the reduced gravity associated with the upper and lower ambient layers. For $0 \leqslant \Lambda < 1$, the plume at the location of the interface was lighter than the lower layer fluid and so was expected to spread along the ambient interface. By contrast, for $\Lambda > 1$, the plume was expected to descend into the lower layer. The values of $\Lambda$ in the experiments of Kumagai (1984) were limited to between 0 and 0.15, while Mott & Woods (2009) ran experiments with a notably larger range: $0 < \Lambda < 0.64$. In both sets of experiments the plume was observed to spread along the interface, as expected. In this case the plume flow in the upper layer can be regarded, at least initially, as a filling box process with the interface serving as a surrogate bottom boundary.

In a study by Camassa *et al.* (2016), an ascending buoyant jet in two-layer stratified ambient fluid was examined whether it could penetrate through or be trapped under the density interface. Camassa *et al.* (2016) theoretically derived a critical distance between the nozzle and the ambient interface to predict the buoyant jet behaviours of either penetrating or being trapped under the sharp interface. Wallace & Sheff (1987) and Kulkarni *et al.* (1993) respectively performed experiments of line-source and point-source plumes with effective values of $\Lambda$ being less than and greater than unity. Although they did not compute this quantity explicitly, the values of $\Lambda$ ranged from 0.19 to 2.92 in the study of Wallace & Sheff (1987) and from 0.11 to 2.76 in the study of Kulkarni *et al.* (1993). These $\Lambda$ values we estimate from plume theory assuming an ideal point source and an entrainment coefficient of 0.1. In both sets of experiments the tank was sufficiently large that boundaries played an insignificant role. Wallace & Sheff (1987) and Kulkarni *et al.* (1993) observed different evolution regimes

depending upon different combinations of the experimental parameters, including the density and volume flux of the plume source, the depth of the upper layer and the densities of the upper and lower layers. If the plume density just above the interface was significantly greater than that of the lower layer ($\Lambda \geqslant 2.92$ in the study of Wallace & Sheff 1987 and $\Lambda \geqslant 2.25$ in the study of Kulkarni *et al.* 1993), all of the plume fluid penetrated through the interface. Conversely, if the density of the plume just above the interface was smaller than that of the lower layer ($\Lambda \leqslant 0.19$ in the study of Wallace & Sheff 1987 and $\Lambda \leqslant 0.21$ in the study of Kulkarni *et al.* 1993), some plume fluid nonetheless penetrated into the lower layer due to inertia. An inverted fountain was thereby formed and whatever plume fluid penetrated into the lower layer eventually flowed as an interfacial gravity current along the ambient interface. Finally, a partial penetration regime occurred if the mean density of the plume just above the interface was comparable to the lower layer density ($\Lambda \approx 0.97$ in the study of Wallace & Sheff 1987 and $0.86 \leqslant \Lambda \leqslant 2.13$ in the study of Kulkarni *et al.* 1993). Because the horizontal time-averaged density distribution of a plume was nonuniform (as opposed to the uniformity assumed by the so-called "top-hat" formulation) and rather varied as an approximate Gaussian distribution, the fluid in the core (periphery) of the plume was denser (lighter) than the lower layer. Thus, as the plume impinged upon the interface, part of the plume penetrated through the interface and continued to descend while the rest intruded at the interface. We refer to this phenomenon as a "splitting plume".

In related work, a downslope-propagating gravity current impinging upon an interface in a two-layer ambient was examined by Wells & Wettlaufer (2007) and Cortés *et al.* (2014). Like Kumagai (1984) and Mott & Woods (2009), Wells & Wettlaufer (2007) determined that gravity current fluid accumulated at the interface of the two-layer fluid causing the gravity current to break through the interface after some time. Like Kulkarni *et al.* (1993), Cortés *et al.* (2014) found three different regimes characterized by (i) total penetration of the gravity current through the interface, (ii) total spreading along the ambient interface

or (iii) partial splitting at the interface. Cortés *et al.* (2014) characterized the regimes in terms of a bulk Richardson number, Ri, (which is effectively inversely proportional to $\Lambda$) and a Froude number, Fr, which is the ratio of the current speed to the shallow water speed based on the current height.

One of the principal limiting assumptions associated with the above studies is that the upper ambient layer is uninfluenced by external effects, being affected by the impinging plume alone. In the present investigation we extend this previous line of inquiry by examining a line-source plume that descends into a two-layer stratified ambient in which the upper layer is allowed to deepen as a consequence of surface fresh water inputs that, at least initially, are larger than the flux of fresh water out of the upper layer due to entrainment into the descending plume. The surface level is kept fixed by extracting fluid from the bottom of the lower layer at the same rate as fresh water and plume fluid are added at the top. With this setup, we are able to observe in some experiments the transition in time from a bottom spreading plume to an interfacially splitting plume and then finally to an interfacially spreading plume. We characterize this complete life-cycle in terms of relevant experimental parameters associated both with the plume and also with the ambient stratification.

The rest of Chapter 2 is organized as follows. In Section 2.2, equations for the evolution of a plume in unbounded and bounded domains are reviewed. The experimental setup is presented in Section 2.3. Thereafter, the detailed analyses of three experiments exhibiting qualitatively different flow behaviour are considered. Section 2.4 also contains a summary of salient quantitative results. Finally, our discussion and conclusions are provided in Section 2.5.

## 2.2 Theory

### 2.2.1 Equations for a line-source plume

Morton *et al.* (1956) formulated equations to describe a statistically steady plume descending into an infinite environment. Although derived for a point-

source plume, the model is readily adapted for a line-source plume geometry (Lee & Emmons, 1961). These are the equations presented here.

The horizontal cross-section of the plume is assumed to have self-similar time-averaged horizontal profiles that scale with height. For conceptual convenience, the profiles are taken to have top-hat structure. In reality, the time-averaged structure is closer to Gaussian and it is because of this that one might expect plume-splitting behaviour, as discussed in the Introduction. However, the intent of this section is to classify when plume splitting may occur, but not to model the splitting process itself. Under the top-hat assumption, the time averaged profiles of the vertical velocity and reduced gravity are

$$w(x, z) = \begin{cases} \bar{w}(z), & \text{if } |x| \leqslant b(z) \\ 0, & \text{if } |x| > b(z) \end{cases} \tag{2.1}$$

$$g'(x, z) = \begin{cases} \bar{g}'(z), & \text{if } |x| \leqslant b(z) \\ 0. & \text{if } |x| > b(z) \end{cases} \tag{2.2}$$

Here, $x$ is the horizontal co-ordinate with origin at the plume midpoint, $z$ is the vertical co-ordinate whose positive direction is taken to be downward from the point source for a descending plume, $b(z)$ is the half-width of the line-plume, $\bar{w}(z)$ is the mean vertical velocity of the plume and $\bar{g}'(z) = g\left(\bar{\rho}(z) - \rho_0(z)\right)/\rho_0(0)$ is the mean reduced gravity, in which $g$ is gravity, and $\bar{\rho}(z)$ and $\rho_0(z)$ are the densities of the plume and ambient, respectively, measured at elevation $z$. The ambient density, $\rho_0(z)$, is taken to be smaller than the plume density, at least near the source, so that $\bar{g}'(z)$ is positive. At any vertical level, the volume, momentum and buoyancy fluxes per unit width of a line-plume are defined by

$$Q(z) = \int_{-\infty}^{\infty} w \, \mathrm{d}x = 2\bar{w}(z)b(z), \tag{2.3}$$

$$M(z) = \int_{-\infty}^{\infty} w^2 \, \mathrm{d}x = 2\bar{w}^2(z)b(z), \tag{2.4}$$

$$F(z) = \int_{-\infty}^{\infty} wg' \, \mathrm{d}x = 2\bar{g}'(z)\bar{w}(z)b(z). \tag{2.5}$$

21

Assuming density variations between the ambient and plume are small, the Boussinesq approximation can be invoked, in which case the dynamics of an ascending plume are equivalent to those of the descending plume studied here. The system is closed by making the entrainment assumption that the horizontal inflow velocity just outside the plume due to entrainment is proportional to the mean vertical velocity of the plume at that vertical level with proportionality constant $\alpha$. Reported values for the so-called entrainment coefficient differ depending on the experimental details (Lee & Emmons, 1961; Kotsovinos, 1975; Yuana & Cox, 1996), but it is generally agreed that for a line-plume $\alpha$ falls between about 0.1 and 0.16. From the conservation of volume, momentum and buoyancy for an incompressible fluid, the following respective equations can be derived for the (steady state) vertical variation of $Q$, $M$ and $F$:

$$\frac{\mathrm{d}Q}{\mathrm{d}z} = 2\alpha \frac{M}{Q}, \tag{2.6}$$

$$\frac{\mathrm{d}M}{\mathrm{d}z} = \frac{FQ}{M}, \tag{2.7}$$

$$\frac{\mathrm{d}F}{\mathrm{d}z} = -Q \frac{\mathrm{d}g_0'}{\mathrm{d}z}. \tag{2.8}$$

Here $g_0'(z) = g(\rho_0(z) - \rho_0(0))/\rho_0(0)$ is the reduced gravity for the ambient density relative to a characteristic density, $\rho_0(0)$.

## 2.2.2 Solutions in a uniform ambient

For an ideal line-plume originating from an infinitesimally thin source at $z = 0$ and descending through a uniform ambient, theoretical solutions can be obtained from (2.6)-(2.8) by setting $g_0'(z) = 0$ and taking the source volume and momentum fluxes to be zero. The volume, momentum and buoyancy fluxes per unit width as functions of depth are found to be

$$Q(z) = (2\alpha)^{2/3} F_s^{1/3} z, \tag{2.9}$$

$$M(z) = (2\alpha)^{1/3} F_s^{2/3} z, \tag{2.10}$$

$$F(z) = F_s, \tag{2.11}$$

where $F_s$ is the source buoyancy flux per unit width. From (2.3)-(2.5), it follows that the mean reduced gravity of the plume is

$$\bar{g}'(z) = \frac{F_s}{Q(z)} = (2\alpha)^{-2/3} F_s^{2/3} z^{-1}, \qquad (2.12)$$

and the half-width of the plume is

$$b(z) = \frac{Q^2(z)}{2M(z)} = \alpha z. \qquad (2.13)$$

### 2.2.3 Filling box theory

The above solutions apply for the case of a line-plume in a stationary unbounded ambient. Considering a descending line-source plume in a confined region, such as a rectangular tank with length $L_T$, the vertical velocity of the rising ambient return flow can be obtained from conservation of volume as $-Q(z)/L_T$. By extension, and ignoring diffusion, the ambient density evolves according to the following advection equation (Baines & Turner, 1969):

$$\frac{\partial g'_0}{\partial t} = \frac{Q}{L_T} \frac{\partial g'_0}{\partial z}. \qquad (2.14)$$

The filling box model is obtained by coupling (2.14) with (2.6)-(2.8). Taking this approach, Baines & Turner (1969) derived an expression for the position of the first front with time, $t$. They assumed that the ambient density increases linearly with $t$ in the long-time limit whereas other variables, such as the plume radius, vertical velocity and reduced gravity were time independent.

Germeles (1975) extended the Baines & Turner (1969) model by considering non-ideal plumes and, more importantly, by developing a numerical algorithm to solve the filling box model, in which the ambient density profile was discretized into a staircase structure. At each time step a new layer representing the discharged fluid from the plume impacting the lower boundary was added at the bottom of the profile.

The time for the entire box to be filled with discharged plume fluid, equivalent to the time required by the first front to reach the elevation of the source,

is referred to as the filling box time, $T_{fb}$. For an ideal line-source plume, the filling box time is given by (Baines & Turner, 1969):

$$T_{fb} = \frac{L_T}{(2\alpha)^{2/3} F_s^{1/3}}.$$
(2.15)

## 2.2.4 Plume incident upon an interface of a two-layer fluid

For an ideal plume falling through a two-layer stratified ambient with a lower layer having density $\rho_l$ and depth $H_l$ and an upper layer having density $\rho_u$ and depth $H_u$, (2.12) gives the reduced gravity of the plume just above the interface as

$$\bar{g}'(H_u) = g\frac{\bar{\rho}(H_u) - \rho_u}{\rho_u} = (2\alpha)^{-2/3} F_s^{2/3} H_u^{-1}.$$
(2.16)

At this depth, the mean density of the plume is less than (greater than) the lower layer density if $\bar{g}'(H_u)$ is less than (greater than) the reduced gravity, $g'_{ul}$, based on the density contrast between the lower and upper layers where

$$g'_{ul} = g\frac{\rho_l - \rho_u}{\rho_u}.$$
(2.17)

As suggested by the previous discussion, the ability of the plume to descend within the lower layer can be assessed by forming the ratio of these two quantities (Mott & Woods, 2009):

$$\Lambda \equiv \frac{\bar{g}'(H_u)}{g'_{ul}} = (2\alpha)^{-2/3} \frac{F_s^{2/3}/H_u}{g'_{ul}}.$$
(2.18)

If $\Lambda > 1$, the plume can penetrate through the interface initially and will continue to do so for all time: the finite width of the domain implies that the upper layer thickness $H_u$ will progressively decrease as the ambient fluid in the upper layer is entrained into the plume and carried to depth. As a result, $\bar{g}'(H_u)$ and hence $\Lambda$ will increase with time so that $\Lambda$ is always greater than unity. On the other hand, if $\Lambda < 1$ initially, the plume will spread at the interface. Over time, the plume will therefore descend into the evolving stratified ambient in the upper layer as predicted by the filling box theory of Baines & Turner

24

(1969). This situation will persist if $\Lambda \ll 1$ in which case the ambient interface effectively plays the role of a solid bottom boundary. However, if $\Lambda$ is initially not too much smaller than 1, it is possible that $\bar{g}'(H_u)$ will increase sufficiently as a result of the density increase of the upper layer ambient so that plume breakthrough occurs at some later time (Mott & Woods, 2009).

For a constant flux gravity current propagating downslope through the interface of a two-layer ambient, Cortés *et al.* (2014) argued that both the Richardson number, Ri, and the Froude number, Fr, determine whether the gravity current splits or not. They defined

$$\text{Ri} = \left( \frac{F_s^{2/3}/H_u}{g'_{ul}} \right)^{-1}, \tag{2.19}$$

$$\text{Fr} = \frac{U}{(g'h)^{1/2}}, \tag{2.20}$$

in which $U$, $g'$ and $h$ are the average velocity, reduced gravity and the thickness of the gravity current, respectively. From the dimensional analysis of a two-dimensional gravity current, $F_s^{2/3}/H_u$ is proportional to the reduced gravity of the gravity current just above the interface. Accordingly, Ri defined by (2.19) is proportional to $\Lambda^{-1}$.

## 2.2.5 Filling box flow in a two-layer ambient fluid containing an ambient source and sink

As a nontrivial extension of the flow scenario described in Section 2.2.4, consider a case in which lower layer fluid is extracted from the bottom of the domain with a constant volume flux per unit width $Q_{\text{sink}}$ while fluid with density $\rho_u$ is injected at the surface with constant volume flux per unit width $Q_u$, as shown in figure 2.1. So that the total volume in the domain remains constant (and hence the free surface stationary), $Q_{\text{sink}}$ is chosen to equal the sum of $Q_u$ and the volume flux per unit width from the line-plume source, $Q_s$. For an ideal plume, $Q_s = 0$, by definition, and therefore $Q_{\text{sink}} = Q_u$.

In the absence of the plume, the interface would descend at a speed $Q_{\text{sink}}/L_T$. Conversely, in the absence of the sinking flow ($Q_{\text{sink}} = 0$) and as a consequence
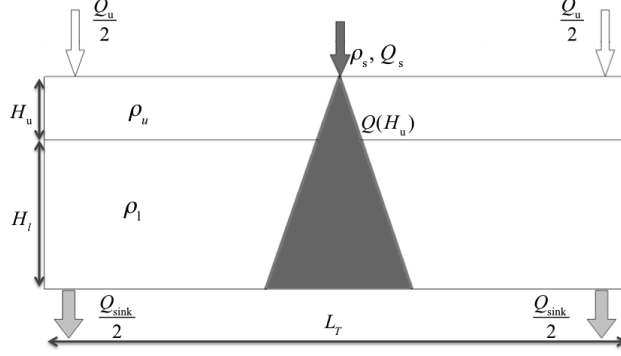
Figure 2.1: Schematic of a line-plume descending through a two-layer ambient with upper layer density $\rho_u$, upper layer depth $H_u$ and lower layer density $\rho_l$, lower layer depth $H_l$. The source density of the non-ideal plume is $\rho_s$ and its volume flux per unit width is $Q_s$. Fluid of density $\rho_u$ is also injected at a constant rate, $Q_u$, equally at either side of the domain near the surface. Meanwhile, fluid is extracted at a constant rate $Q_{\text{sink}} = Q_s + Q_u$ equally at either side of the domain from the bottom, so that the free surface remains fixed in time.

of entrainment of upper layer fluid into a pure plume, the interface would rise at the (time-variable) speed $Q(H_u)/L_T$. If $Q_{\text{sink}} > 0$ and the plume penetrates into the lower layer, carrying entrained upper layer fluid to depth, the interface would have a speed of $(Q_{\text{sink}} - Q(H_u))/L_T$, with a downward (upward) direction if the sign is positive (negative). The competition between these effects with $Q_{\text{sink}} > 0$ and $Q(H_u) > 0$ are considered here specifically for the circumstance in which $H_u$ is initially zero. By extension, $H_u(t)$ can be expressed as

$$H_u(t) = \int_0^t \frac{Q_{\text{sink}} - Q(H_u(\tau))}{L_T} \mathrm{d}\tau. \tag{2.21}$$

Assuming the plume always penetrates into the lower layer, the interface deepens asymptotically to a depth $H_{u\infty}$, at which point the volume flux per unit width of the plume at the interface $Q(H_{u\infty})$ is balanced by $Q_{\text{sink}}$. Using (2.9), the steady state upper layer thickness is predicted to be

$$H_{u\infty} = \frac{Q_{\text{sink}}}{(2\alpha)^{2/3} F_s^{1/3}}. \tag{2.22}$$

The characteristic time for the interface to deepen to its time-independent value is

$$\frac{H_{u\infty}}{Q_{\text{sink}}/L_T} = \frac{L_T}{(2\alpha)^{2/3} F_s^{1/3}}, \tag{2.23}$$

which is just the filling box time $T_{fb}$ expressed in (2.15).

The steady state upper layer depth prescribed by (2.22) can only be achieved if the plume density at $H_{u\infty}$ is greater than $\rho_l$ so that the plume continues to descend into the lower layer. Analogous to the time-dependent variable $\Lambda$ prescribed by (2.18), we define a time-independent variable $\lambda$ by

$$\lambda \equiv \lim_{t \to \infty} \Lambda = \frac{\bar{g}'(H_{u\infty})}{g'_{ul}} = \frac{F_s}{g'_{ul} Q_{\text{sink}}}. \tag{2.24}$$

The term $g'_{ul} Q_{\text{sink}} = g'_{ul} Q(H_{u\infty})$ can be interpreted as the loss of buoyancy flux per unit width that is experienced by the plume as a consequence of traversing the interface. By extension, $\lambda^{-1}$ is the relative loss of buoyancy flux per unit width as the plume penetrates into the lower layer from the upper layer.

While Mott & Woods (2009) focused on cases with no sinking flow and initially with $\Lambda < 1$, here we consider cases where $\Lambda$, though initially greater than unity, subsequently decreases as the sinking flow acts to increase $H_u$. Whether $\Lambda < 1$ in the long time limit depends on the value of $\lambda$ given by (2.24), which in turn depends upon the external parameters $F_s$, $Q_{\text{sink}}$ and $g'_{ul}$, all of which are time-independent by assumption. If $\lambda > 1$, the plume is predicted to descend into the lower layer for all time. By contrast if $\lambda < 1$, eventually the plume will not penetrate through the interface, and will instead spread above the lower layer. In the latter case, one anticipates a transition regime in which the plume splits, corresponding to partial outflow along the interface as $\Lambda$ falls below a value of order unity. Once splitting begins, a positive feedback occurs whereby the upper layer deepens and further decreases $\Lambda$, so that eventually the plume is expected to spread entirely at the interface. These predictions are tested against laboratory experiments. Although our analysis, experimental and otherwise, is here restricted to a line-source plume, we expect the condition $\lambda = 1$ likewise represents a marginal case when the plume structure takes other shapes at the source, e.g. a point, or even a distributed, source. Indeed, this is the basis for the comparisons with environmental and architectural flows that we draw in section 2.5.
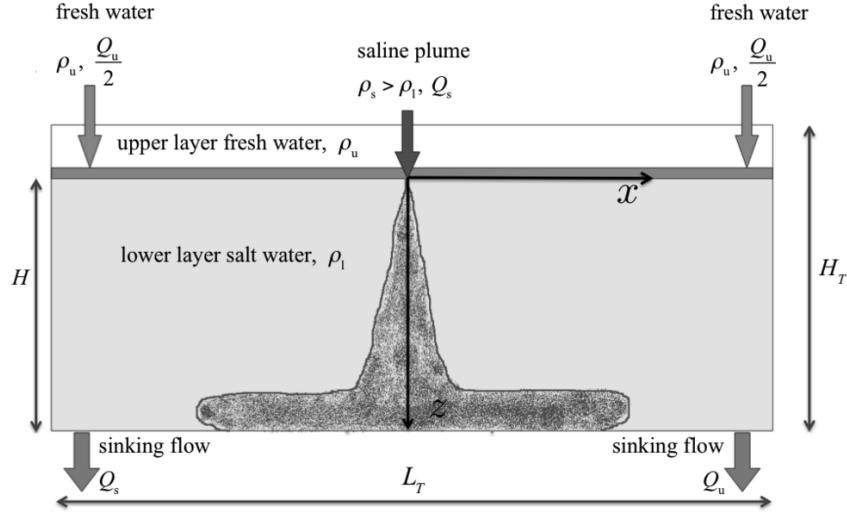
Figure 2.2: Schematic diagram of the laboratory experimental setup. The tank measured $L_T = 120$ cm long, $W_T = 8$ cm wide and $H_T = 40$ cm deep. The upper layer of the ambient was fresh water with density $\rho_u$ and the lower layer was filled with salt water having density $\rho_l$.

## 2.3 Experimental setup

Laboratory experiments were conducted in an acrylic tank with rectangular cross-section, as shown schematically in figure 2.2. The tank measured $L_T = 120$ cm long, $W_T = 7.6$ cm wide, and $H_T = 40$ cm deep. The tank was filled to a depth $H = 30$ cm with salt water of density $\rho_l$, measured with an Anton Paar DMA 4500 densitometer, having a precision of $\pm 0.00001$ g cm$^{-3}$. The density $\rho_l$ varied between $1.00100$ g cm$^{-3}$ and $1.02000$ g cm$^{-3}$ among different experiments. A relatively thin ($\sim 5$ cm) upper layer was established by adding fresh water dyed with green food colouring through sponge floats at both ends of the tank. Density profiles were measured by a vertically-oriented micro-scale conductivity probe (Precision Measurement Engineering, MSCTI) having a measuring frequency of 10 Hz. This probe was connected to a vertically traversing plate located at $x = -15$ cm, i.e. 15 cm to the left of the plume source. The plate and probe moved downward at a speed of 0.5 cm s$^{-1}$. Motion control was achieved using a stepper motor (Oriental Motor, PK245-01AA) connected to a computer running LabView. Probe measurements confirmed that the initial interface

thickness was around 1 cm.

A line-source nozzle spanning the tank width was located in the middle of the tank. The nozzle, whose opening measured 0.4 cm wide by 7.1 cm long, had a T-shaped internal structure that reduced the outflow speed. A piece of coarse sponge material was attached to the opening to introduce small perturbations to the flow and thereby trigger a laminar to turbulent transition in the plume. Schematics of the nozzle can be found in Appendix C of Roes (2014).

As shown in figure 2.2, the nozzle opening was always situated at the approximate mid-depth of the interface at the initial instant. Thus every experiment, regardless of the value of $\Lambda$, began the same way, i.e. with plume fluid falling all the way to the bottom of the tank.

Over the course of each experiment, red food colouring was periodically injected into the tubing connected to the source nozzle. At early times dye was injected every $\sim 3$ min including at $t = 0$. This time interval grew to 6 min as the experiment progressed and the flow dynamics became less transient. An electroluminescent light sheet with near-uniform intensity (Electric Vinyl, Perf-Alite Electric Vinyl) was placed 20 cm behind the tank. In front of the tank at a distance of 3 m was situated a digital video camera (Panasonic HDC-HS250) that recorded experimental images with a frame rate of 30 frames per second (fps). Although the shortest of our experiments lasted just over 1 hour, experiments were more typically run for 2 hours and, in one extreme case, more than 4 hours. For all experiments, digital movies were analyzed by extracting one frame per second to make time-lapse movies that were then imported into Matlab.

The experiment began with the activation of two peristaltic pumps (Manostat, Carter and Newport FPU5-MT/N) that acted as a source of salt water for the plume and as a source of fresh water for the surface layer. The peristaltic pumps also extracted water from the bottom of the tank. The volume flux of injecting flow into the tank is the same value of the extracting flow out of the tank with the same pump. The use of peristaltic pumps with tubing

of consistent diameter, wall thickness and material type ensured that the total volume of injected fluid was equal to the volume of extracted fluid. The pumps were calibrated by measuring with a stopwatch the time required to fill a graduated cylinder to a volume of $230\,\mathrm{mL}$. The constant rate of injection of fresh water, $Q_u W_T$, ranged from $2.0\,\mathrm{cm^3\ s^{-1}}$ to $7.1\,\mathrm{cm^3\ s^{-1}}$ in different experiments. Meanwhile, the source had a constant volume flux of $Q_s W_T$ that fell between $0.6\,\mathrm{cm^3\ s^{-1}}$ and $2.0\,\mathrm{cm^3\ s^{-1}}$ in different experiments.

The plume was generated by injecting dense salt water of density $\rho_s > \rho_l$, ranging between $\rho_s = 1.0130\,\mathrm{g\ cm^{-3}}$ and $1.1102\,\mathrm{g\ cm^{-3}}$. Multiple ambient density profiles were collected during each experiment, with a single traverse taking approximately 1 min. This was sufficiently fast compared to the slowly varying ambient density, that each profile could be considered as an instantaneous measurement of the ambient density. The probe was calibrated before and after each experiment using four salt water solutions whose densities were accurately measured with the densitometer.

## 2.4   Experimental results

### 2.4.1   Qualitative results and analysis methods

Three experiments are presented here for the purpose of illustrating the range of flow behaviour that was generally observed.

A classical filling box type experiment is shown in figure 2.3. Experimental parameters correspond to Expt. 22 in table 2.1, where the source buoyancy flux per unit width was calculated from

$$F_s = Q_s g \frac{\rho_s - \rho_u}{\rho_u}. \tag{2.25}$$

Two comments are necessary regarding (2.25). Firstly, and because the nozzle was initially located at the elevation of the ambient interface, it should be understood that the above definition for $F_s$ does not apply for small $t$. Secondly, $Q_s > 0$. To account for the finite source volume flux of the plume, the virtual source distance, $z_v$, was computed using the methodology of Hunt &

| Expt. | $\rho_s$ ($g\ cm^{-3}$) | $\rho_l$ ($g\ cm^{-3}$) | $Q_s W_T$ ($cm^3\ s^{-1}$) | $Q_{sink} W_T$ ($cm^3\ s^{-1}$) | $F_s$ ($cm^3\ s^{-3}$) | $\lambda$ | $t_t$ (min) |
|---|---|---|---|---|---|---|---|
| 1 | 1.02287 | 1.00655 | 0.437 | 7.67 | 1.39 | 0.172 | 17 |
| **2** | 1.02697 | 1.01063 | 0.61 | 4.48 | 2.24 | 0.320 | 20 |
| 3 | 1.04004 | 1.01056 | 1.00 | 8.14 | 5.37 | 0.422 | 13 |
| 4 | 1.04037 | 1.02009 | 1.01 | 4.61 | 5.47 | 0.424 | 17 |
| 5 | 1.05911 | 1.01008 | 0.46 | 4.00 | 3.60 | 0.600 | 34 |
| 6 | 1.05707 | 1.05165 | 2.00 | 3.06 | 15.14 | 0.720 | 24 |
| 7 | 1.02000 | 1.00500 | 1.01 | 4.54 | 2.80 | 0.739 | 39 |
| 8 | 1.03984 | 1.01037 | 0.97 | 4.35 | 5.14 | 0.791 | 27 |
| **9** | 1.05408 | 1.01060 | 0.77 | 4.44 | 5.49 | 0.791 | 39 |
| 10 | 1.06604 | 1.01534 | 0.94 | 4.55 | 8.20 | 0.827 | 38 |
| 11 | 1.02970 | 1.01033 | 0.96 | 3.02 | 3.87 | 0.837 | 52 |
| 12 | 1.00828 | 1.00098 | 1.02 | 4.57 | 1.29 | 0.870 | 68 |
| 13 | 1.05922 | 1.02000 | 0.95 | 3.00 | 7.46 | 0.893 | 60 |
| 14 | 1.01238 | 1.00344 | 0.98 | 3.03 | 1.76 | 0.904 | 89 |
| 15 | 1.09034 | 1.02008 | 1.03 | 4.59 | 12.22 | 0.952 | 51 |
| 16 | 1.04029 | 1.00810 | 1.00 | 4.54 | 5.40 | 0.955 | 57 |
| 17 | 1.04997 | 1.01010 | 1.02 | 4.57 | 6.78 | 0.990 | 57 |
| 18 | 1.04008 | 1.00700 | 1.00 | 4.65 | 5.37 | 1.052 | No |
| 19 | 1.03988 | 1.01030 | 0.91 | 2.94 | 4.87 | 1.083 | No |
| 20 | 1.11020 | 1.01988 | 1.01 | 4.56 | 14.58 | 1.155 | No |
| 21 | 1.05963 | 1.01012 | 1.01 | 4.54 | 7.97 | 1.174 | No |
| **22** | 1.07565 | 1.01081 | 0.80 | 4.25 | 7.97 | 1.180 | No |
| 23 | 1.01338 | 1.00097 | 0.96 | 4.47 | 1.85 | 1.277 | No |
| 24 | 1.03970 | 1.00500 | 0.96 | 4.41 | 5.01 | 1.417 | No |
| 25 | 1.07975 | 1.00976 | 1.01 | 4.79 | 10.61 | 1.510 | No |
| 26 | 1.04020 | 1.00196 | 0.96 | 4.41 | 5.17 | 2.624 | No |
| 27 | 1.04051 | 1.00106 | 0.99 | 4.47 | 5.36 | 3.547 | No |

Table 2.1: Experimental parameters. Experiments **22**, **9** and **2** correspond to the experiments shown in figures 2.3, 2.4 and 2.6, respectively.

(a) Snapshot, $t = 0.7\,\mathrm{min}$
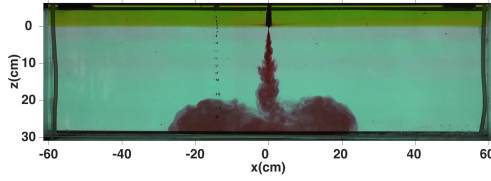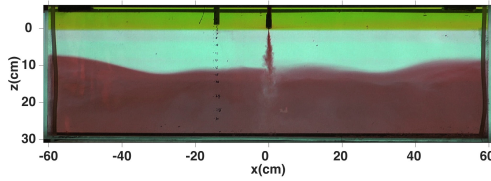
(d) Vertical time series, $x = -20\,\mathrm{cm}$

(b) Snapshot, $t = 3\,\mathrm{min}$

(e) Vertical density profiles, $x = -15\,\mathrm{cm}$

(c) Snapshot, $t = 60\,\mathrm{min}$
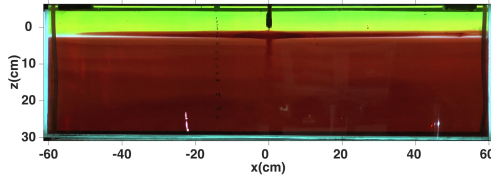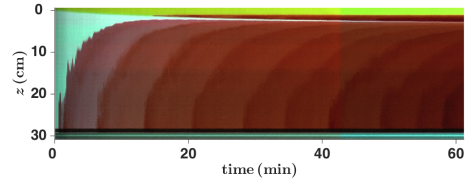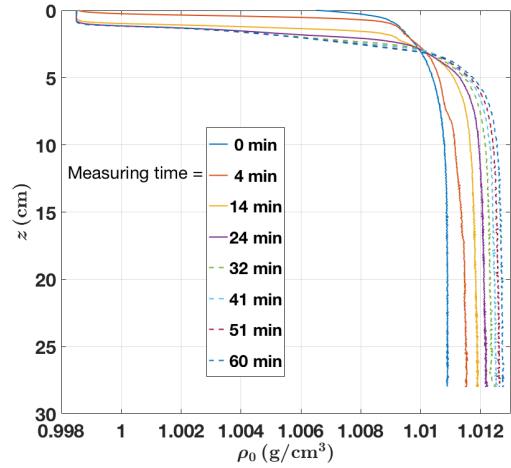
Figure 2.3: Snapshots from a classical filling box type experiment (Expt. 22 in table 2.1), with $\lambda = 1.180$, taken at time (a) $0.7\,\mathrm{min}$, (b) $3\,\mathrm{min}$ and (c) $60\,\mathrm{min}$. For future reference, note that the upper layer thickness is measured from the base of the nozzle, not the free surface. (d) Vertical time series collected at $x = -20\,\mathrm{cm}$. For flow visualization purposes, red dye is injected into the plume every $3\,\mathrm{min}$ at the start of the experiment and every $6\,\mathrm{min}$ thereafter. (e) Density profiles measured at the times indicated.

Kaye (2001). For the experiments of table 1, $z_v \lesssim 0.2\,\mathrm{cm}$ which is an order of magnitude smaller than the terminal upper layer thickness. Based on this observation, it is sufficient and convenient to set the elevation of the nozzle tip as the origin, $z = 0$.

With $\lambda = 1.180$, the plume is expected to descend to the tank bottom for all times, a fact confirmed by figures 2.3 (a)-(c). Shortly after the start of the experiment (figure 2.3 (a)) the plume arrived at the tank bottom and then spread as a gravity current until it reached the side walls. The first front (figure 2.3 (b)), which demarcates the interface between discharged plume fluid and uncontaminated lower layer fluid, ascended continuously because the plume volume flux per unit width at the first front was greater than $Q_{\mathrm{sink}}$. The fluid below the first front remained continuously stratified, as indicated by the density profile collected at 4 min (figure 2.3 (e)). Thereafter the first front ascended to a terminal elevation of 2.60±0.07 cm, at which elevation the plume volume flux through the front was balanced by the volume flux of the sink at the tank bottom. After the upper layer reached a depth of 0.78±0.07 cm, the plume began to split and an interfacial gravity current was formed. As confirmed by figure 2.3 (c), however, the depth of the resultant intermediate layer remained modest and the plume continued to fall all the way to the bottom boundary for the entire duration of the experiment, about an hour.

Vertical time series were constructed from the experimental video by stacking together a series of vertical slices (one pixel wide) taken at $x = -20\,\mathrm{cm}$ from successive video frames, as shown in figure 2.3 (d). This panel makes clear the progressive deepening of the upper layer from 0 cm to 0.98±0.07 cm. The terminal depth in question may be compared with the predicted depth $H_{u\infty}$ using (2.22). Assuming $\alpha = 0.1$, we predict $H_{u\infty} = 0.84\,\mathrm{cm}$, which is in reasonable agreement with the measured value.

Figure 2.3 (e) shows density profiles taken at successive times. Profiles collected after a significant time had elapsed confirmed that the upper fresh water layer reached a terminal depth of approximately 1.0 cm, measured from the

base of the plume nozzle. Below this depth the ambient consisted of a gradually thickening interface and a lower-layer whose density, nearly uniform in $z$, increased slowly with time, $t$.

An experiment exhibiting a transition to an interfacially spreading plume is shown in figure 2.4. The experimental parameters correspond to those given for Expt. 9 in table 2.1 and are comparable to those of Expt. 22 (shown in figure 2.3) except that the plume source density, $\rho_s$, is smaller by $0.02\,\mathrm{g\ cm^{-3}}$. The smaller value of $\rho_s$ results in a decrease of $F_s$ to $5.49\,\mathrm{cm^3\ s^{-3}}$, and a corresponding decrease of $\lambda$ to 0.791. Although $\rho_s > \rho_l$, because $\lambda$ is less than unity it is anticipated that the plume will eventually spread entirely at or above the interface of the two layer ambient, intruding within an intermediate layer.

At early times (figure 2.4 (a)), the plume descends to the bottom as before. After $\sim 10\,\mathrm{min}$, the plume splits at the interface to form an intrusion that propagates to $x =$-20 cm at $10\,\mathrm{min}$ (figure 2.4 (b)). Later, the plume spreads entirely within this intermediate layer, as shown in figure 2.4 (c). We refer to the process by which the intrusion evolves first from a splitting intrusion (with some plume fluid continuing to penetrate through the lower ambient layer) to a spreading intrusion (with no plume fluid falling into the lower layer) as the "transition." The time $t_t$ corresponds to the end of the transition process and can be estimated from movies of the experiments by noting the time at which the red fluid injected into the plume first spreads entirely above the lower layer. For the experiment shown in figure 2.4, $t_t \simeq 35\,\mathrm{min}$ with an error of $\pm 3\,\mathrm{min}$. The end of the transition can be determined more accurately from vertical time series images (e.g. figure 2.4 (d)) by tracking the rate of descent of the interface between the intermediate and lower layers. When the transition is complete, no plume fluid penetrates all the way through the interface at the top of the lower layer. As a result, there is no fountain top entrainment that would otherwise transport lower layer fluid to the interface (Kumagai, 1984). If we consider the fluid below the interface as a control volume, then following transition a constant outflow from this volume due to the bottom sinks results in a steady

34

descent of the interface at speed $Q_{\text{sink}}/L_T = 0.005\,\text{cm s}^{-1}$. After locating the time-variable interface depth from the vertical time series, we find the best-fit line at later times when the interface is observed to descend at a constant speed. Separately, we fit a degree five polynomial to the interface depth versus time plot at early times. The intersection of the best-fit line and polynomial gives $t_t$. For the experiment shown in figure 2.4, $t_t = 36\pm1\,\text{min}$. This measurement is characteristic of other experiments, i.e. $t_t$ is typically on the order of tens of minutes. If no transition occurred after two hours (for most experiments), it was deemed that transition would never occur.

The time for the start of transition is also estimated from the vertical time series. From the aforementioned best-fit line to the late-time interface depth versus time, we extrapolated backward in time to find the intersection of this line with $z = 0$, indicating the elevation of the source. This point of intersection defines a "virtual time", $t_v$. For the experiment shown in figure 2.4, $t_v = 11\,\text{min}$. If we imagine a similar experiment starting from $t = t_v$ with $F_s = 0$, so that the plume is in fact a jet, the ambient interface will descend with the constant rate $Q_{\text{sink}}/L_T$ from the beginning. After time $t_t - t_v$ the ambient interface will exactly overlap the ambient interface shown in figure 2.4 (d). The virtual time is therefore the time delay of the real experiment with $F_s > 0$ from an analogue experiment with $F_s = 0$. From this point of view, we can also consider $t_v$ as the approximate onset (or start) time of the transition process.

For the experiment shown in figure 2.4, the green-dyed upper layer deepened to a measured value of $H_{u\infty} = 0.94 \pm 0.07\,\text{cm}$. This was consistent with the prediction of $0.96\,\text{cm}$ obtained from (2.22) with $\alpha = 0.1$.

Although the first front moved upwards for $t < 10\,\text{min}$ (figure 2.4 (d)), it later moved downwards as splitting occurred because $Q_{\text{sink}}$ exceeded the plume volume flux per unit width through the first front. After transition, when the plume stopped penetrating into the lower layer, the first front descended at the same rate, $Q_{\text{sink}}/L_T$, as the interface.

Figure 2.4 (e) shows the density profiles measured with the conductivity

(a) Snapshot, $t = 0.7\,\mathrm{min}$

(b) Snapshot, $t = 10\,\mathrm{min}$

(c) Snapshot, $t = 60\,\mathrm{min}$

(d) Vertical time series, $x = -20\,\mathrm{cm}$

(e) Vertical density profiles, $x = -15\,\mathrm{cm}$
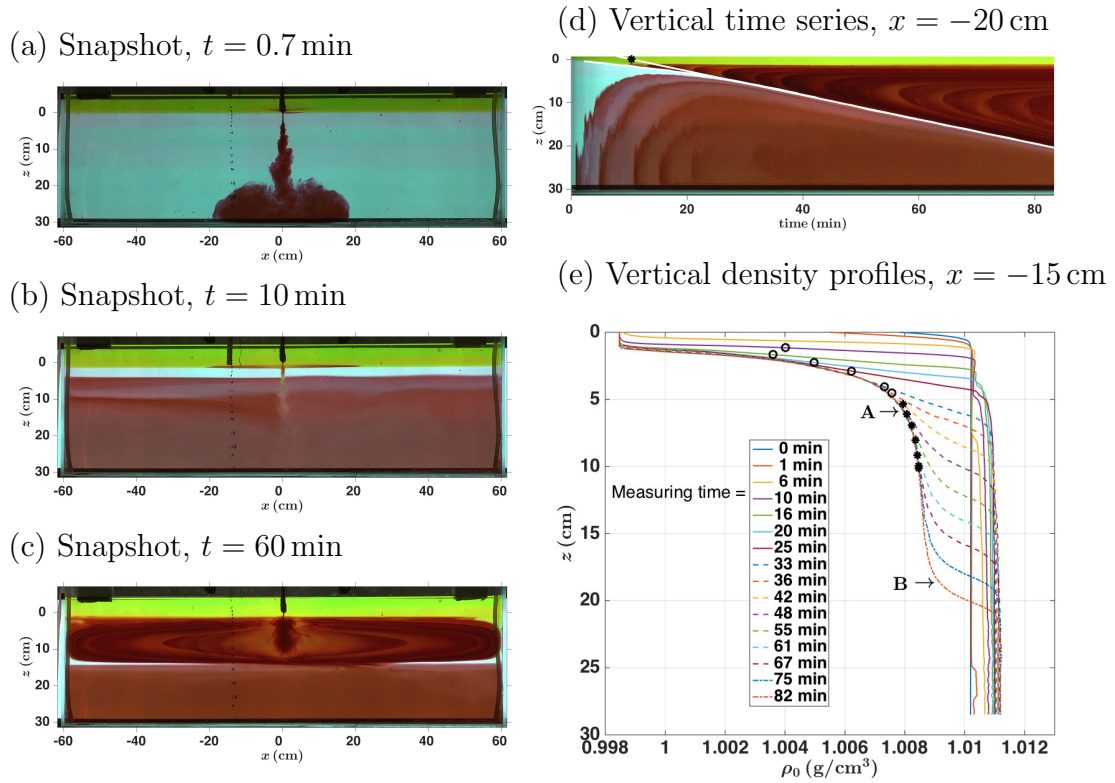
Figure 2.4: As in figure 2.3, but for an experiment with $\lambda = 0.791$ (Expt. 9 in table 2.1). In panel (d), the extrapolation of the interface between the intermediate and lower layers is intersected by the $x$ axis, from which the virtual time, $t_v = 11\,\mathrm{min}$ can be found. In panel (e), the $\circ$ and $*$ markers indicate the measured depths of the splitting and spreading intrusions, respectively, for each applicable time. The locations denoted by 'A' and 'B' indicate the upper and lower depths, respectively, bounding the intermediate layer of fluid formed by the intrusion at $t = 82\,\mathrm{min}$.

probe at different times. Before the transition was complete the ambient re-sembled a two-layer stratification. The ambient thereafter evolved towards a three-layer profile. The intermediate layer was formed by the intrusion, whose steady state density, $\bar{\rho}(H_{u\infty})$, can be estimated using (2.12). Given $z = H_{u\infty}$ and $Q(H_{u\infty}) = Q_{\text{sink}}$,

$$\bar{\rho}(H_{u\infty}) = \rho_u \left( \frac{\bar{g}'(H_{u\infty})}{g} + 1 \right) = \rho_u \left( \frac{F_s}{g\, Q_{\text{sink}}} + 1 \right). \tag{2.26}$$

For the experiment shown in figure 2.4, the mean density calculated from (2.26) is $1.0083\,\text{g cm}^{-3}$. We compare this prediction with measured values taken at $t = 82\,\text{min}$ at depths between points A and B in figure 2.4 (e). Consistent with (2.26), the mean density of the intermediate layer is measured to be $\rho_{\text{int}} = 1.0085 \pm 0.0003\,\text{g cm}^{-3}$. The time-variable intrusion depth can be inferred from the right-hand side of figure 2.4 (d) as the left-most point of the sideways parabola-like red curves that appear between the upper (green-dyed) layer and the lower layer. These intrusion depths are superimposed as symbols plotted on the density profiles in figure 2.4 (e), showing that the intrusion descended at a level close to the middle of the near-uniform middle layer. The positions of the fronts of the first-observed interfacial gravity currents are tracked at different times and are plotted in the $x - t$ plane, as shown in figure 2.5. The data points satisfying $|x| < 30\,\text{cm}$ are fitted with a pair of best-fit lines, whose slopes indicate the (approximately constant) initial speeds of propagation. The small difference between the speed of the leftward propagating current, $0.067 \pm 0.002\,\text{cm s}^{-1}$, and that of the rightward propagating current, $0.064 \pm 0.002\,\text{cm s}^{-1}$, may reflect a slight asymmetry in the rate of freshwater injection in the upper layer. For the experiments in which transition occurred, the average of the left and right front speeds shall be denoted by $U_{\text{intr}}$.

For the experiment shown in figure 2.6, the source density is $\rho_s = 1.02697\,\text{g cm}^{-3}$. The corresponding source buoyancy flux per unit width is $F_s = 2.24\,\text{cm}^3\,\text{s}^{-3}$, and $\lambda = 0.320$ (see Expt. 2 of table 2.1). Consistent with expectations, the experiment shows a faster transition compared to the experiment exhibited in figure

37
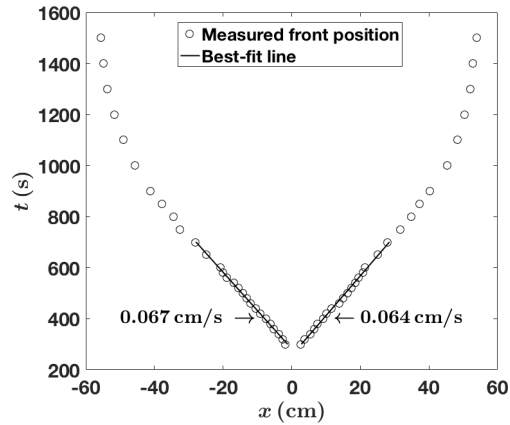
Figure 2.5: Intrusion front location vs. time (Expt. 9 in table 2.1). The slopes of the best-fit lines show the initial propagation speeds of the splitting intrusion in the left and right directions.

(a) Snapshot, $t = 0.7\,\mathrm{min}$
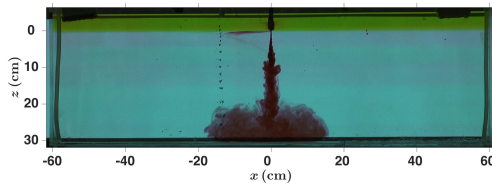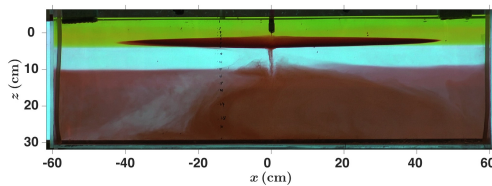
(d) Vertical time series, $x = -20\,\mathrm{cm}$

(b) Snapshot, $t = 17\,\mathrm{min}$

(e) Vertical density profiles, $x = -15\,\mathrm{cm}$

(c) Snapshot, $t = 60\,\mathrm{min}$
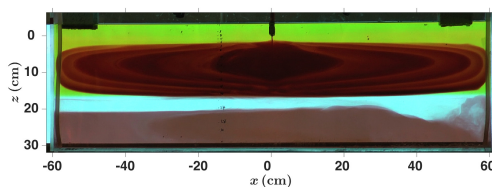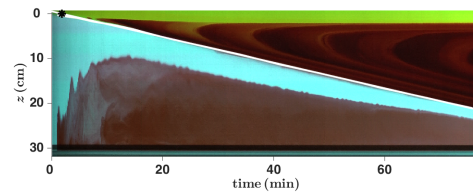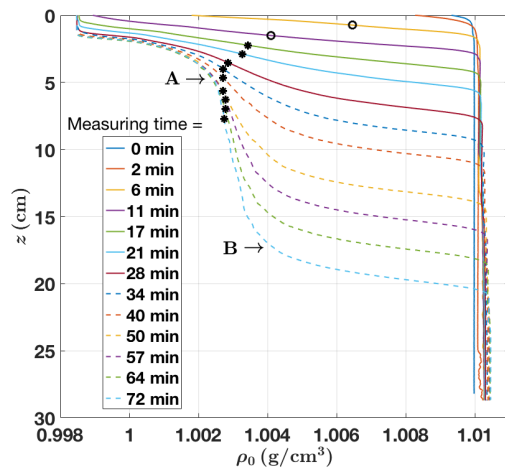


Figure 2.6: As in figure 2.4, but for experiment with $\lambda = 0.320$ (Expt. 2 in table 2.1).

2.4. Here, $t_v \simeq 2.2\,\mathrm{min}$ and the transition is complete after $t_t = 20\,\mathrm{min}$. Thereafter the interface descends at the same rate of $0.005\,\mathrm{cm\ s^{-1}}$ as seen for Expt. 9. The density profiles are shown in figure 2.6 (e). Following transition, a three-layer stratification evolved from a two-layer stratification as observed in the experiment shown in figure 2.4. From (2.26), we expect $\bar{\rho}(H_{u\infty}) = 1.0024\,\mathrm{g\ cm^{-3}}$. The mean density of the intermediate layer is calculated from the last measured profile at $t = 72\,\mathrm{min}$ over the range between points A and B indicated in figure 2.6 (e). We find that $\rho_{\mathrm{int}} = 1.0030 \pm 0.0002\,\mathrm{g\ cm^{-3}}$, which agrees reasonably well with the predicted value.

## 2.4.2 Quantitative results

The value of the ambient fluid density measured at the deepest depth, $z = 28\,\mathrm{cm}$, from figure 2.3 is plotted against time in figure 2.7. For sake of comparison, figure 2.7 also contains an analogue filling box prediction computed using the Germeles algorithm (Germeles, 1975). In drawing the solid curve, we have assumed an ideal plume and have applied the same source buoyancy flux but have presumed a uniform ambient having the same density as that of the lower layer from the experiment. The significant deviations between this solid curve and the experimental data points for $t \gtrsim 500\,\mathrm{s}$ affirm the nontrivial influence of the deepening upper layer and the commensurate transport of upper layer fluid to depth by the plume.

A series of experiments were run with a range of parameters as listed in table 2.1. Figure 2.8 shows a regime diagram indicating whether or not transition occurred; measurements are plotted in the $g'_{ul} - \lambda$ plane. Experiments that did and did not include transition are drawn, respectively, with circles and squares. In the former case, the circle radius indicates the time, $t_t$, needed to complete the process of transition. In section 2.2.5, it was argued that $\lambda = 1$ ought to represent a dividing line in such regime diagrams. Figure 2.8 confirms that this interpretation is accurate. As expected, the figure also confirms that $t_t$ generally increases with $\lambda$ for $0 < \lambda < 1$.
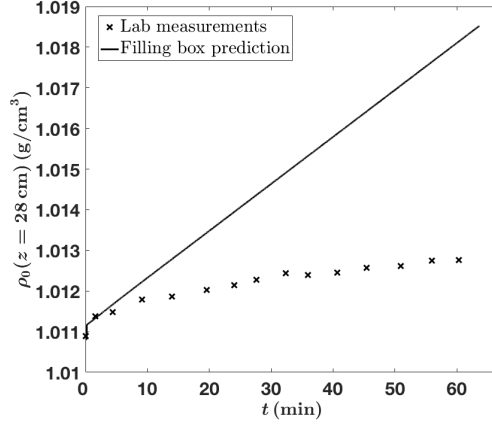
Figure 2.7: Ambient fluid density measured at a depth of $z = 28\,\mathrm{cm}$ for the experiment shown in figure 2.3. A corresponding filling box prediction in which the upper layer is omitted is plotted as the solid line.
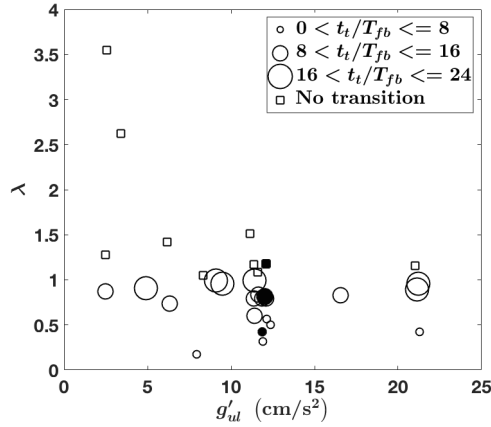


Figure 2.8: Regime diagram indicating transition vs. no transition for the experiments described in table 2.1. Here $\lambda$ is given by (2.24) and $g'_{ul} = g\frac{\rho_l - \rho_u}{\rho_u}$ is the reduced gravity between the ambient upper and lower layers. Moreover, $t_t$ is the end of transition time and $T_{fb}$ is given by (2.15). The solid symbols correspond to the experiments shown in figures 2.3, 2.4 and 2.6, respectively, with decreasing $\lambda$.

(a) Virtual time            (b) End of transition time
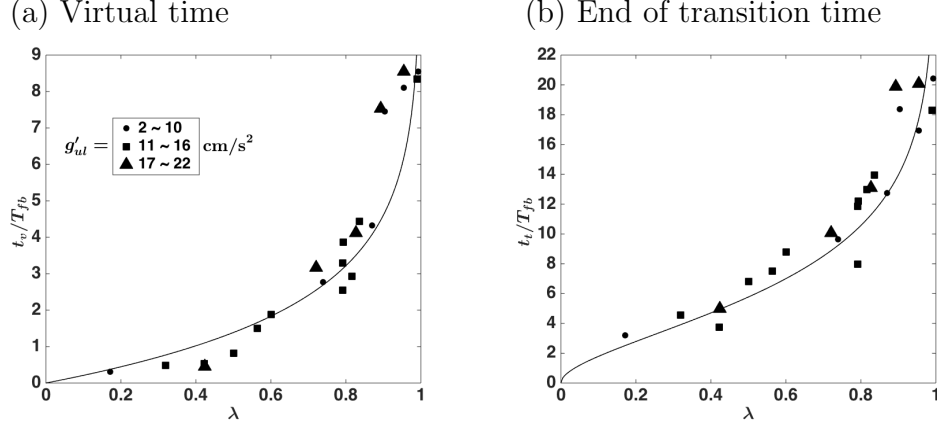
Figure 2.9: Non-dimensional virtual time and end of transition time vs. $\lambda$. Both times are normalized by the filling box time $T_{fb} = (2\alpha)^{-2/3} L_T F_s^{-1/3}$ with $\alpha = 0.1$.

For the experiments wherein transition occurred, figure 2.9 shows the values of $t_v$ and $t_t$ (normalized by the filling box time, $T_{fb}$) plotted against $\lambda$. For a wide range of $g'_{ul}$, the data collapse well, which indicates that $\lambda$ is the appropriate parameter for characterizing the plume splitting and transition processes. Both $t_v$ and $t_t$ become very large compared with the filling box time as $\lambda \to 1^-$. The relative loss of the plume buoyancy flux decreases as $\lambda$ increases and thus it takes more time for the transition to initiate and to complete. To help generalize the results, figure 2.9 includes empirically fit curves to the data, which have the following respective equations:

$$\frac{t_v}{T_{fb}} = (-2.16 \pm 0.25) \log(1 - \lambda), \qquad \frac{t_t}{T_{fb}} = (-4.63 \pm 0.48) \log(1 - \lambda^{1/2}). \quad (2.27)$$

Also for the experiments with transition, the mean steady state density, $\rho_{\text{int}}$, of the intermediate layer is plotted against $F_s / (g\, Q_{\text{sink}})$ in figure 2.10. The data collapse well with the prediction of (2.26), which confirms that $\rho_{\text{int}}$ is independent of $\rho_l$ and the tank dimension.

Images like figure 2.6 (b) suggest that a significant amount of plume fluid may accumulate along the interface even before transition. Because this discharged plume fluid contains solute (and, in the marine outfall scenario, aqueous pollution), it is desirable to estimate the mass of solute, $M_{\text{int}}$, within the intermediate

41
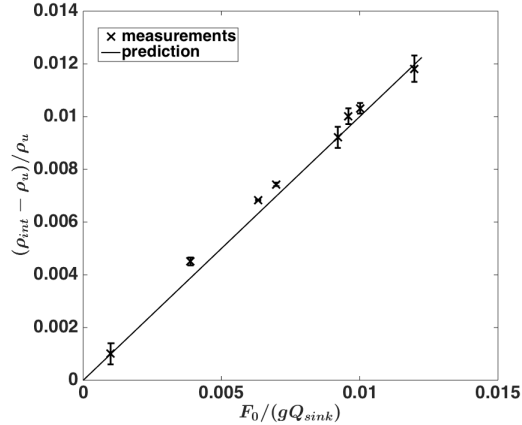
Figure 2.10: Mean steady state density of the intermediate layer in those experiments where transition occurred. The straight line indicates the prediction of (2.26).

layer in question at time $t_t$. This information can be gleaned from the conductivity probe data. Care is taken to discount any solute present in the (diffuse) interface at the initial time. Figure 2.11 plots $M_{\text{int}}$ versus $\lambda$ where the former variable has been normalized by $M_{\text{total}}$, the total mass of solute supplied by the plume source over $0 \leqslant t \leqslant t_t$. Before the onset of splitting, all the plume fluid falls through the lower layer. With larger $\lambda < 1$, it takes more time for splitting to initiate. Thus more plume fluid descends to the bottom boundary as a result of which $M_{\text{int}}/M_{\text{total}}$ is less than in experiments where $\lambda$ is small and splitting occurs earlier, albeit with intermediate fluid whose density may be little larger than $\rho_u$. When applied to the marine outfall example discussed previously, this tells us that the relative amount of pollution that can be carried to the surface will increase with $\lambda$.

After transition, discharged plume fluid intrudes roughly in the middle of the intermediate layer as shown in figures 2.4 (d) and 2.6 (d). Of course, the intermediate layer thickens over the duration of the experiment and hence the depth at which plume fluid discharges as an intrusion descends with time. Figures such as 2.4 (d) and 2.6 (d) show that the rate of descent, $W_{\text{intr}}$, is approximately constant; accordingly, a unique value for $W_{\text{intr}}$ can be calculated for each ex-

42
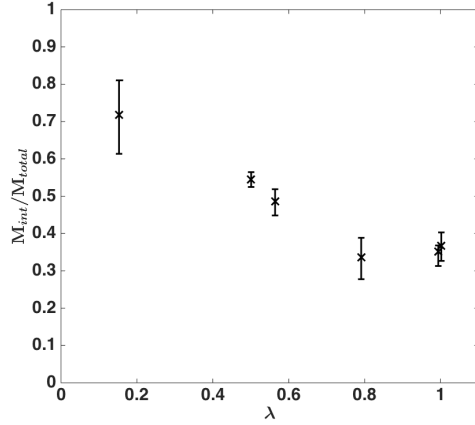
Figure 2.11: Ratio of the solute mass in the intermediate layer, $M_{\text{int}}$, at $t_t$ to the total mass of solute, $M_{\text{total}}$, injected by the nozzle during $0 \leqslant t \leqslant t_t$.
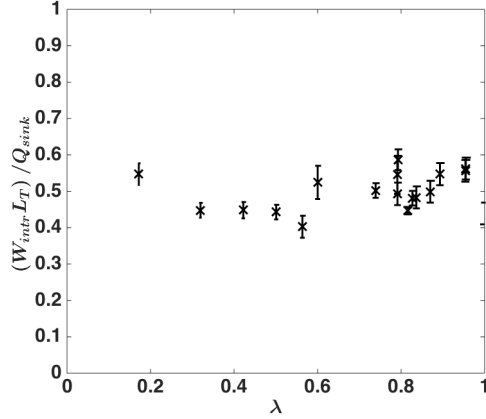


Figure 2.12: Descent rate, $W_{\text{intr}}$, of the intrusion spreading depth vs. $\lambda$.

periment in which transition occurred. In figure 2.12, we plot $W_{\text{intr}}$ against $\lambda$. Considering the symmetric geometry of the intrusion (e.g. see figure 2.4 (c), 2.6 (c)), approximately one-half of the intrusion fluid lies below the intrusion depth, and $W_{\text{intr}}$ is approximately $0.5(\pm 0.1)\, Q_{\text{sink}}/L_T$.

Whereas figure 2.12 considers the vertical descent of the intrusions, figure 2.13 shows the variation of $U_{\text{intr}}$ with $\lambda$. Studies of intrusions often non-dimensionalize the front speed using, as a characteristic vertical length scale, the intrusion height. We find it more instructive, however, to non-dimensionalize $U_{\text{intr}}$ with $\alpha F_s^{1/3}$. So normalized, and although there is some scatter in the data,
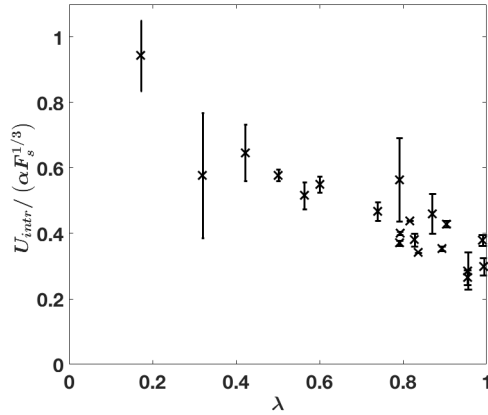
Figure 2.13: Normalized intrusion front speed, $U_{\mathrm{intr}}$, vs. $\lambda$. In some experiments with large $Q_u$, the asymmetries in the fresh water influxes at the two ends of the tank were large and introduced large errors indicated by the comparatively long lengths of the vertical error bars.

the front speed decreases approximately linearly with increasing $\lambda$. The qualitative trend of the data from figure 2.13 can be understood by referring to figures 2.4 (b) and 2.6 (b), which suggest that thicker and faster advancing intrusions are associated with smaller values of $\lambda$. Taken together, the marine outfall implication of figures 2.11 and 2.13 is as follows: with smaller $\lambda$, more passive scalars accumulate in the vicinity of the pycnocline and their lateral transport along the pycnocline and away from the point of vertical convection is larger.

## 2.5   Discussion and conclusions

We have examined the influence of a deepening upper layer on the behaviour of a line-source plume that falls through a two-layer stratified ambient fluid. Depending upon the relative loss of buoyancy flux of the plume at the interface, which we express using the parameter $\lambda = F_s / \left( g'_{ul} \, Q_{\mathrm{sink}} \right)$, either a bottom propagating gravity current develops and persists (if $\lambda > 1$) or the plume splits then spreads entirely as an intrusion that propagates between the upper and lower layers (if $\lambda < 1$). During plume splitting some fraction of the plume fluid discharges once the upper layer depth surpasses a critical value. Unlike the ex-

periments of Kumagai (1984) and Mott & Woods (2009), which examined the eventual breakthrough of a plume at an interface due to solute accumulation, an opposite transition process is observed in many of our laboratory experiments. Specifically, the plume evolves from total penetration to partial discharge (splitting) to complete discharge with interfacial spreading occurring in a deepening intermediate layer of roughly constant density.

Because initially a plume entrains upper-layer fluid and carries it to depth, the ambient interface descends more slowly at first than it would if the source were a jet ($F_s = 0$), which does not penetrate the interface. However, if a jet source flow was initiated at the virtual time $t = t_v$ rather than $t = 0$, the ambient interface would, in due course, overlap with the descending ambient interface observed in our experiments employing plumes. This is the way in which we consider $t_v$ to represent the approximate onset of the transition process, and $t_t$ to represent the corresponding end where no plume fluid reaches the lower layer. As shown in figure 2.9, $t_v$ and $t_t$ normalized by the filling box time $T_{fb}$ collapse well when plotted against $\lambda$ and both become very large as $\lambda \to 1^-$.

Although our experiments are highly idealized, they can provide further insights into some important environmental flows. Consider again the outflow of aqueous pollutants in Massachusetts Bay. The outfall tunnel extends 13 km offshore and is connected to a 2 km long diffuser which is located along the seafloor. The effluent is discharged through 55 risers into the sea whose local depth is approximately 34 m. The average volume flux of the waste water from all 55 risers is $16.0\,\mathrm{m}^3\,\mathrm{s}^{-1}$ and the waste water density is taken as 1.0 g cm$^{-3}$ (Hunt *et al.*, 2010; Roberts *et al.*, 2011). From surveys conducted in summer (Hunt *et al.*, 2002), the stratification in Massachusetts Bay can be represented approximately as a two-layer fluid with a 10 m upper layer of density 1.0226 g cm$^{-3}$ and a 24 m lower layer of density 1.0245 g cm$^{-3}$ such that $g'_{ul} = 0.018\,\mathrm{m}\,\mathrm{s}^{-2}$. Moreover, the buoyancy flux per unit length of the diffuser is taken to be $F_s = 0.019\,\mathrm{m}^3\,\mathrm{s}^{-3}$. Also from equation (2.12), the reduced gravity of the plume varies with elevation $z$ as $\bar{g}'(z) = 0.21\mathrm{m}^2\,\mathrm{s}^{-2} \times z^{-1}$ where $z = 0$ corresponds to the seafloor.

Accordingly, the reduced gravity of the plume at the interface ($z = 24\,\mathrm{m}$) is $0.0087\,\mathrm{m\ s^{-2}}$. From equation (2.18), $\Lambda = 0.48$ which signifies that the plume will be arrested below the upper layer. As winter approaches, and due to surface cooling and wind forcing, the water column becomes well mixed. The interface steadily approaches the seafloor and the ambient reduced gravity decreases. Both of these factors serve to increase $\Lambda$. Although the directionality of the interface advance relative to the source is opposite to that in our experiments, the present results apply because the interface vertical velocity is small. We anticipate that plume splitting should occur as $\Lambda$ approaches unity, and complete transport of the pollutants to the free surface should occur for $\Lambda > 1$.

Another similar, albeit inverted, example concerns the displacement ventilation of a building containing low-level and high-level vents to the exterior. We consider a ground-level heat source such as a piece of electrical equipment that generates an ideal plume having a buoyancy flux per unit width, $F_s$. The plume ascends to the ceiling at $z = H$ and discharges its fluid to form an upper layer where the reduced gravity, $g'_{ul}$, between the upper and lower ambient layers is identical to the reduced gravity of the plume $\bar{g}'(H)$ measured at the ceiling at $t = 0$. Over time, the interface descends towards the source before reaching a terminal elevation, $h$, which is prescribed by the area of the upper and lower vents and the height of the building zone (see (2.11) of Linden et al. 1990). Applying (2.9) with $z = h$ and (2.12) with $z = H$ into (2.24), we find that $\lambda = H/h > 1$. Thus transition and outflow of the plume along the ambient interface cannot occur as indeed has been observed experimentally (Linden *et al.*, 1990). However, if after steady state is achieved the heat source is turned down and the outflow rate, $Q_{\mathrm{sink}}$, through the high-level vent is enhanced artificially by a ratio greater than $H/h$, (e.g. using an extraction fan), then $\lambda$ can fall below unity. In this scenario, transition is anticipated and a three-layer stratification will develop.

In the Introduction, we presented a qualitative description for plume splitting along the ambient interface and thereby emphasized the importance of a

non-uniform density distribution over the plume cross section. Efforts to model the plume splitting analytically have been pursued; in particular, we attempted to parameterize the fraction of the plume fluid that would "split" (and therefore discharge along the ambient interface) given Gaussian distributions for velocity and density. At early times when the ambient interface is sharp, the calculation is straightforward and the total volume and density of discharged fluid can readily be obtained. Complications arise, however, for larger times when the sharp ambient interface must be replaced by a zone of continuous stratification. In this latter case, the plume splitting behaviour depends on the local buoyancy frequency of the ambient as well as the local reduced gravity of the plume. Future work will aim to more satisfactorily model the time evolution of the splitting process. Ultimately, we wish to derive a parameterization of the plume splitting process that can be straightforwardly incorporated into a filling-box model.

# Chapter 3

# Plume in rotating two-layer stratified fluid

## Summary

A descending plume in a rotating two-layer stratified ambient fluid is investigated experimentally. In most experiments, the source buoyancy flux of the plume is set to be small so that the mean density of the plume impinging the interface is less than the lower layer density, characterized by the buoyancy parameter, $\Lambda$, being less than unity. In such cases, the discharged plume fluid spreads radially at the interface in the form of an intrusive gravity current at early times. At later times, this intrusion evolves to form an anticyclonic lens due to the influence of the Coriolis force. The measured radial position of the intrusion front, $R(t)$, follows a power law relation against time, $t$, with a 3/4 power in the gravity current regime and, later, a 1/4 power after the intrusion evolves into a quasi-geostrophically balanced lens. The plume reaching the interface progressively increases its density due to re-entraining relatively dense fluid by descending through the lens. Consequently, the plume penetrates through the interface and descends to the bottom of the tank except in cases where the lens is unstable. Faster rotation makes the lens thicker and hence increases the volume of the re-entrained fluid, which decreases the time for onset of penetration. On the other hand, rotation indirectly decreases the average fountain-head entrainment rate from the lower layer, which has the opposite effect of retarding

penetration. With the combination of these two competing influences, we find that the non-dimensional penetration time follows a power law versus $\Lambda$. By extension, the average rate of fountain-head entrainment, $\bar{E}_i$, is measured and the ratio of $\bar{E}_i$ to the corresponding theoretical value $E_i$, derived in the limit of no rotation, is found to vary systematically with the Rossby number measured at the interface.

## 3.1  Introduction

Turbulent plumes have been well investigated since the seminal study of Morton *et al.* (1956), referred to hereafter as MTT, who developed an integral model for a plume in a semi-infinite domain with the effects of background rotation being ignored. This model was adapted by Baines & Turner (1969) to account for the evolution of a plume in an ambient fluid of finite size. As the plume reached the opposite (horizontal) boundary, being a solid surface in the case of a descending plume or a solid surface or free interface in the case of an ascending plume, the fluid from the plume spread horizontally to the walls of the control volume and then a stratified layer formed. This stratified layer progressively thickened as a result of the continual discharge of plume fluid. The plume itself was modified through entrainment of the resulting time-varying ambient fluid.

More recently the evolution of plumes in a two-layer ambient fluid has been studied through laboratory experiments (Kumagai, 1984; Mott & Woods, 2009; Ma *et al.*, 2017). In order to classify whether the plume is capable of penetrating through the interface at a distance $z = H_u$ from the virtual origin, a buoyancy parameter was introduced by Mott & Woods (2009) as $\Lambda = g'(H_u)/g'_{ul}$. Here $g'(H_u) = g(\rho(H_u) - \rho_u)/\rho_{00}$ is the reduced gravity of the downward-propagating plume relative to upper layer fluid, in which $\rho(H_u)$ is the plume density immediately above the ambient fluid interface. Meanwhile $g'_{ul} = g(\rho_l - \rho_u)/\rho_u$ is the reduced gravity of the lower layer of density $\rho_l$ with respect to the upper layer of density $\rho_u$. In both expressions, $g$ is gravitational acceleration and $\rho_{00} = \rho_u$ is chosen to be the characteristic density. When $\Lambda < 1$, meaning the plume

at the interface is initially lighter than the lower layer, the plume fluid spreads horizontally at the interface. Kumagai (1984) and Mott & Woods (2009) regarded the ambient interface as a false bottom for a filling-box process that was restricted to the upper layer. Due to re-entrainment and fountain-head entrainment effects, the plume eventually penetrated through the interface when its density became larger than the fluid in the lower layer. In both of Kumagai (1984) and Mott & Woods (2009), the penetration onset time was found to be dependent on the horizontal cross-sectional area of the geometry and $\Lambda$. In a related study, Ma *et al.* (2017) investigated a line-source plume that descended into a two-layer ambient, in which the upper layer deepened in time due to a source of upper layer fluid (and a corresponding sink of ambient fluid at depth). Due to this deepening upper layer, $\Lambda(t)$ decreased in time starting from values well above unity. In experiments for which $\Lambda(t)$ fell below unity, the plume split at the interface such that a fraction of the plume fluid was detrained into the ambient forming an intrusive gravity current at the interface; any plume fluid not discharged in this way descended to the tank bottom. The formation of the intrusion accentuated the detrainment process until eventually all the plume fluid spread as an intrusion with none reaching the bottom.

When a downward descending plume impinges on an ambient interface where the lower layer is comprised of fluid having a greater density than the plume ($\Lambda < 1$), the plume may nonetheless overshoot the interface and return back as a fountain. During this process, there is entrainment of lower layer fluid. Baines (1975) suggested that the entrainment rate, $E_i$, by the fountain head was dependent solely on the interfacial Froude number defined as $\mathrm{Fr}_i = w_{Gc}(H_u)/\sqrt{b_G(H_u)g'_{ul}}$ where $w_{Gc}(H_u)$ and $b_G(H_u)$ are the centreline vertical velocity and the radius of the (Gaussian) plume at the interface level. Although Baines' model has been well-accepted in general terms, various researchers (Baines, 1975; Kumagai, 1984; Baines *et al.*, 1993; Lin & Linden, 2005) have provided different empirical formulas relating $E_i$ and $\mathrm{Fr}_i$. Shrinivas & Hunt (2014) reviewed previous work by others vis-à-vis this functional de-

pendence, and also presented theoretical models trying to establish a universal relation between $E_i$ and $\mathrm{Fr}_i$.

Another noteworthy aspect of the impingement process (whether the plume strikes a density interface or a rigid bottom) is that the vertical momentum is reduced to zero and the plume fluid deflects to propagate horizontally as an axisymmetric flow. In the present study, we investigate the interfacial intrusion sufficiently far from the impingement region, where the intrusion is momentum-dominated as argued by Kaye & Hunt (2007). In other words, the intrusions of interest here behave as a buoyancy driven gravity current, at least until Coriolis effects become important whereby the intrusion evolves to a quasi-geostrophically balanced state.

Of course background rotation has an influence not only on the fluid discharged by the plume at the ambient interface, but also on the descending plume itself. For example, in studies of plumes in a uniform density ambient fluid, Fernando *et al.* (1998) showed experimentally that the speed of descent of the plume front decreased for $t > 2.4/\Omega$, where $\Omega$ is the background rotation rate. They attributed this deceleration to the alteration by the Coriolis force of the horizontal flow induced by plume entrainment. This horizontal flow in the ambient fluid developed into a cyclonic circulation that retarded inflow and entrainment into the plume. This circulation of ambient fluid around the plume eventually broke down as a result of a baroclinic instability.

As found by Fabregat Tomàs *et al.* (2016) in numerical simulations and Frank *et al.* (2017) in laboratory experiments, near the source, background rotation may also induce anticyclonic precession to the plumes near the source. The frequency of precession, $\omega$, was measured by Frank *et al.* (2017) to be proportional to the angular frequency of rotation, $\Omega$, such that $\omega \approx (0.40 \pm 0.04)\,\Omega$. In a much smaller subset of experiments, Frank (pers. comm.) observed that the plume developed into a tubular cyclonic vortex (herein referred to as a "tornado"). In some of our experiments of rotating plumes in a two-layer fluid we also observed the occurrence of a tornado penetrating from the upper to lower

layer ambient fluid. The evolution of the plume was dramatically different in these cases, as a result of which we herein choose to focus on those experiments exhibiting the more typical precessing plume behaviour.

Just as in the non-rotating case, a plume in a rotating environment that encounters a solid bottom or impenetrable density interface, will spread axisymmetrically in the horizontal. However, rotation can substantially influence the consequent evolution of this discharged fluid. By point of comparison, axisymmetric gravity currents produced by lock release with background rotation were investigated by Ungarish & Huppert (1998) and Hallworth *et al.* (2001). The dense fluid was released from a hollow cylinder in a solid-body rotating ambient of light fluid. After geostrophic adjustment, a steady lens was formed and its shape was predicted with a shallow-water model. The gravitationally-converse scenario was studied by Griffiths & Linden (1981) who discharged light fluid upon the free surface of a dense ambient fluid in solid-body rotation. If the source volume flux was sufficiently small, the lens was at each moment in a quasi-steady state dictated by a balance of buoyancy, Coriolis and centrifugal forces.

There are few studies of plumes in a rotating stratified environment. This gap in the literature is somewhat surprising because any plume that evolves over long times and in sufficiently large domains must eventually become influenced by both the Coriolis force and stratification. Examples include giant volcanic eruptions (Baines & Sparks, 2005), vertical convection under polynyas (Okada *et al.*, 2004) and under-sea oil blowouts (Frank *et al.*, 2017). As alluded to above, we herein investigate a point-source plume impinging downwards upon a density interface of a two-layer ambient fluid in the presence of rotation. While in most experiments the plume is lighter than the lower layer when it first reaches the interface, unlike the experiments performed by Kumagai (1984) and Mott & Woods (2009), the radially spreading intrusion generated by the plume at the interface never advances all the way to the side boundaries; the Coriolis force limits the lateral spread of the discharged plume fluid. As a

consequence, the physical processes within the upper layer fluid are different from those captured by filling-box models adopted by Kumagai (1984) and Mott & Woods (2009). For instance, the time for the onset of penetration is no longer dependent on the cross-sectional area of the geometry, but instead depends on $\Omega$. In a similar fashion, the fountain-head entrainment is influenced by the Coriolis force through the formation and evolution of the anticyclonic lens. A major goal of our analysis is to resolve these details through laboratory experiments and thereby to provide a more complete picture of plume impingement on a density interface as it is influenced by rotation.

In Section 3.2, previous theories describing plumes in a non-rotating ambient fluid and intrusions in a non-rotating and rotating ambient fluid are summarized and adapted to the present experiments. These experiments are subsequently described: the setup of laboratory experiments and experimental results are presented in Section 3.3 and Section 3.4, respectively. Discussion and conclusions are given in Section 3.5.

## 3.2 Theory

In our study, a downward-propagating plume originates near the free surface and descends to the interface of a rotating two-layer ambient fluid. At early times, before there has been a significant re-entrainment of discharged plume fluid, the plume remains less dense than the lower layer ambient fluid and therefore spreads as an intrusive gravity current. Later, the Coriolis force deflects the radial advance of this intrusion and it evolves into a quasi-geostrophically balanced lens. In this paper, we reserve the term "lens" to mean an intrusive gravity current whose (late time) evolution is significantly impacted by Coriolis force.

### 3.2.1 Plume theory

**Plume in a uniform ambient**

In a uniform density ambient fluid without rotation, the volume flux, $Q(z)$, the reduced gravity, $g'(z)$, the vertical velocity, $w(z)$, and the radius, $b(z)$, of a top-hat plume are given by the MTT equations:

$$Q(z) = \frac{6\alpha}{5} \left(\frac{9\alpha}{10}\right)^{\frac{1}{3}} \pi^{\frac{2}{3}} F_s^{1/3} z^{5/3}, \tag{3.1}$$

$$g'(z) = \frac{5}{6\alpha} \left(\frac{10}{9\alpha}\right)^{\frac{1}{3}} \pi^{-\frac{2}{3}} F_s^{2/3} z^{-5/3}, \tag{3.2}$$

$$w(z) = \frac{5}{6\alpha} \left(\frac{9\alpha}{10}\right)^{\frac{1}{3}} \pi^{-\frac{1}{3}} F_s^{1/3} z^{-1/3}, \tag{3.3}$$

$$b(z) = \frac{6}{5}\alpha z, \tag{3.4}$$

(see Appendix B). Here $z$ is the vertical distance from the ideal plume source with the positive direction downwards, $F_s$ is the buoyancy flux from the ideal point-source and $\alpha$ is the entrainment coefficient; a typical value of $\alpha$ for a top-hat plume is taken to be 0.14 (Kumagai (1984), also see Appendix B). Finally $g'(z)$ is the reduced gravity of the plume with respect to the ambient fluid density.

**Plume in a two-layer ambient**

Kumagai (1984) and Mott & Woods (2009) considered a two-layer ambient where the upper layer has a density $\rho_u$ and depth $H_u$ and the lower layer has a density $\rho_l$ and depth $H_l$. Both studies considered a circumstance in which the initial density of the plume at the interface level ($z = H_u$) was less than the density of the fluid in the lower layer, so that the plume could not penetrate through the interface. This condition is expressed mathematically as $\Lambda < 1$ (Mott & Woods, 2009) where

$$\Lambda = \frac{g'(H_u)}{g'_{ul}}. \tag{3.5}$$

Here $g'_{ul} = g\left(\rho_l - \rho_u\right)/\rho_u$ is the reduced gravity between the upper and lower layers and $g'(H_u)$ is given by evaluation of (3.2), with the assumption that the

ideal plume source is situated at the top of the upper layer.

**Entrainment by a plume impinging on an interface**

Due to inertia, a plume with $\Lambda < 1$ can overshoot into the lower layer and then collapse as a fountain, before advancing as an intrusive gravity current along the interface. During these overshoot and collapse processes, some fluid from the lower layer is entrained and brought into the fountain. The rate of entrainment into the fountain head from the lower layer is characterized by the ratio

$$E_i = \frac{Q_{ent}}{Q(H_u)}. \tag{3.6}$$

Here, $Q(H_u)$ is determined from (3.1). Conversely, $Q_{ent}$ is the volume flux of fluid associated with fountain-head entrainment of lower layer fluid.

Most experimental studies showed that $E_i$ was solely dependent on the interfacial Froude number, $\mathrm{Fr}_i$, as suggested initially by Baines (1975). Explicitly, for a top-hat plume, $\mathrm{Fr}_i$ is given by

$$\mathrm{Fr}_i = 2^{5/4} \frac{w(H_u)}{\sqrt{b(H_u)g'_{ul}}}. \tag{3.7}$$

For large Froude numbers ($\mathrm{Fr}_i \geq 1.4$), Shrinivas & Hunt (2014) found that the fountain-head entrainment rate varies approximately linearly with $\mathrm{Fr}_i$, according to

$$E_i = 0.42\mathrm{Fr}_i. \tag{3.8}$$

For a point-source plume and employing (3.2) - (3.5), $\Lambda$ is expressed in terms of $\mathrm{Fr}_i$ as

$$\Lambda = \frac{\alpha}{5\sqrt{2}}\mathrm{Fr}_i^2 = 0.02\mathrm{Fr}_i^2, \tag{3.9}$$

in which $\alpha = 0.14$ has been used in this last expression. Substituting (3.9) into (3.8), yields

$$E_i \approx 2.97\Lambda^{1/2}. \tag{3.10}$$

As we shall describe in further detail below, (3.10) provides a helpful reference in characterizing the impact of rotation which is, of course, omitted in

the above analysis. The lens fluid, having a volume $V_{lens}(t)$, is composed of the volume $V_p(t)$ of fluid discharged by the plume and the volume $V_{ent}(t)$ of fluid entrained from the lower layer:

$$V_{lens}(t) = V_p(t) + V_{ent}(t), \tag{3.11}$$

where $V_{ent} = \int_0^t Q_{ent} \, \mathrm{d}t$. Meanwhile, the volume, $V_p(t)$, of plume fluid entering the top of the lens situated at a height $h_u$ above the interface can be computed from

$$V_p(t) = \int_0^t Q\left(H_u - h_u(t)\right) \mathrm{d}t. \tag{3.12}$$

Because the intrusion thickness increases in time, the plume gradually entrains less upper layer fluid and more discharged plume fluid during its descent. With (3.11) and (3.12) to calculate $V_{ent}(t)$ and using (3.6), the average fountain-head entrainment during a time period of $t$ is given by

$$\bar{E}_i = \frac{V_{ent}(t)}{Q(H_u)t}. \tag{3.13}$$

At early times, i.e. before a significant volume of plume fluid is discharged along the ambient interface, we expect $\bar{E}_i \simeq E_i$. For larger $t$, the fountain-head entrainment dynamics are expected to be modified by the formation of the intrusion, which may, in turn, be influenced by rotation. As a result, we expect $\bar{E}_i < E_i$.

**Effects of background rotation on the plume**

In principle, the Coriolis force can reduce the volume of fluid entrained into a plume by suppressing the horizontal motion of turbulent eddies. At depth $z$, the local characteristic length and velocity scales of the largest eddy within a plume are given by the radius, $b(z)$, and the mean vertical velocity, $w(z)$, respectively. The effect of the Coriolis force on an eddy of this size is characterized by a depth-dependent Rossby number defined as

$$\mathrm{Ro}(z) = \frac{w(z)}{f b(z)}, \tag{3.14}$$

where $f = 2\Omega$ is the Coriolis parameter. Substituting (3.3) and (3.4) into (3.14), yields

$$\mathrm{Ro}(z) = \frac{25}{72} \left( \frac{9}{10\pi\alpha^5} \right)^{1/3} \Omega^{-1} F_s^{1/3} z^{-4/3} \approx 6.0 \Omega^{-1} F_s^{1/3} z^{-4/3}. \qquad (3.15)$$

The minimum value of $\mathrm{Ro}(z)$ for the plume in the upper layer coincides with the interface level, $z = H_u$. In the experiments presented here, $\mathrm{Ro}(H_u) > 1$, so we can expect there to be comparatively little influence of rotation on entrainment by eddies. On the other hand, the Coriolis force can alter the direction of the ambient fluid being drawn radially inwards to the plume. Hence a cyclonic circulation may be formed around the plume particularly near the source, as observed by Fernando *et al.* (1998). Such a circulation will inhibit further entrainment of ambient fluid into the plume. Note, however, that Fernando *et al.* (1998) also found that the circulation around the plume became unstable in their experiments.

In most experiments of plumes in a rotating uniform density ambient, Frank *et al.* (2017) found the plume precessed anticyclonically near the source after a short initiation time. The influence of precession on ambient entrainment being unknown, we model the entrainment based on the vertical, not the along-flow, distance traversed by the plume.

### 3.2.2   Intrusive gravity current and lens

**Advance of non-rotating and rotating intrusions**

Kaye & Hunt (2007) investigated the flow driven by the impingement of a plume on a rigid bottom, modelling the radial outflow as jet-like near the site of impingement and gravity current-like in the far-field, taken to be at distances greater than 4.3 times the plume radius at the point of impingement. Far from this point, they obtained the same result as Britter (1979) for the radial advance of the flow front i.e. $R(t) = 0.84 \left( F_s t^3 \right)^{1/4}$, where $R(t)$ is the radial position of the intrusion front. Here we extend this result to include the effects of interfacial spreading at early times and rotation leading to lens formation at late

times. For small $t$ when rotation can be neglected, but presumably beyond the momentum driven regime, we suppose that the front advances radially as

$$R(t) \propto \left(F_s t^3\right)^{1/4}.$$  (3.16)

We expect the constant of proportionality to differ from 0.84 because the process of plume impingement on an ambient interface (rather than a solid boundary) entails fountain-head entrainment of lower layer fluid as described above. In the case of rotation-affected spreading we follow the scaling of Griffiths & Linden (1981) who derived expressions for the shape and radial extent of the anticyclonic lens. In particular, they found $R(t) = \sqrt{2}\left(\frac{F_s t}{\pi \Omega^2}\right)^{1/4}$. Generalizing this result, we estimate the radial position of the intrusive flow front at late times to be

$$R(t) \propto \left(\frac{F_s t}{\Omega^2}\right)^{1/4}.$$  (3.17)

In order to estimate the time at which rotation begins to influence the lateral spreading of the intrusion, it is helpful first to non-dimensionalize $t$ and $R(t)$ with $\Omega^{-1}$ and $(F_s/\Omega^3)^{1/4}$, respectively, which gives

$$\tau = \Omega t, \ \xi(\tau) = \frac{R(t)}{(F_s/\Omega^3)^{1/4}}.$$  (3.18)

We then combine (3.16) and (3.17) under the assumption that the transition from the gravity current regime to the expanding-lens regime occurs at a non-dimensional critical time of $\tau_c$. Thus at early and late times, the non-dimensional radial position is given by

$$\xi = \begin{cases} k_1 \tau^{3/4}, & \text{if } \tau \leqslant \tau_c, \\ k_2 \tau^{1/4}, & \text{if } \tau > \tau_c, \end{cases}$$  (3.19)

in which $k_1$, $k_2$ and $\tau_c$ are empirical constants to be determined by the experiments described in the following section.

**Lens thickness**

In the experiments by Griffiths & Linden (1981), and neglecting any mixing between the lens fluid and the ambient fluid, the density, $\rho_{lens}$, of the lens fluid

remains constant both spatially and temporarily, and is equal to the value of the source fluid density. Griffiths & Linden (1981) derived the maximum lens thickness to be $h(t) = \left(\frac{\Omega^2 F_s t}{\pi g_{lens}'^2}\right)^{1/2}$, where $g_{lens}' = g\left(\rho_{lens} - \rho_u\right)/\rho_u$ is constant. In adapting this result to the present study, we first imagine a scenario in which a lens above an interface is fed by the descending plume. As the lens grows due to the continuous discharge of plume fluid, its upper extent slowly approaches the source. As a consequence, the plume falls a progressively smaller vertical distance before entering the lens and so directly entrains less external ambient fluid. Therefore, $\rho_{lens}$, now a function of $t$, steadily grows with time. Defining $h_u(t)$ to be the lens thickness in such scenario, the Griffiths & Linden (1981) result shows that

$$h_u(t) \propto \frac{\Omega F_s^{1/2} t^{1/2}}{g_{lens}'(t)} = \frac{\Omega F_s^{1/2} t^{1/2}}{g'(H_u)} \gamma(t). \tag{3.20}$$

Here we have introduced a variable,

$$\gamma(t) = g'(H_u)/g_{lens}'(t). \tag{3.21}$$

Remarkably, and as we shall explore in greater detail below, (3.20) provides helpful guidance even for the case when the descending plume impinges upon an ambient interface rather than solid bottom boundary. In the ambient interface case, discharged plume fluid is, of course, partitioned between the upper and lower ambient layers according to the magnitudes of $\rho_u$ and $\rho_l$. On the other hand, there also exists in this case the possibility of fountain-head entrainment, which provides another source of lens fluid. The balance of these competing effects is such that (3.20) will be shown to provide a reasonably accurate description of the experimental data. Such information is useful in understanding the dynamics of the lens more generally: given $h_u(t)$ we can estimate the volume of fluid from the plume entering the top of the lens using (3.12). Separately measuring this total volume from the experiments, the difference provides a measure of fountain-head entrainment through (3.13). By extension, we can examine how rotation affects the fountain-head entrainment rate relative to the prediction made for a non-rotating ambient, as given by (3.10).
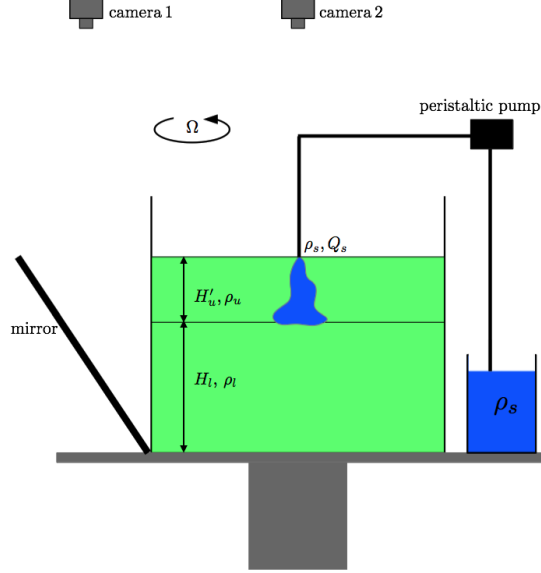
Figure 3.1: Schematic of the experimental apparatus. A tank of a square horizontal cross-section, $50\,\text{cm} \times 50\,\text{cm}$, and depth of $50\,\text{cm}$ is placed on a turntable which rotates at angular frequency $\Omega$. The salt water in the lower layer has a density $\rho_l$ and thickness $H_l$; the upper layer is filled with fresh water of density $\rho_u$. The distance from the nozzle to the interface is $H'_u$. Saline water of density $\rho_s > \rho_l$ flows through the nozzle with a volume flux $Q_s$. Camera 1 is used to record the side view movie through the angled mirror and camera 2 is for top-view recording.

## 3.3 Experimental setup

The experiment setup is shown in figure 3.1. An acrylic square tank having a horizontal cross section of $50\,\text{cm} \times 50\,\text{cm}$ and depth of $50\,\text{cm}$ was placed on a turntable (ANUTECH) for the laboratory experiments. The $1\,\text{m}$ diameter turntable provided a constant rotation at angular frequencies, $\Omega$, from $0.01\,\text{s}^{-1}$ to $10\,\text{s}^{-1}$ with an accuracy of $0.001\,\text{s}^{-1}$. Prior to the initiation of rotation, the tank was filled to a depth of $H_l = 25.0\,\text{cm}$ with saline water having a density of $\rho_l$. Values for $\rho_l$ fell into one of two categories: either $1.00753\,\text{g cm}^{-3} \leqslant \rho_l \leqslant 1.00802\,\text{g cm}^{-3}$ or $1.01735\,\text{g cm}^{-3} \leqslant \rho_l \leqslant 1.02070\,\text{g cm}^{-3}$. Densities were measured with a densitometer (Anton Paar DMA 4500) having a precision of $\pm 0.00001\,\text{g cm}^{-3}$ at a reference temperature of $20\,°\text{C}$. Experiments were performed in a laboratory having a room temperature that fluctuated between $22\,°\text{C}$ and $23\,°\text{C}$, which resulted in measurement uncertainties of $0.0002\,\text{g cm}^{-3}$.

60

A plume nozzle (designed by Dr. Paul Cooper and described in more detail by Hunt & Linden, 2001) was suspended vertically above the lower layer at the radial centre of the tank. The nozzle had a circular opening whose diameter measured $0.4\,\text{cm}$. The vertical distance between the nozzle opening and the lower layer free surface was defined as the upper layer thickness $H_u'$ where $3.0\,\text{cm} \leq H_u' \leq 8.0\,\text{cm}$. The effective upper layer thickness is taken to be $H_u = H_u' + z_v$, in which $z_v$ is the virtual origin, which accounts for the fact that the nozzle has a finite area and the plume has a finite source volume flux, $Q_s$ (Hunt & Kaye, 2001). A small piece of mesh was affixed to the nozzle opening so as induce small-scale fluctuations within the plume, which was observed to become turbulent close to the source.

The tank was then put into solid-body rotation allowing 30 minutes to elapse after the initiation of rotation. An upper layer of density $\rho_u = 0.99850\,\text{g cm}^{-3}$ was then added through a sponge float over top of the lower layer until the free surface was approximately $0.5\,\text{cm}$ above the nozzle opening. Any air bubbles at the nozzle source were manually removed.

The system rotated for another hour to ensure a state of solid-body rotation. The plume was generated using a peristaltic pump (Manostat Carter) to force saline water of density $1.06685\,\text{g cm}^{-3} \leqslant \rho_s \leqslant 1.07212\,\text{g cm}^{-3}$ through the nozzle at a volume flux $Q_s$ ranging from $0.1\,\text{cm}^3\,\text{s}^{-1}$ to $1.1\,\text{cm}^3\,\text{s}^{-1}$. This fluid was drawn from a $8\,\text{L}$ source reservoir, which was located just beneath the tank and which rotated with the same angular frequency. Before the start of each experiment the volume flux was calibrated by measuring the volume of fluid discharged by the nozzle into a graduated cylinder over a time interval of $150\,\text{s}$.

Two cameras secured to the frame of the rotating table were used to record movies of the experiments. Side-view movies were obtained with a digital camera set in movie mode (Canon EOS REBEL T2i), which was directed downwards to an angled flat mirror so that light reaching the camera passed parallel to the ambient interface. Top-view movies were obtained with a digital movie camera (Panasonic HDC-HS250) directed downwards along the axis of rotation at a

vertical distance of 2 m above the base of the tank. An electroluminescent light sheet was placed under the tank. On the opposite side from the angled mirror across the tank was situated a light stand with four horizontally stacked fluorescent bulbs. A piece of tracing paper was fastened to the tank wall adjacent to the fluorescent bulbs to diffuse the intense light so produced. After each experiment the movies were loaded into Matlab for further analysis, as described in the next section. In total, 36 experiments were performed with parameters listed in table 3.1.

## 3.4 Experiment analyses and results

### 3.4.1 Analysis methods and qualitative results

An experiment begins once the peristaltic pump supplies fluid to the nozzle and a descending plume is formed. The point in time when the plume first reaches the ambient interface is regarded as $t = 0$. Figure 3.2 shows the general features from a typical experiment; here $\Omega = 0.2\,\mathrm{s}^{-1}$, $\rho_l = 1.00776\,\mathrm{g\ cm}^{-3}$, $\rho_s = 1.06674\,\mathrm{g\ cm}^{-3}$, $Q_s = 1.02\,\mathrm{cm}^3\,\mathrm{s}^{-1}$, and $H_u' = 5.3\,\mathrm{cm}$. The virtual origin for this experiment is calculated to be $z_v = 0.96\,\mathrm{cm}$ (Hunt & Kaye, 2001). Accordingly, we define the effective upper layer thickness as $H_u = H_u' + z_v = 6.26\,\mathrm{cm}$ with the origin of the coordinate system coincident with the virtual source. Even though $\rho_s > \rho_l$, the density of the plume, $\rho$, decreases during its descent through the upper layer due to entrainment of upper layer fluid, so that $\rho(H_u) < \rho_l$ and hence discharged plume fluid accumulates along the interface. More specifically, this discharged fluid forms a radially spreading interfacial gravity current that in turn evolves into an anticyclonically rotating lens having a relatively slow rate of expansion (see figure 3.2 (a)). As time progresses the plume entrains the relatively more dense fluid in the lens until its density at the interface becomes larger than that of the lower layer. Thereafter, discharged plume fluid falls to depth (figure 3.2 (b)). A vertical time series constructed from movie slices taken below the nozzle is used to estimate the time, $T_p$, when penetration

62

| Expt. | $\Omega$ | $\rho_l$ | $\rho_s$ | $Q_s$ | $H_u$ | $\Lambda$ | $\mathrm{Fr}_i$ | $\mathrm{Ro}(H_u)$ | $T_p$ |
|---|---|---|---|---|---|---|---|---|---|
| | $\mathrm{s}^{-1}$ | $\mathrm{g\ cm}^{-3}$ | $\mathrm{g\ cm}^{-3}$ | $\mathrm{cm}^3\ \mathrm{s}^{-1}$ | cm | | | | s |
| 1 | 0 | 1.00778 | 1.06931 | 1.01 | 4.24 | 0.925 | 4.83 | $\infty$ | 250 |
| 2 | 0 | 1.00775 | 1.06923 | 0.88 | 5.17 | 0.609 | 3.92 | $\infty$ | – |
| 3 | 0 | 1.00788 | 1.06690 | 0.96 | 6.22 | 0.457 | 3.40 | $\infty$ | – |
| 4 | 0.05 | 1.00760 | 1.07050 | 0.87 | 4.36 | 0.826 | 4.57 | 66.1 | 60 |
| 5 | 0.05 | 1.00775 | 1.07055 | 0.94 | 5.30 | 0.618 | 3.95 | 52.3 | 118 |
| 6 | 0.1 | 1.00754 | 1.06995 | 0.94 | 4.20 | 0.926 | 4.84 | 35.5 | 33 |
| 7 | 0.1 | 1.00776 | 1.06921 | 0.89 | 5.18 | 0.612 | 3.93 | 26.3 | 99 |
| 8 | 0.1 | 1.00775 | 1.07043 | 0.92 | 5.19 | 0.631 | 3.99 | 26.7 | 75 |
| 9 | 0.1 | 1.00774 | 1.06864 | 0.92 | 6.19 | 0.462 | 3.42 | 20.9 | 127 |
| 10 | 0.1 | 1.00770 | 1.06953 | 0.98 | 8.22 | 0.304 | 2.77 | 14.7 | – |
| 11 | 0.2 | 1.00791 | 1.07055 | 0.81 | 4.12 | 0.835 | 4.59 | 17.4 | 27 |
| 12 | 0.2 | 1.00753 | 1.06653 | 0.97 | 5.23 | 0.636 | 4.01 | 13.2 | 54 |
| 13 | 0.2 | 1.00776 | 1.06674 | 1.02 | 6.26 | 0.476 | 3.47 | 10.6 | 82 |
| 14 | 0.2 | 1.00787 | 1.06927 | 0.95 | 7.21 | 0.364 | 3.03 | 8.6 | 232 |
| 15 | 0.2 | 1.00798 | 1.06780 | 0.60 | 7.01 | 0.273 | 2.63 | 7.7 | – |
| 16 | 0.3 | 1.00774 | 1.07041 | 0.87 | 4.26 | 0.845 | 4.62 | 11.4 | 17 |
| 17 | 0.3 | 1.00776 | 1.06917 | 0.90 | 5.18 | 0.615 | 3.94 | 8.8 | 39 |
| 18 | 0.3 | 1.00783 | 1.06912 | 0.91 | 6.19 | 0.457 | 3.40 | 7.0 | 90 |
| 19 | 0.3 | 1.00785 | 1.06712 | 1.10 | 7.30 | 0.385 | 3.12 | 5.9 | 133 |
| 20 | 0.3 | 1.02070 | 1.07195 | 0.98 | 5.22 | 0.276 | 2.64 | 9.1 | 190 |
| 21 | 0.3 | 1.00783 | 1.06782 | 0.65 | 7.04 | 0.291 | 2.71 | 5.2 | – |
| 22 | 0.4 | 1.00787 | 1.06965 | 0.90 | 4.28 | 0.839 | 4.60 | 8.5 | 12 |
| 23 | 0.4 | 1.00770 | 1.06967 | 0.89 | 5.17 | 0.619 | 3.95 | 6.6 | 26 |
| 24 | 0.4 | 1.00791 | 1.06701 | 1.02 | 6.26 | 0.470 | 3.45 | 5.3 | 58 |
| 25 | 0.4 | 1.00792 | 1.06939 | 1.04 | 7.26 | 0.380 | 3.10 | 4.4 | 112 |
| 26 | 0.4 | 1.00772 | 1.06891 | 0.93 | 8.20 | 0.293 | 2.72 | 3.6 | 233 |
| 27 | 0.4 | 1.00781 | 1.06685 | 0.10 | 5.62 | 0.121 | 1.75 | 2.8 | – |
| 28 | 0.5 | 1.00784 | 1.06935 | 0.84 | 5.15 | 0.590 | 3.86 | 5.2 | 28 |
| 29 | 0.5 | 1.00773 | 1.06955 | 0.91 | 6.19 | 0.464 | 3.42 | 4.2 | 49 |
| 30 | 0.5 | 1.01735 | 1.07212 | 1.01 | 4.93 | 0.365 | 3.04 | 5.9 | 85 |
| 31 | 0.5 | 1.00785 | 1.06950 | 0.90 | 7.18 | 0.355 | 2.99 | 3.4 | 87 |
| 32 | 0.5 | 1.00770 | 1.06955 | 0.88 | 7.17 | 0.356 | 3.00 | 3.4 | 90 |
| 33 | 0.5 | 1.00775 | 1.07008 | 0.93 | 8.19 | 0.295 | 2.73 | 2.9 | 157 |
| 34 | 0.5 | 1.01989 | 1.07194 | 0.88 | 4.96 | 0.290 | 2.71 | 5.6 | 116 |
| 35 | 0.5 | 1.00802 | 1.06872 | 0.95 | 8.21 | 0.287 | 2.69 | 2.9 | 131 |
| 36 | 0.5 | 1.00773 | 1.07030 | 0.93 | 9.19 | 0.245 | 2.49 | 2.5 | 308 |

Table 3.1: Experimental parameters. Variables are defined as $\Omega$: angular frequency; $\rho_l$: lower layer density; $\rho_s$: plume source density; $Q_s$: plume source volume flux; $H_u$: effective upper layer thickness; $T_p$: penetration time; $\Lambda$: buoyancy parameter defined by (3.5); $\mathrm{Fr}_i$: interfacial Froude number; $\mathrm{Ro}(H_u)$: plume interfacial Rossby number. In some experiments, the penetration of discharged plume fluid into the lower layer is not observed in a duration of 310 seconds, in which case $T_p$ is then indicated as –.

(a) Side view, $t = 40\,\mathrm{s}$

(b) Side view, $t = 100\,\mathrm{s}$

$h_u^* = 1.8\,\mathrm{cm}$

$D_{lens}(z, t)$

(c) Vertical time series at $x = 0$

$T_p = 77\,\mathrm{s}$
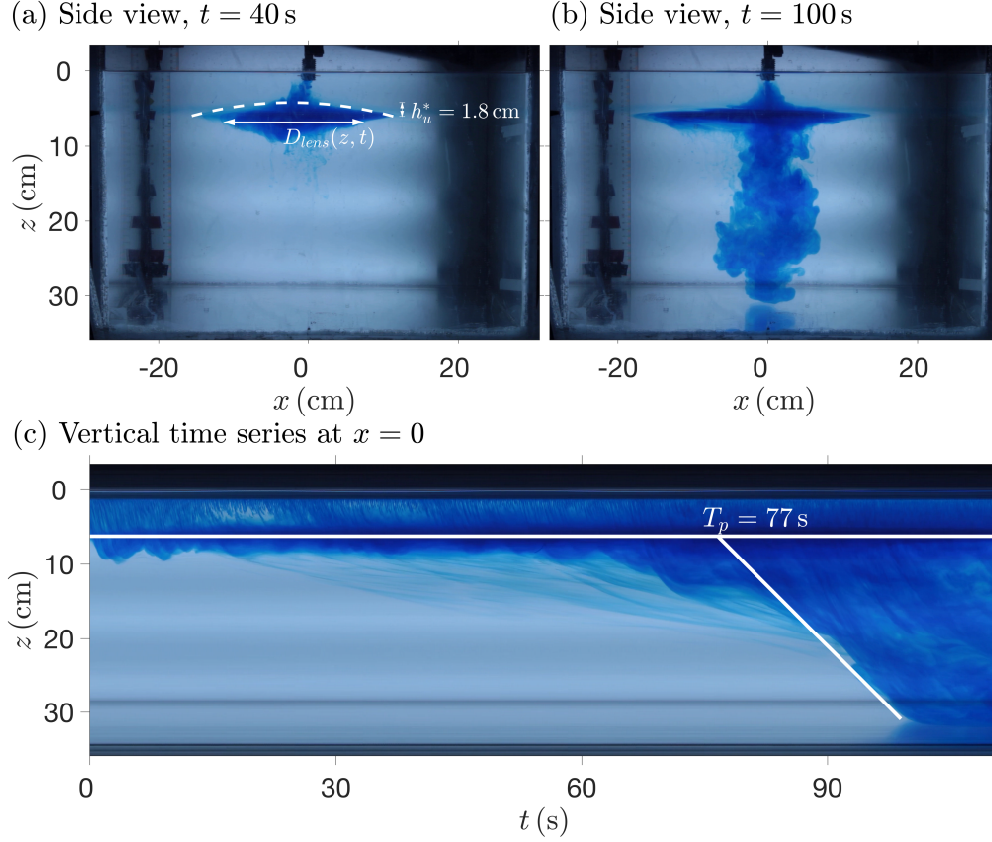
Figure 3.2: Two snapshots from the side-view movie of Experiment 13 (see table 3.1). (a) $t = 40\,\mathrm{s}$: discharged plume fluid spreads radially at the interface and the maximum thickness of the upper part of the lens measures $h_u^* = 1.8\,\mathrm{cm}$. The distance between the left and right front positions of the lens at depth $z$ defines depth-dependent lens diameter, $D_{lens}(z, t)$. (b) $t = 100\,\mathrm{s}$ after fluid has penetrated through the ambient interface. (c) Vertical time series constructed below the location of the nozzle, at $x = 0$. The interface level, $z = 6.26\,\mathrm{cm}$ is marked with the horizontal white line. The evolution of the plume that falls through the lower ambient layer is determined by fitting a contour-matching straight line over the height range $15\,\mathrm{cm} \leq z \leq 30\,\mathrm{cm}$. The onset of penetration, $T_p = 77\,\mathrm{s}$, is determined as the intersection point between the sloping and horizontal white lines.

64

(a) Side view, $t = 20\,\mathrm{s}$

(b) Side view, $t = 40\,\mathrm{s}$

(c) HTS at $z = 3.5\,\mathrm{cm}$
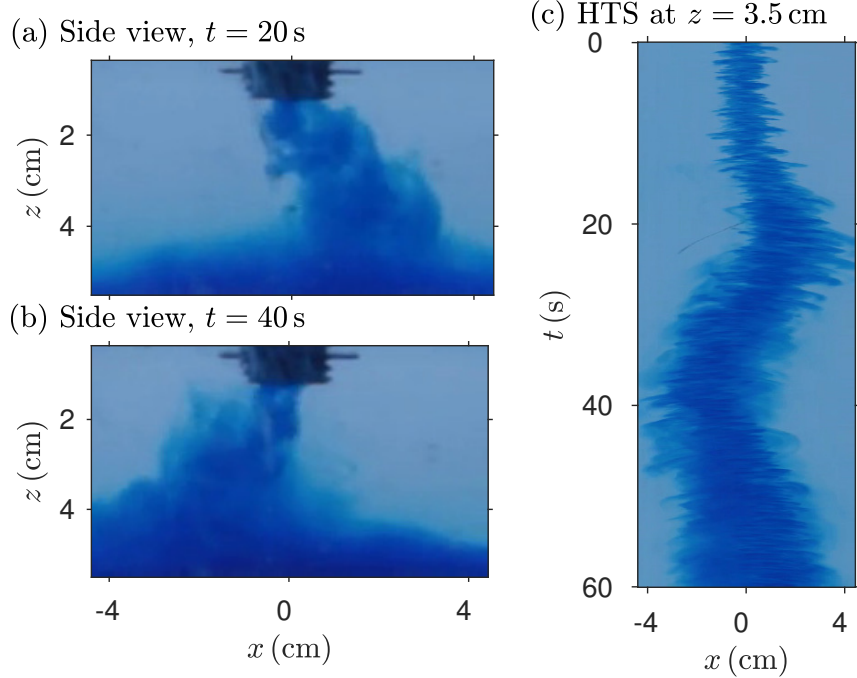
Figure 3.3: Zoomed-in snapshots of the region close to the nozzle from the side-view movie of the experiment shown in figure 3.2. The plume is deflected to the right at (a) $t = 20\,\mathrm{s}$, and to the left at (b) $t = 40\,\mathrm{s}$. A horizontal time series (HTS) constructed from the movie at $z = 3.5\,\mathrm{cm}$ is shown in panel (c).

through the interface first occurs (figure 3.2 (c)). This is found by fitting a line to the descending front of the plume in the lower layer and extrapolating back to the level of the ambient interface. Fitting using a straight line is justified here because we find that, immediately post-penetration, discharged plume fluid falls at a nearly constant speed to the bottom of the tank. This is indicated by the inclined solid line in figure 3.2 (c). For the experiment illustrated in figure 3.2, we estimate a penetration time of $T_p = 77\,\mathrm{s}$; data corresponding to other experiments, including those for which penetration was not observed, are summarized in Table 3.1 and are discussed further below.

In most experiments, the plume near the source begins to precess soon after the start of the experiment. Figures 3.3 (a-b) show zoomed-in snapshots focusing on the region around the nozzle from the same experiment shown in figure 3.2. The plume deflects to the right side of the image at $t = 20\,\mathrm{s}$ and to the left side at $t = 40\,\mathrm{s}$. To make this oscillatory behaviour more evident, horizontal time

65

series are constructed from the experimental movie at $z = 3.5\,\mathrm{cm}$ as shown in figure 3.3 (c). The precession period is measured to be approximately $40\,\mathrm{s}$ in this particular case, corresponding to a precession frequency of $0.16\,\mathrm{s}^{-1}$.

In spite of the precession described above, it is clear from figures 3.2 (a-b) that the lens of Experiment 13 remained below the plume up to and beyond the point of penetration of plume fluid into the lower layer. However in some experiments, the lens shifted its position off centre. Such behaviour is noted, for instance, in figure 3.4, which presents snapshots from both side- and top-view movies for Experiment 21. At early times, this experiment is similar to that shown in figure 3.2 (a) before penetration: discharged plume fluid collected below the nozzle and rotated anticyclonically. However, the lens shifted off-centre in a manner similar to that found by Fernando *et al.* (1998) in their experiments with a uniform density ambient. There as here, this azimuthal instability occurred after the lens exceeded a critical radius. Consequently, the plume fluid passed through only a thin part of the lens and so penetration into the lower layer was not observed in a duration of 310 seconds, whereas in comparable experiments with no instability, penetration was observed within this time.

From top-view images such as those exhibited in figure 3.4 (b,d), the radius of the intrusion can be measured as a function of time. For each frame from the top-view movie, the plan area, $S(t)$, of the intrusion is calculated, from which the effective radius of the intrusion is obtained to be $\sqrt{\frac{S(t)}{\pi}}$. The radial distance between $\sqrt{\frac{S(t)}{\pi}}$ and the plume radius at the interface, $b(H_u)$, is given by

$$R^*(t) = \sqrt{\frac{S(t)}{\pi}} - b(H_u), \qquad (3.22)$$

where $*$ indicates a value obtained by experimental measurement. At early times $R^*(t)$ measures the distance of radial advance of the intrusive gravity current and at late times it approximates the radius of the expanding lens.

The maximum thickness of the lens above the interface, $h_u^*(t)$, is measured from side-view movies. Because the plume obstructs the upper part of the lens

(a) Side view, $t = 60\,\text{s}$      (c) Side view, $t = 240\,\text{s}$

(b) Top view, $t = 60\,\text{s}$      (d) Top view, $t = 240\,\text{s}$
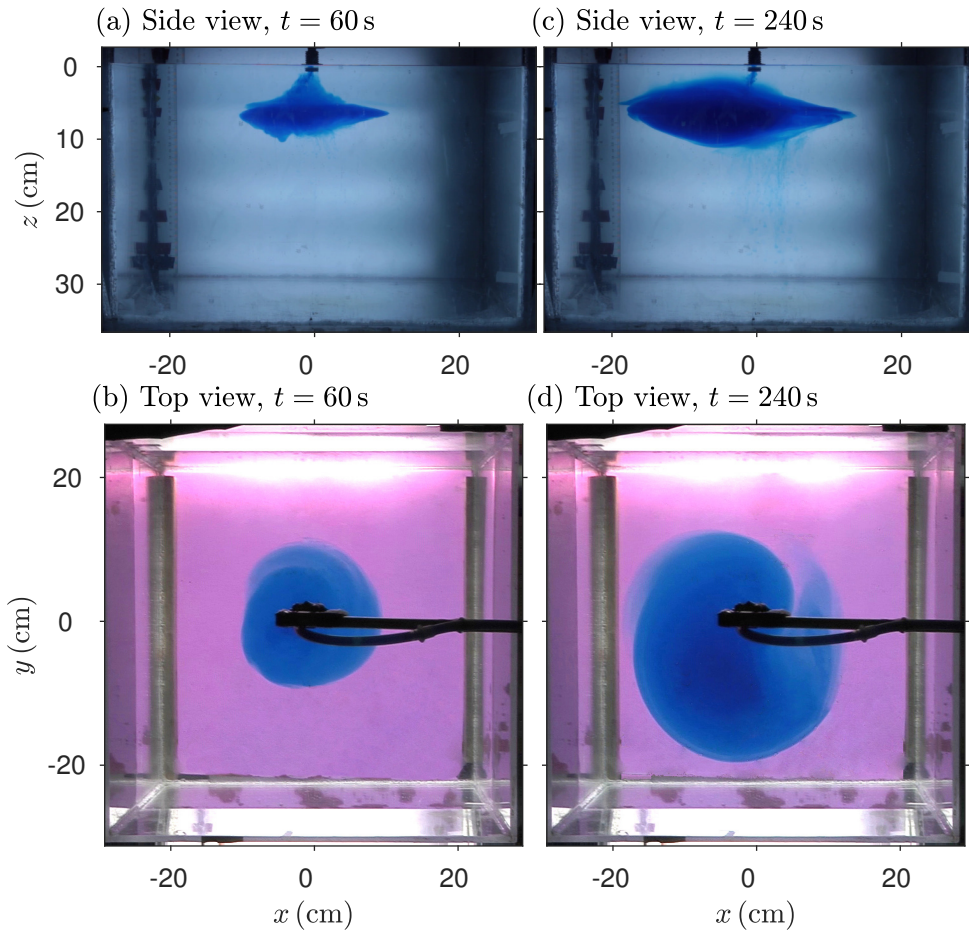
Figure 3.4: Snapshots from both side-view and top-view movies of Experiment 21 in table 3.1. The other horizontal axis in the top-view images is indicated as $y$ with origin located at the nozzle. Here, an instability causes the lens to move off-centre between $t = 60\,\text{s}$ and $t = 240\,\text{s}$. Consequently, no penetration is observed. A metal rod is used to suspend the nozzle above the tank; it appears, (along with the tubing supplying the nozzle) as a horizontal line in panels (b) and (d).

at its centre, it is difficult to measure $h_u^*(t)$ directly in all cases. Instead, we fit the left and right upper halves of the lens boundary using a second-order polynomial function as illustrated in figure 3.2 (a). The vertical growth of the lens is faster in experiments having larger $\Omega$, these being the cases where the radial outflow of discharged plume fluid is inhibited by the Coriolis force.

Given $h_u^*(t)$, the volume of the lens, $V_{lens}(t)$, can be estimated from

$$V_{lens}(t) = \frac{\pi}{4} \int_{H_u-h_u^*(t)}^{z_{max}(t)} D_{lens}^2(z,t)\mathrm{d}z, \tag{3.23}$$

at least up until $t = T_p$ or until the point in time when the lens becomes unstable and drifts away from the axis of rotation. Here, $z_{max}(t)$ is the maximum vertical distance of the lens from the origin and $D_{lens}(z,t)$ indicates the depth-dependent diameter measured from side-view images of the experiment, as shown in figure 3.2 (a). Because the ambient fluid in the upper and lower layers have different densities and therefore different refractive indices, images are expected to be distorted in the immediate neighbourhood of the ambient interface, which introduces errors in calculating $V_{lens}$. To correct for this effect, we analyzed images of the tank with no descending plume but with density of lower layer ambient fluid to be $\rho_l = 1.00800\,\mathrm{g\ cm^{-3}}$ or $\rho_l = 1.02000\,\mathrm{g\ cm^{-3}}$ and fresh water in the upper layer. Based on the apparent distortion of a vertically-aligned ruler placed inside of the tank, a refraction correction scheme was devised that was then applied to all the other experimental images collected during this study.

### 3.4.2   Quantitative results

Figure 3.5 shows a plot of the frequency of precession $\omega$ versus the background rotation frequency $\Omega$. In their study of plumes in a rotating uniform density ambient fluid, Frank *et al.* (2017) found that $\omega$ increases linearly with $\Omega$ with a proportionality constant of $0.40 \pm 0.04$. Likewise we find an approximately linear relationship between $\omega$ and $\Omega$, although with a moderately larger slope of $0.52 \pm 0.09$.

In figure 3.6 (a), the non-dimensional radial position of the intrusion front,
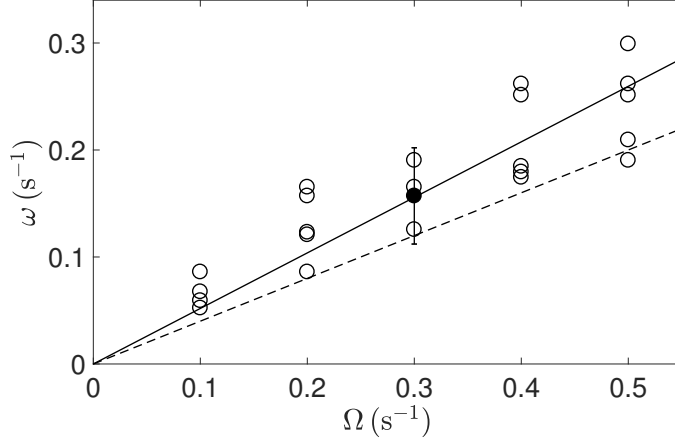
Figure 3.5: Frequency of the plume precession, $\omega$, plotted against the background rotation rate, $\Omega$. A representative error bar is plotted on the closed symbol. The best-fit line is indicated as the solid line and the dashed line is the result by Frank *et al.* (2017).

$\xi$, is plotted against non-dimensional time, $\tau$. Consistent with our prediction (3.19), we find a rapid increase at early times followed by a slower advance at later times. With (3.19) in mind, we fit the measured data from figure 3.6 (a) to the form $\xi = k_1 \tau^{3/4}$ for $\tau < 5$ and to $\xi = k_2 \tau^{1/4}$ for $\tau > 20$. Doing so gives proportionality constants $k_1 = 0.25 \pm 0.04$ and $k_2 = 0.63 \pm 0.04$. The critical time, $\tau_c \approx 2\pi$, is found as the intersection point between the dashed and solid lines in figure 3.6 (a). Thus we compose the following semi-empirical prediction for the (dimensional) front position as a function of time:

$$R(t) = \begin{cases} [0.25 \pm 0.04] \left(F_s t^3\right)^{1/4}, & t \lesssim 2\pi/\Omega, \\ [0.63 \pm 0.04] \left(\frac{F_s t}{\Omega^2}\right)^{1/4}, & t \gtrsim 2\pi/\Omega. \end{cases} \qquad (3.24)$$

In figure 3.6 (b), the predictions of (3.24) are compared against analogue measured data for a variety of experiments with generally favourable agreement observed.

Figure 3.7 shows how the penetration time, $T_p$, depends on $\Omega$ and $\Lambda$, given by (3.5). The value of the penetration time, $T_p$, is proportional to the size of the circles. In all these experiments, the lens remained centred under the plume. Square symbols indicate those cases having an unstable lens for which penetration does not occur by the end of the (310 s duration) experiment. It is
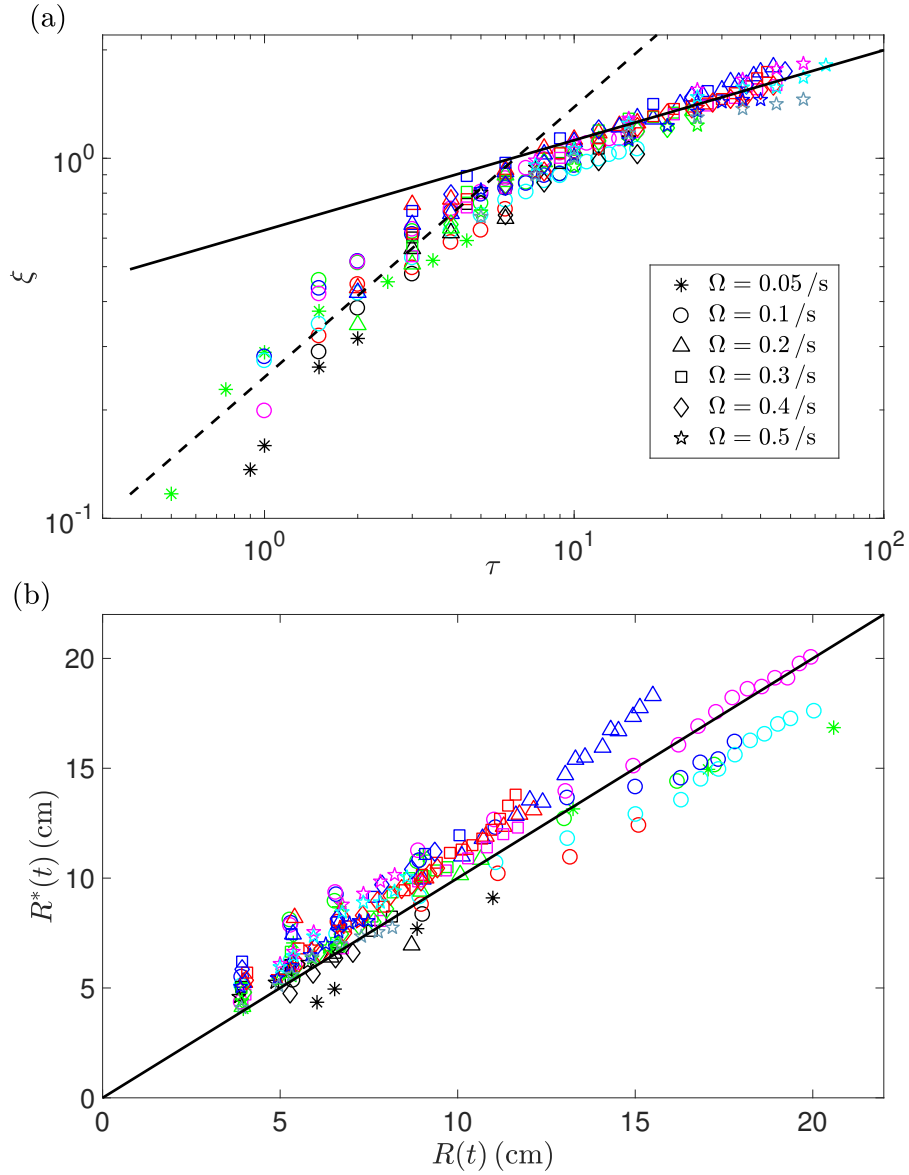
69

Figure 3.6: (a) The non-dimensional radial position of the intrusion front, $\xi$, vs. non-dimensional time, $\tau$. The best-fit line for $\tau < 5$ ($\tau > 20$) is given by the dashed (solid) line. The intersection between these two lines is found to be $\tau_c \approx 2\pi$. (b) The dimensional radial position of the intrusion front, $R^*(t)$, measured from different experiments vs. $R(t)$ from (3.24). Different experiments with the same value of $\Omega$ are distinguished by the different colours and provide an indication of the reproducibility of our experiments.
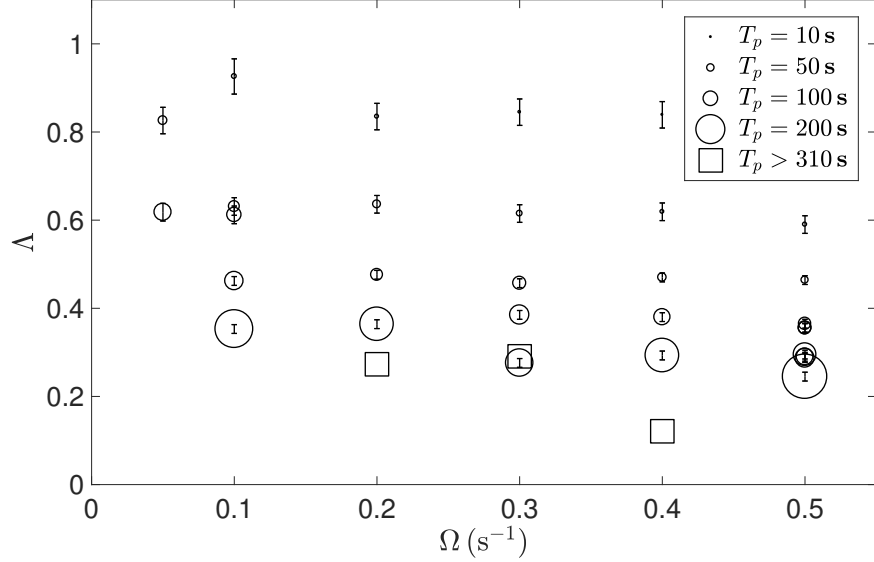
Figure 3.7: The penetration time, $T_p$, plotted as a function of $\Lambda$ and $\Omega$. The symbols $\square$ designate experiments for which no penetration was observed before the end of the experiment.

observed that $T_p$ generally increases as $\Lambda$ decreases: it takes more time for the plume to increase its density at the interface to the point of penetration if the initial density of the plume at the interface is much less than the density of the lower layer. Also, and although there is some scatter in the data, $T_p$ decreases as $\Omega$ increases. This is because the lens radius decreases with increasing $\Omega$, and, consequently the thickness of the lens increases. Thus the plume re-entrains the comparatively larger density fluid of the lens over a greater depth making its density at the interface larger. On the other hand, as discussed further below, rotation indirectly reduces the volume of fluid entrained from the lower layer through the fountain-head. The reduced volume of more dense entrained fluid slows the increasing density of the lens and so retards the time of onset of penetration.

Expanding on the data of figure 3.7, the non-dimensional penetration time $\tau_p = \Omega T_p$ is plotted against $\Lambda$ in figure 3.8. The measured data from different experiments collapses well. The inset figure shows $\ln(\tau_p)$ versus $\ln(\Lambda)$ from which we find the following trend based on the line of best fit:

$$\tau_p \equiv T_p \Omega = (2.7 \pm 0.5)\, \Lambda^{-2.7 \pm 0.2}. \tag{3.25}$$

71
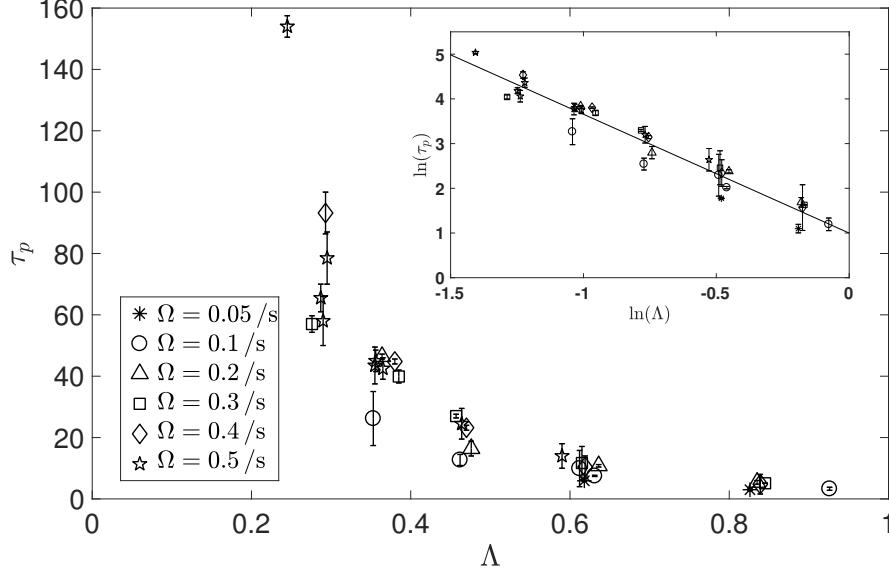
Figure 3.8: Non-dimensional penetration time, $\tau_p$, vs. $\Lambda$. The inset shows $\ln(\tau_p)$ vs. $\ln(\Lambda)$, and the solid line is a best-fit of the measurements, which is given by $\tau_p = (2.7 \pm 0.5)\,\Lambda^{-2.7 \pm 0.2}$.

In comparison, the characteristic time-scale employed by Mott & Woods (2009) to normalize the penetration time from their non-rotating experiments was a buoyancy time, which was a function of the horizontal cross-sectional area of the tank. In our experiments with rotation the lens never reaches the side walls of the tank. It is thus reasonable to take $1/\Omega$ as the characteristic time in (3.25). This power law does not correctly predict the behaviour in the immediate-penetration limiting case $\Lambda \to 1$, for which $\tau_p \to 0$ is expected. However, it is remarkable that it holds up to values of $\Lambda \approx 0.9$ for values of $\tau_p$ as low as about 3.

As discussed in §3.2.2, a number of assumptions are made to infer the scaling relationship for $h_u(t)$. For example, we assume that the lens has a spatially-uniform reduced gravity of $g'_{lens}(t)$ that increases with time. Meanwhile, $g'_{lens}(T_p)$ is assumed to be identical to $g'_{ul}$, which ignores the possible contribution of the plume momentum to the penetration process. In the context of (3.5) and (3.21), this latter assumption requires that

$$\gamma(T_p) = \Lambda. \tag{3.26}$$
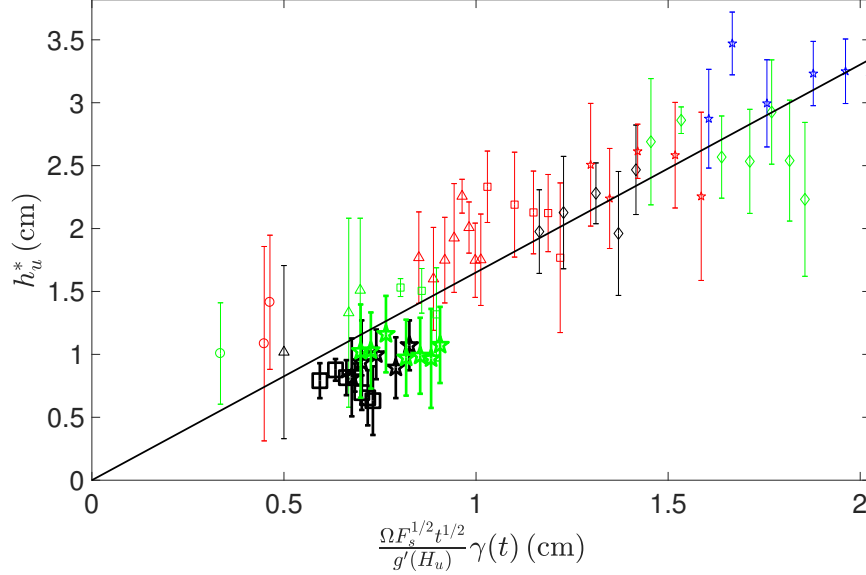
Figure 3.9: Measured thicknesses of the lens above the interface, $h_u^*(t)$, vs. $\frac{\Omega F_s^{1/2} t^{1/2}}{g'(H_u)} \gamma(t)$, where $\gamma(t)$ is obtained from (3.28). A best-fit line having slope 1.6 is as indicated. As with figure 3.6, different symbols represent different rotation rates and different colours indicate different experiments. The thick symbols show Experiments 20, 30 and 34 for which $\rho_l \approx 1.02\,\mathrm{g\,cm^{-3}}$; in all other cases, $\rho_l \approx 1.008\,\mathrm{g\,cm^{-3}}$ (see table 3.1).

Substituting (3.26) into (3.25) yields

$$\gamma(T_p) = (1.4 \pm 0.1)\,(\Omega T_p)^{-0.37 \pm 0.03}\,, \tag{3.27}$$

as a measure of the relative plume-to-lens density at the penetration time. Generally, according to (3.21), $\gamma(t)$ is function of time up to $t = T_p$. Thus we assert that the relative lens density in any single experiment evolves in time according to

$$\gamma(t) = (1.4 \pm 0.1)\,(\Omega t)^{-0.37 \pm 0.03}\,,\ t \lesssim T_p. \tag{3.28}$$

The lower layer density, $\rho_l$, does not enter explicitly into the power law, but is important because it sets the value of $T_p$ implicitly through (3.26).

Substituting the expression for $\gamma(t)$ obtained from (3.28) into (3.20), allows us to plot $h_u^*(t)$ against $\frac{\Omega F_s^{1/2} t^{1/2}}{g'(H_u)} \gamma(t)$, as shown in figure 3.9. The data points from experiments with large lower layer density, $\rho_l \approx 1.02\,\mathrm{g\,cm^{-3}}$, lie moderately below the trend from other experimental data with smaller $\rho_l$, suggesting that $\rho_l$ may implicitly, if only modestly, influence the empirical constants in the power

law (3.28). This provides some indication of the importance of fountain-head entrainment. From the slope of the best-fit line indicated in figure 3.9, we surmise that the constant of proportionality implicit in (3.20) is 1.6. Thus a semi-empirical expression for $h_u(t)$ is given by

$$h_u(t) \approx 0.16\Omega^{0.63}F_s^{-1/6}H_u^{5/3}t^{0.13}. \tag{3.29}$$

With this semi-empirical result to hand, $V_p(t)$ can be calculated from (3.12) and $V_{ent}(t)$ can be obtained from (3.11). Thus the average entrainment rate, $\bar{E}_i$ can be calculated from (3.13), at least for the time period before the onset of penetration. In figure 3.10, the ratio of the average fountain-head entrainment rate, $\bar{E}_i$, to the theoretical estimate, $E_i$, obtained by Shrinivas & Hunt (2014) in the absence of rotation is plotted against the inverse of the Rossby number. Here, the Rossby number, Ro, is measured at the level of the ambient interface and at the initial time, $t = 0$. The ratio of entrainment values clearly decreases as $\text{Ro}^{-1}(H_u)$ increases, which is consistent with the explanation provided in §3.2.1. Fitting a best-fit curve to the data of figure 3.10, we find a functional relationship given by

$$\frac{\bar{E}_i}{E_i} = \exp\left((-5.7 \pm 1.7)\,\text{Ro}^{-1}(H_u)\right). \tag{3.30}$$

## 3.5   Discussion and conclusions

We investigated a point-source plume descending into a rotating two-layer ambient fluid. Although the fluid emanating from the source is more dense than the lower layer, turbulent entrainment causes the plume to be less dense than the lower layer when it impinges initially upon the interface. Symbolically, this condition is expressed as $\Lambda \equiv g'(H_u)/g'_{ul} < 1$. As such, our study is similar to those of Kumagai (1984) and Mott & Woods (2009) except that we include background rotation, which non-trivially changes the evolution of the flow in several ways.
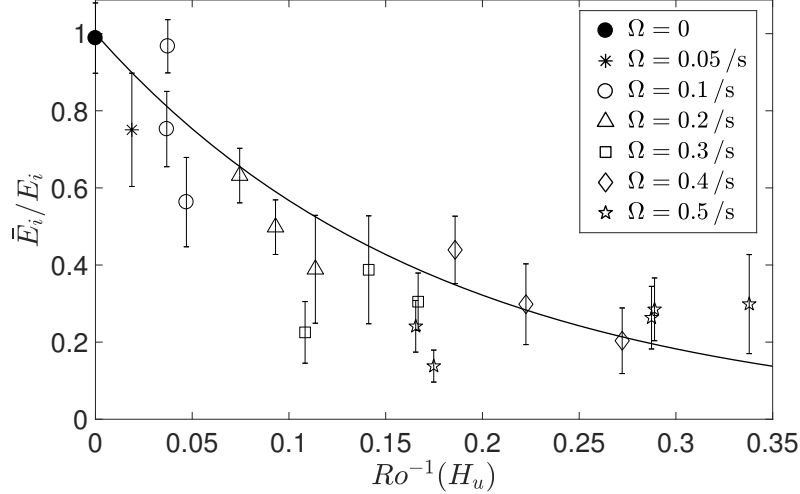
Figure 3.10: Measured fountain-head entrainment rate, $\bar{E}_i$, normalized by the theoretical value in a non-rotating ambient vs. $Ro^{-1}(H_u)$.

As regards the plume dynamics, rotation deflects the radially-inward flows associated with ambient entrainment into the plume resulting in a cyclonic circulation around the plume (Fernando *et al.*, 1998). As in Frank *et al.* (2017), we likewise find that rotation causes the plume to precess anticyclonically. Rotation also modifies the outflow of discharged plume fluid at the ambient interface. This is especially true after approximately one rotation period by which point the outflow is deflected to form an anticyclonic lens which, as argued by Griffiths & Linden (1981), is balanced by buoyancy, centrifugal and Coriolis forces. At these later times, the lens expands radially as $t^{1/4}$.

In our experiments, rotation does not affect the fountain-head entrainment directly because the plume Rossby number measured at the ambient interface is greater than unity. However, rotation suppresses the radial spreading of discharged plume fluid as a result of which the area of contact between the plume head and the lower ambient layer is comparatively small. This has the effect of reducing the volume of lower layer fluid entrained into the lens. Supporting this assertion, figure 3.10 shows that the ratio of the average fountain-head entrainment rate with rotation, $\bar{E}_i$, to the fountain-head entrainment rate without rotation, $E_i$, is a decreasing function of the inverse Rossby number, $Ro^{-1}(H_u)$.

The plume entrains fluid not only from the upper and lower ambient layers,

but also re-entrains fluid previously discharged into the lens. As a consequence of this behaviour, the lens density steadily increases with time up until the point where it exceeds the lower layer density. This defines the onset of penetration which is characterized by discharged plume fluid falling to the bottom of the tank. Thicker lenses which occur for larger $\Omega$, have more voluminous plume re-entrainment and consequently smaller $T_p$, the time corresponding to the onset of penetration. This effect dominates over the retarding effect of reduced fountain-head entrainment, and is captured by the empirical relationship (3.25) for $T_p$ as it depends on rotation through $\Omega$ and the relative initial buoyancy at the interface through $\Lambda$.

# Chapter 4

# LES simulation of turbulent plumes in rotating ambient fluid

## 4.1 Introduction

Many studies about plumes have been carried out theoretically (Morton *et al.*, 1956; Morton, 1959; Hunt & Kaye, 2001; Carlotti & Hunt, 2017) and experimentally either without background rotation (George *et al.*, 1977; Ramaprian & Chandrasekhara, 1989; Dai *et al.*, 1994; Mott & Woods, 2009; Ma *et al.*, 2017) or with background rotation (Fernando *et al.*, 1998; Frank *et al.*, 2017). Investigating plumes by way of numerical simulation is a further option that has advantages over laboratory experiments. Unlike measuring the plume quantities at discrete locations with probes or taking photos from side views, numerical simulations can give fully 3D information, such as the instantaneous velocity and reduced gravity at every location, whether inside the plume proper or within the external ambient. Numerical simulations were adopted by other researchers to investigate turbulent plumes via Direct Numerical Simulation (DNS) (Pham *et al.*, 2007; Plourde *et al.*, 2008; van Reeuwijk *et al.*, 2016) or Large Eddy Simulation (LES) (Zhou *et al.*, 2001; Devenish *et al.*, 2010; Yang *et al.*, 2016*a*; Fabregat Tomàs *et al.*, 2016).

A plume was simulated by van Reeuwijk *et al.* (2016) with DNS in a uniform ambient without background rotation. They found the turbulent plume Prandtl number, $\mathrm{Pr}_t$, defined as the ratio between the eddy viscosity, $\nu_t$, and the eddy

diffusivity, $\kappa_t$, was about 0.7, which was approximately equal to the value for a jet. The comparisons between the simulation results by van Reeuwijk *et al.* (2016) and the MTT model results were good, e.g. when comparing the plume radius or vertical velocity against height. They also computed the entrainment coefficient, $\alpha$, at different heights and found that $\alpha$ values decreased from a very large value close to the plume source to a relatively constant value away from the source. Fabregat Tomàs *et al.* (2016) performed LES simulations to investigate plumes rising in a rotating linearly stratified ambient fluid. In their simulations, an additional term was added in the horizontal momentum equations to account for the Coriolis force. By including background rotation, they found that the plume precessed anticyclonically, which was confirmed by Frank *et al.* (2017) in experiments investigating a descending plume in a rotating uniform ambient.

In this chapter, LES simulations of plumes rising in a non-rotating uniform, rotating uniform and rotating two-layer stratified ambient are presented. In the latter case, simulation parameters are deliberately chosen to be similar to the experimental parameters described in Chapter 3 so that a comparison between laboratory experimental and numerical simulation can be made.

## 4.2 Governing equations

Here we consider both plume and ambient fluids as incompressible. The maximum density difference within the system is small so that the Boussinesq approximation can be applied. For an incompressible fluid, the continuity equation can be approximated as

$$\nabla \cdot \vec{u} = 0, \tag{4.1}$$

where $\vec{u}$ is the velocity. For the sake of modelling a plume with large spatial and long temporal scales (as is relevant to large-scale geophysical flows), the Coriolis force is included in the momentum equation, which is written as follows:

$$\frac{\mathrm{D}\vec{u}}{\mathrm{D}t} = -\frac{1}{\rho_0}\nabla P_T + \frac{\rho}{\rho_0}\vec{g} + \nu\nabla^2\vec{u} - 2\vec{\Omega} \times \vec{u}. \tag{4.2}$$

Here, $\rho$ is the fluid density, $\rho_0$ is a reference density, $P_T$ is the total pressure, $\nu$ is the kinematic viscosity and $\vec{\Omega}$ is the background angular velocity. The fluctuation pressure, $p$, is introduced, which satisfies $-\nabla p = -\nabla P_T + \rho_0 \vec{g}$. Thus (4.2) becomes

$$\frac{\mathrm{D}\vec{u}}{\mathrm{D}t} = -\frac{1}{\rho_0}\nabla p + \vec{g'} + \nu\nabla^2\vec{u} - 2\vec{\Omega} \times \vec{u}, \tag{4.3}$$

where $\vec{g'}$ is the reduced gravity, defined as

$$\vec{g'} = \left(\frac{\rho - \rho_0}{\rho_0}\right)\vec{g}. \tag{4.4}$$

The material derivative, $\frac{\mathrm{D}\vec{u}}{\mathrm{D}t}$, at the left hand side of (4.3) equals the sum of the local time derivative, $\frac{\partial\vec{u}}{\partial t}$, and the advective term, $(\vec{u}\cdot\nabla)\vec{u}$. We suppose that density variations result from temperature variations and that a linear equation of state relates these two quantities, i.e.

$$\rho = \rho_0\left[1 - \beta\left(T - T_0\right)\right], \tag{4.5}$$

where $\beta$ is a constant thermal expansion coefficient and $T_0$ is the reference temperature. In order to achieve laboratory-realistic values for the buoyancy flux, it is necessary in (4.5) to consider elevated values of $T$. We emphasize, however, that our simulations are strictly single phase and that we do not allow for processes like boiling to occur. To close the system, an advection-diffusion equation for $T$ is included, which reads

$$\frac{\mathrm{D}T}{\mathrm{D}t} = \kappa\nabla^2 T, \tag{4.6}$$

where $\kappa$ is the thermal diffusion coefficient. In order to distinguish the plume fluid from the ambient fluid, a non-dimensional passive tracer is associated with the fluid issuing from the plume source. If we assume that this passive tracer, whose concentration is $C$, diffuses at the same rate as $T$, then the corresponding advection-diffusion equation reads

$$\frac{\mathrm{D}C}{\mathrm{D}t} = \kappa\nabla^2 C. \tag{4.7}$$

Consistent with the focus of Chapter 3, our interest is on turbulent plumes having a large Reynolds number, here defined as Re $= \frac{UL}{\nu}$, where $U$ and $L$ are the characteristic values of velocity and flow length scales. Because of the obvious challenges of solving equations (4.1) and (4.3) to (4.7) analytically in the circumstance of turbulent plumes rising in a rotating uniform or two-layer stratified ambient fluid, numerical solutions are instead pursued with an LES method. LES is contrasted with other popular numerical methods, i.e. DNS and Reynolds-Averaged Navier Stokes (RANS) in Appendix C.

## 4.3    MTT model with Gaussian plume

Assuming the horizontal distributions of the time-averaged vertical velocity, $w_G(r, z)$ and reduced gravity, $g'_G(r, z)$, of an axisymmetric plume follow Gaussian profiles, they can be expressed as follows:

$$w_G(r, z) = w_c(z)\exp\left(-\frac{r^2}{b_G(z)^2}\right), \tag{4.8}$$

$$g'_G(r, z) = g'_c(z)\exp\left(-\frac{r^2}{b_G(z)^2}\right), \tag{4.9}$$

where $z$ is the vertical coordinate with the origin located at the ideal plume source and the positive direction downstream of this source, $r$ is the radial coordinate with the origin again located at plume source, $w_c(z)$ and $g'_c(z)$ are the vertical velocity and reduced gravity along the centre-line of the plume, and $b_G(z)$ is the plume radius. From the MTT model, $w_c(z)$, $g_c$ and $b_G(z)$ can be derived as follows (see Appendix B):

$$w_c(z) = \frac{5}{3\alpha}\left(\frac{9\alpha}{10}\right)^{\frac{1}{3}} \pi^{-\frac{1}{3}} F_s^{1/3} z^{-1/3}, \tag{4.10}$$

$$g'_c(z) = \frac{5}{3\alpha}\left(\frac{10}{9\alpha}\right)^{\frac{1}{3}} \pi^{-\frac{2}{3}} F_s^{2/3} z^{-5/3}, \tag{4.11}$$

$$b_G(z) = \frac{6}{5\sqrt{2}}\alpha z. \tag{4.12}$$

Here in order to keep consistent with Chapter 3, we still use the entrainment coefficient, $\alpha$, for a top-hat plume. For the same plume, the entrainment co-

efficient, $\alpha$, assuming a top-hat profile is $\sqrt{2}$ times of that, $\alpha_G$, assuming a Gaussian profile.

From (4.10) and (4.11), the value of $\alpha$ can be expressed as

$$\alpha = \frac{5}{2}\sqrt{\frac{F_s g_c'(z)}{\pi w_c^5(z)}}.$$ (4.13)

Meanwhile dividing $w_c^2(z)$ by $g_c'(z)$ yields

$$z = \frac{2}{3}\frac{w_c^2(z)}{g_c'(z)}.$$ (4.14)

Equation (4.13) can be used to calculate $\alpha$ values from numerical simulation data. In numerical simulations, the vertical coordinate origin, $\tilde{z} = 0$, is usually located in the centre of the bottom boundary of the main computational domain. In order to compare the measurements from numerical simulations with MTT model predictions, i.e. (4.14), we first determine the virtual origin position of the ideal plume that is equivalent, for $\tilde{z} = 0$, to the non-ideal plume in question. This virtual origin is located below the bottom boundary of the main computational domain by a distance $z_v$. Applying (4.14), the relationship between $z_v$ and $\tilde{z}$ can be expressed as follows:

$$z_v = \frac{2}{3}\frac{w_c^2(z)}{g_c'(z)} - \tilde{z}.$$ (4.15)

## 4.4   Simulation setup

Numerical simulations were set up under the framework of OpenFOAM, version 5.0. OpenFOAM is an open-source CFD software based on the C++ language. Like many CFD softwares, a finite volume scheme is adopted in OpenFOAM. Moreover, OpenFOAM provides plentiful pre-built packages to allow users to code various equations in different physical scenarios and for different applications. OpenFOAM is widely used in simulations in industry (Roohi *et al.*, 2013; Chen *et al.*, 2014) and fundamental studies (Lysenko *et al.*, 2012, 2013; Higuera *et al.*, 2018; Zeng *et al.*, 2018). It has also been applied in numerous previous investigations of plumes (Wang *et al.*, 2011; Kumar & Dewan, 2014;
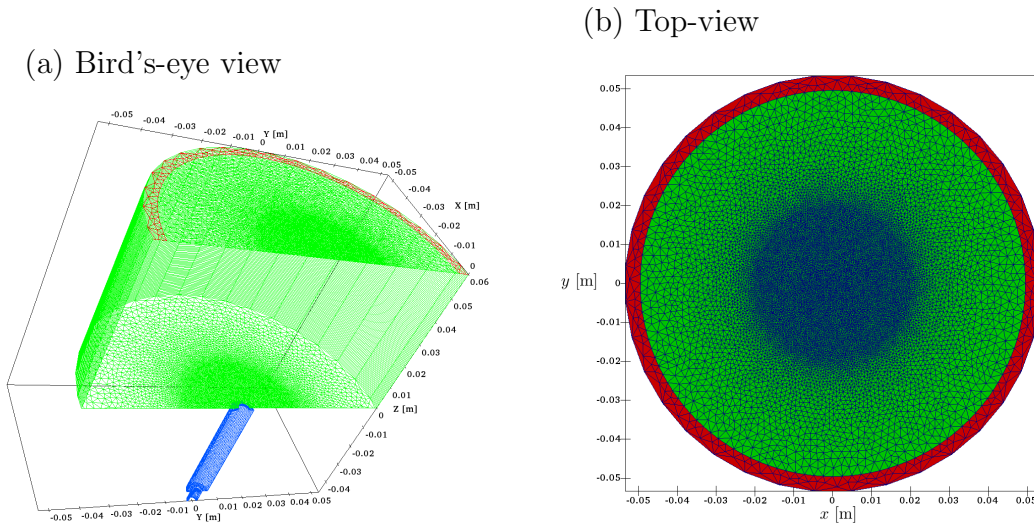
Figure 4.1: Bird's-eye view and top-view of the domain over which numerical simulations are performed. A chamber (shown in blue in panel a) is connected to the computational domain with an opening that is regarded as the plume source. The perimetric area, indicated with red, is the outlet for the domain.

Suzuki *et al.*, 2016). For Boussinesq fluids with heat transfer processes but no background rotation, OpenFOAM provides a pre-built solver, "*buoyantBoussinesqFoam*", for users to use or adapt. Except for the momentum equation, the other equations in *buoyantBoussinesqFoam* are the same as equations (4.1), (4.5) and (4.6). The momentum equation of *buoyantBoussinesqFoam* is similar to (4.2) without including the Coriolis force, $-2\vec{\Omega} \times \vec{u}$. Thus *buoyantBoussinesqFoam* is used to simulate plumes in a non-rotating ambient and adaptions are made based on this package to include the Coriolis term in the momentum equations.

There are also multiple pre-built subgrid-scale (SGS) models within Open-FOAM for one to use. In this chapter, the one-equation eddy-viscosity SGS model (Yoshizawa, 1986), having the name "*kEqn*" within OpenFOAM, is adopted in the LES simulations. The one-equation SGS model solves a transport equation to compute the subgrid scale kinetic energy, and subsequently obtains the subgrid scale eddy viscosity. As addressed by Huang & Li (2009), one-equation SGS models improve LES simulation fidelity by overcoming the shortcomings of

the local equilibrium assumption (Smagorinsky, 1963) in high Reynolds number flows and/or with coarse resolutions.

The mesh was created with Gmsh. One can use Gmsh easily to generate unstructured or structured meshes with relatively complex geometries. The size of the computational domains differ between different simulations. For simulations with uniform ambient fluid, the height of the domain is $H_D = 8\,\mathrm{cm}$ or $6\,\mathrm{cm}$ and the radius, $R_D$, ranges from $2.9\,\mathrm{cm}$ to $5.5\,\mathrm{cm}$. However, because the plume precesses once background rotation is introduced, the domain radius was set to prevent the precessing plume from reaching the side walls. A further consideration applies to the case when the ambient fluid is both rotating and two-layer stratified in that it is advantageous to prevent the intrusions (or lenses) from reaching the side or upper boundaries. In light of the above considerations, the computational domains in simulations including rotation or rotation and stratification were enlarged accordingly. Because the inflow conditions are important for the LES simulation of plumes, a method similar to precursor methods (Tabor & Baba-Ahmadi, 2010) is adopted. Prior to the plume fluid entering the main computational domain through a centred opening of radius $0.2\,\mathrm{cm}$, the fluid flows into a chamber under the inlet opening, as shown in figure 4.1 (a). In the horizontal directions, at the centre region of the main computational domain and throughout the chamber, located below this main computational domain, the meshes had a minimum mean grid spacing of $\Delta x, y = 0.05\,\mathrm{cm}$. This horizontal grid spacing continuously increased to $1\,\mathrm{cm}$ close to the side-wall boundary of the main computational domain, see figure 4.1 (b). By contrast in the vertical direction, we selected a grid spacing of $\Delta z = 0.05\,\mathrm{cm}$ in both the main computational domain and the underlying chamber.

Different types of boundary conditions (BCs) were adopted in different numerical simulations. On the other hand, BCs within the chamber were the same among all simulations. The side boundary of the chamber was set to be a type of "wall" BC, meaning non-slip and non-penetrative. The bottom of

the chamber was set as an inlet BC, whose vertical velocity was specified to be a uniform value upon which was superimposed a 5% random noise. The source fluid flowed through the end of the chamber with a small annular cross-section area into a suddenly wide region. Within the chamber, the flow evolved from laminar to turbulent. Indeed the source Reynolds number, calculated on the basis of the source diameter and vertical velocity, was approximately 6500, more than sufficient to ensure a turbulent flow. The mean volume flux of the fluid across the inlet was set to be $Q_s = 0.817\,\mathrm{cm^3\,s^{-1}}$ for all simulations. Given the radius of the circular opening, an average vertical velocity at the opening was calculated to be $w_s = 6.50\ \mathrm{cm\,s^{-1}}$. Thus the momentum flux was $M_s = w_s Q_s = 5.31\,\mathrm{cm^4\,s^{-2}}$. The density of the fluid is prescribed by the state equation (4.5), with a thermal expansion coefficient, $\beta$, of $2 \times 10^{-4}\,\mathrm{K^{-1}}$, and the reference temperature and density of $T_0 = 293\,\mathrm{K}$ and $\rho_0 = 1\,\mathrm{g\ cm^{-3}}$, respectively. The reference temperature and density were not chosen arbitrarily. Rather they correspond to the temperature and density of the ambient fluid for the case of a homogeneous ambient or to the temperature and density of the lower ambient layer for the case of a two-layer stratified ambient. The source fluid had a temperature of $T_s = 650\,\mathrm{K}$. We reiterate that such a large source temperature was required in order to achieve the requisite source buoyancy flux but that we did not consider boiling in our numerical simulations. (In addition to the boiling point, we also allow the fluid from our simulations to have a different kinematic viscosity from that of water.) Given $T_s$ and according to (4.5), the density of the source fluid was calculated to be $\rho_0 = 0.929\,\mathrm{g\ cm^{-3}}$. The reduced gravity of the source fluid relative to the uniform/lower ambient layer was calculated to be $g'_s = 69.97\,\mathrm{cm\,s^{-2}}$. This is about the same value as in the experiments described in Chapter 3. Therefore, the source buoyancy flux of the plume was obtained to be $F_s = g'_s Q_s = 57.15\,\mathrm{cm^4\,s^{-3}}$.

The bottom boundary of the computational domain was set to be a wall type BC. Because the accuracy of LES simulations was validated by comparing the simulation results with the MTT model results in a non-rotating uniform

| Ambient | floor | side | side, perimeter | upper, centre | upper, perimeter |
|---|---|---|---|---|---|
| Non-rotating, uniform | wall | zero grad. | – | zero grad. | – |
| Rotating, uniform | wall | wall | – | wall | zero grad. |
| Rotating, two-layer | wall | wall | zero grad. | zero grad. | – |

Table 4.1: Simulation boundary conditions (BCs) of the main computational domain. The "wall" indicates non-slip and non-penetrative BC; – indicates that such a boundary does not exist in the simulation.

ambient, in this simulation (see table 4.2 (1)) we mimicked a light plume rising in a infinite ambient fluid by setting the side and entire upper boundaries of the domain as open boundaries, where the flow can freely pass through. Therefore, we set zero gradient boundary conditions on the upper and side boundaries for each of the velocity, temperature and pressure. For simulations involving background rotation but no stratification, fluid was allowed to exit the main computational domain only adjacent to the lateral boundary – see the perimetric region demarcated in red in figures 4.1 (a), (b). Over the rest of the upper boundary, the BC was of wall type. Moreover, for the simulations with a two-layer ambient fluid, the outlet sink was moved to the side boundaries of the computational domain below the ambient interface in order to keep the volume of upper layer fluid constant. A summary of the BCs employed for these different simulations is presented in table 4.1.

For the simulations with two-layer ambient stratification, the stratification is set up by specifying different temperatures in the upper and lower layers. As mentioned above, the lower layer, whose thickness was $H_l$, always had a temperature of 293 K. The temperature of the fluid in the upper layer was set as $T_u$, and thus the density of the fluid in the upper layer was approximately $\rho_0 = 0.984 \, \text{g cm}^{-3}$.

The kinematic viscosity, $\nu$, was given a value of $4 \times 10^{-4} \, \text{cm}^2 \, \text{s}^{-1}$ and the diffusivity, $\kappa$, for temperature and the passive tracer were each defined by $\nu \text{Pr}$. The laminar Prandtl number, Pr, was set to be 7 and the turbulent Prandtl number, $\text{Pr}_t$, was chosen to be 0.7 consistent with van Reeuwijk *et al.* (2016). An adjustable time step $\Delta t$ was set to limit the maximum Courant number to

| Run | $T_u$ | $H_l$ | $\Omega$ | $\Delta x, y, \Delta z$ | $R_\mathrm{D}$ | $H_\mathrm{D}$ | $R_\mathrm{fine}$ | $N_\mathrm{cell}$ | Duration | $N_\mathrm{CPU}$ | $t_\mathrm{Run}$ |
|---|---|---|---|---|---|---|---|---|---|---|---|
| | K | cm | s$^{-1}$ | cm | cm | cm | cm | million | s | | h |
| 1 | – | – | 0 | 0.05 | 5.5 | 8 | 2.9 | 6.1 | 15 | 64 | 19 |
| 2 | – | – | 4.2 | 0.05 | 5 | 6 | 3 | 3.1 | 10 | 12 | 29 |
| 3 | – | – | 1.1 | 0.05 | 2.9 | 6 | 1.6 | 1.3 | 10 | 12 | 7 |
| 4 | – | – | 2.1 | 0.05 | 2.9 | 6 | 1.6 | 1.3 | 10 | 2 | 25 |
| 5 | – | – | 2.1 | 0.05 | 2.9 | 6 | 1.6 | 1.3 | 20 | 8 | 24 |
| 6 | – | – | 4.2 | 0.05 | 5 | 6 | 3 | 3.1 | 10 | 12 | 33 |
| 7 | – | – | 4.2 | 0.05 | 5 | 6 | 3 | 3.1 | 10 | 32 | 6 |
| 8 | 375 | 4 | 0.5 | 0.05 | 14 | 15 | 4 | 7.6 | 150 | 64 | 92 |
| 9 | 375 | 4 | 0.3 | 0.05 | 21 | 12 | 4 | 9.2 | 90 | 64 | 64 |

Table 4.2: Simulation parameters. Variables are defined as $T_u$: upper layer fluid temperature; $H_l$: lower layer thickness; $\Delta x, y$: mean value of the small grid spacing in the horizontal direction; $\Delta z$: grid spacing in the vertical direction; $R_\mathrm{D}$: radius of the computational domain; $H_\mathrm{D}$: height of the computational domain; $R_\mathrm{fine}$: radius of the region with small grid spacings; $N_\mathrm{cell}$: computational cell number; $N_\mathrm{CPU}$: CPU number; $t_\mathrm{Run}$: wall clock time for each simulation. The source fluid temperature was $T_s = 650\,\mathrm{K}$ for every each simulation and the temperature for the fluid of uniform ambient or the lower layer in two-layer ambient was $T_0 = 293\,\mathrm{K}$. In simulations with uniform ambient, $T_u$ and $H_u$ are indicated as –.

0.5, where the Courant number was defined as the ratio between the velocity and the product of the grid spacing and time step in each direction. The background rotation angular velocity, $\Omega$, ranged from $0.1\,\mathrm{s}^{-1}$ to $4.2\,\mathrm{s}^{-1}$.

## 4.5 Results

A total of nine LES runs are reported upon here with parameters listed in table 4.2. The simulation in a non-rotating uniform ambient, see table 4.2 (1), is run to validate the SGS model. The simulation results are compared with the MTT model results.

### 4.5.1 Validation of LES

An instantaneous snapshot of temperature on a vertical slice passing through the plume origin is shown in figure 4.2 (a) at $t = 2.5\,\mathrm{s}$. The plume becomes turbulent right after entering into the computational domain, which suggests
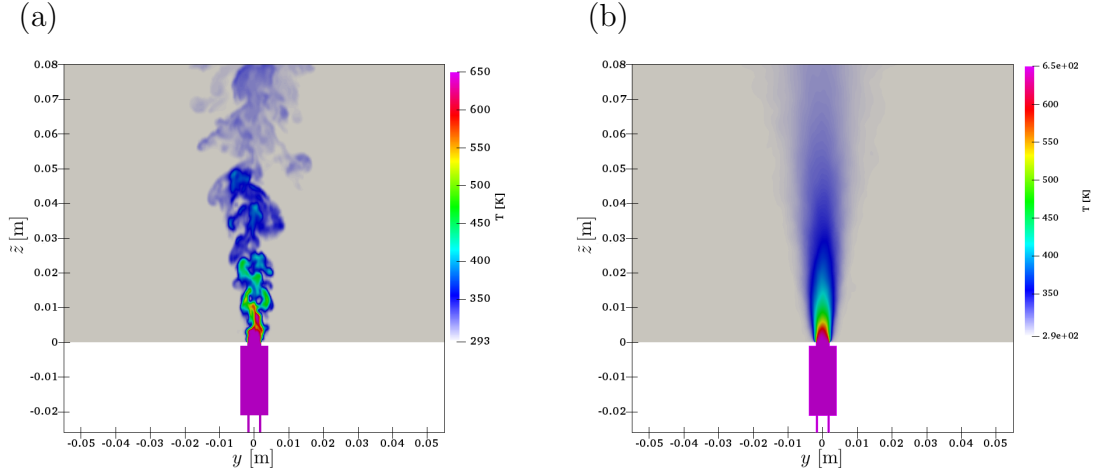
Figure 4.2: Side-view image of the temperature, $T$, from Run 1 (uniform ambient, no background rotation) at a vertical slice passing through the plume origin. (a) The instantaneous $T$ at t=2.5 s; (b) the mean value of $T$ in the time range of $[2.5, 15]$ s.

that our design of the chamber works well for establishing turbulent flow right above the source opening. The values of $T$ on the same slice as figure 4.2 (a) are averaged in the time range of $[2.5, 15]$ s, and the resulting average image is shown in 4.2 (b). This latter figure shows a symmetry about the centre-line of the plume that is absent in the instantaneous image.

At the centre-line of the plume, the time-averaged vertical velocity, $w_c$, and the temperature, $T_c$, are sampled. The centre-line, time-averaged reduced gravity, $g'_c$ is calculated from (4.4) and (4.5). The entrainment coefficient, calculated under the assumption that the plume can be modelled analytically using a top-hat formulation, is calculated from (4.13) at each level and is shown in figure 4.3 (b). The value of $\alpha$ decreases with height approaching to $\sim 0.2$ at $z - z_v = 6$ cm. Similarly, van Reeuwijk *et al.* (2016) also reported that $\alpha$ approached a constant value at large heights from a very large value nearby the source in their the DNS study. The mean value of $\alpha$ in the range from 2 cm to 7 cm is 0.22, which is larger than the typical value of 0.14 measured from experiments. We suspect the reason for the discrepancy is that the one-equation SGS model over computes the eddy viscosity $\nu_t$. Fortunately, when comparing
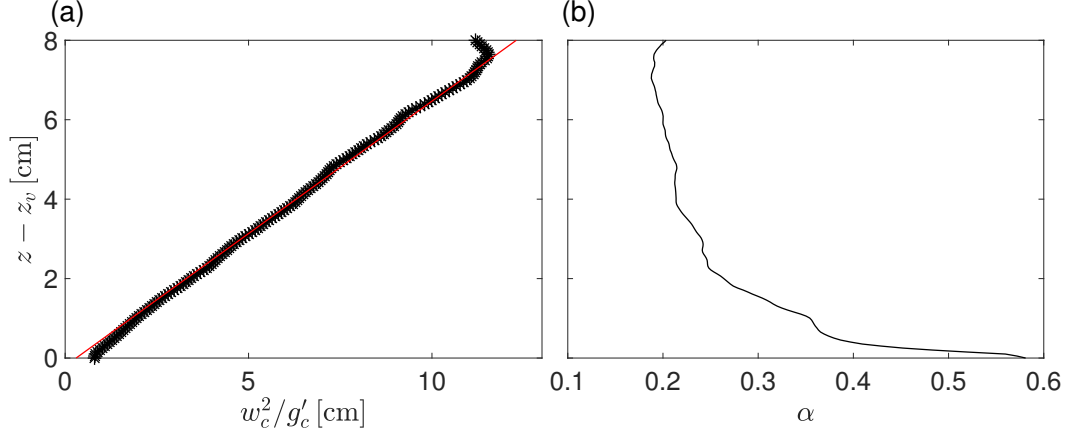
Figure 4.3: (a) The ratio $w_c^2/g_c'$ versus $z - z_v$ (black points). The red line is the corresponding best fit line with a forced slope of $\frac{2}{3}$. (b) The calculated $\alpha$ versus $z - z_v$.

the simulation results with experimental measurements, variables, such as the radius of the lens, are presented in non-dimensional form and hence the $\alpha$ value does not influence the comparison.

The ratio $w_c^2/g_c'$ is plotted against the vertical coordinate of the computational domain $\tilde{z} = z - z_v$ in figure 4.3 (a). According to (4.15), $z - z_v$ varies linearly with $w_c^2/g_c'$ with a slope of $\frac{2}{3}$, regardless of the value of the entrainment coefficient $\alpha$. A best-fit line with a forced slope of $\frac{2}{3}$ is obtained using data in a range from 2 cm to 7 cm. Even though the slope of the best fit line is forced to be $\frac{2}{3}$, this best fit line still fits the numerical data quite well. The extrapolation of this line of best fit to the vertical axis gives us a means, through (4.15), of estimating the virtual origin distance $z_v$. By this process, we estimate that $z_v = 0.20$ cm. We consider this estimate to be more accurate than that obtained using the analytical method of Hunt & Kaye (2001) because their approach assumes a constant value for $\alpha$, which is at odds with figure 4.3 (b). The discrepancies close to the upper boundary, as shown in figure 4.3 (a), are caused by boundary condition effects.

Further comparisons between theory and numerics can be made by considering the radial variation of $w$ and $g'$ as measured at the prescribed heights. Such is the purpose of figure 4.4, which shows normalized vertical velocities and re-
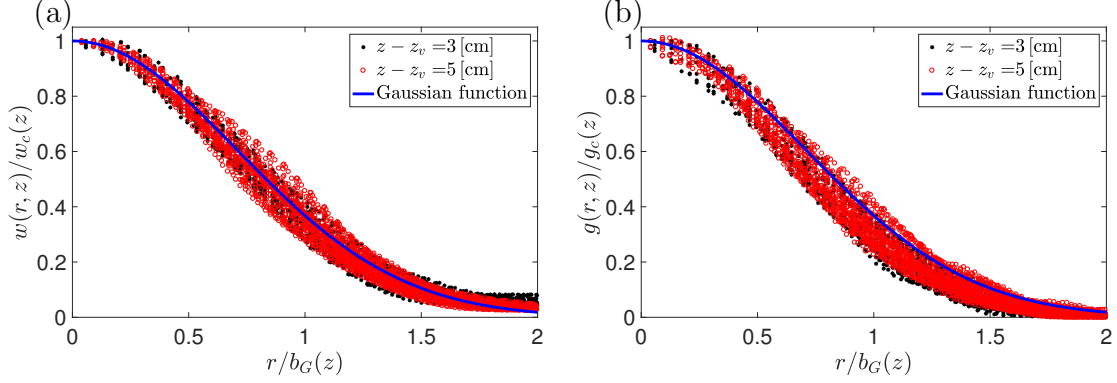
Figure 4.4: The normalized vertical velocity, $w(r, z)/w_c(z)$, and reduced gravity, $g(r, z)/g_c(z)$, from simulation versus the normalized radial coordinate at two different heights. The blue curves show the Gaussian function.

duced gravities plotted against $r/b_G(z)$ where $b_G(z)$ is the radius of a Gaussian-profile plume. Numerical data are measured at two different elevations, namely $z - z_v = 3\,\mathrm{cm}$ and $z - z_v = 5\,\mathrm{cm}$. The Gaussian function $\exp\left(-\frac{r^2}{b_G^2(z)}\right)$ is plotted in each panel of figure 4.4 as a blue curve. The vertical velocity and reduced gravity overlap with the Gaussian function, consistent with numerous experimental investigations e.g. George *et al.* (1977), Ramaprian & Chandrasekhara (1989) and Ezzamel *et al.* (2015), suggesting that these variables indeed follow a Gaussian distribution. Even though figure 4.3 (b) shows the entrainment coefficient, $\alpha$, varies with height, we note that $\frac{w_c^2(z)}{g_c'(z)}$ calculated from the numerical simulations can fit (4.15), which is derived from the MTT model results, in which $\alpha$ is assumed as a constant. This fact suggests that (4.15) is also applicable to the plume with a height-dependent $\alpha(z)$. To this end, and considering the comparisons shown in figures 4.3 and 4.4, we believe the numerical simulations can well describe a turbulent plume in a non-rotating uniform ambient fluid.

## 4.5.2 Simulations with background rotation

### Rotating uniform ambient

We assume the turbulence parameterized by the SGS model is not affected by the Coriolis force as such motions occur on small spatial and fast-time scales, so that we can still use the same configuration as the simulation without back-

89
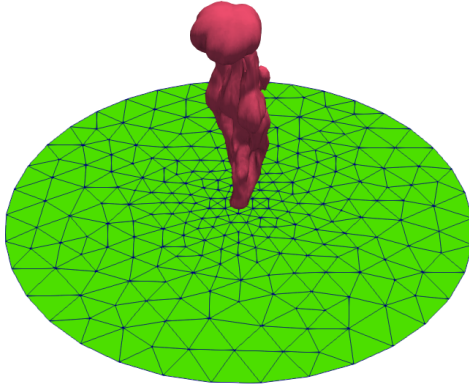
(a) Snapshot, $t = 0.8\,\mathrm{s}$        (b) Snapshot, $t = 1.3\,\mathrm{s}$
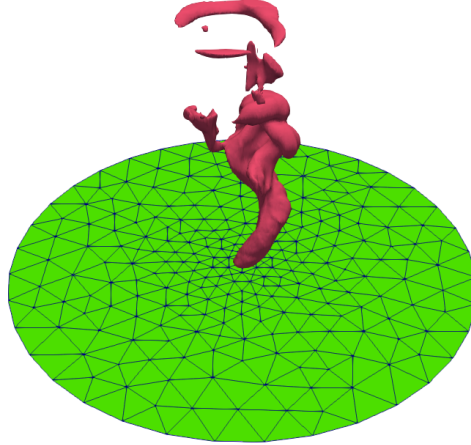
Figure 4.5: Two bird's-eye view images at $t = 0.8\,\mathrm{s}$ and $1.3\,\mathrm{s}$ from Run 2. A critical value of $T = 330\,\mathrm{K}$ is indicated with the red iso-surface. A schematic diagram of the mesh structure is shown along the bottom boundary, in which the grid spacing in increased for the convenience of illustration.

ground rotation. Two bird's-eye view images from Run 2 are shown in figure 4.5. A contour of the $T = 330\,\mathrm{K}$ isotherm is plotted and indicated by the red iso-surface. As shown in figure 4.5, the plume ascends to the upper boundary in a small time of $t = 0.8\,\mathrm{s}$ then starts to be deflected and precesses anticyclonically beginning around $t = 1.3\,\mathrm{s}$.

In figures 4.6 (a) and (b), the temperatures measured along horizontal cross-sections located $z = 1\,\mathrm{cm}$ and $2\,\mathrm{cm}$ above the source are shown at $t = 2\,\mathrm{s}$. (We choose vertical distances of $1\,\mathrm{cm}$ and $2\,\mathrm{cm}$ because the precession originates close to the plume source.) The horizontal location of the maximum temperature of the precessing plume is tracked at each instantaneous time and this location is regarded as the instantaneous plume centre at each height in question. In figure 4.6 (b), the angular displacement, $\theta$, from the $x-$axis of a line connecting the centre of the cross-section to the instantaneous plume centre is indicated. The plume precession frequency can then be found from plots of $\cos\theta$ or $\sin\theta$ versus non-dimensional time, $t\Omega$. Plots of this type are shown in figures 4.6 (c) and (d), which clearly show that the plume precesses anticyclonically about the
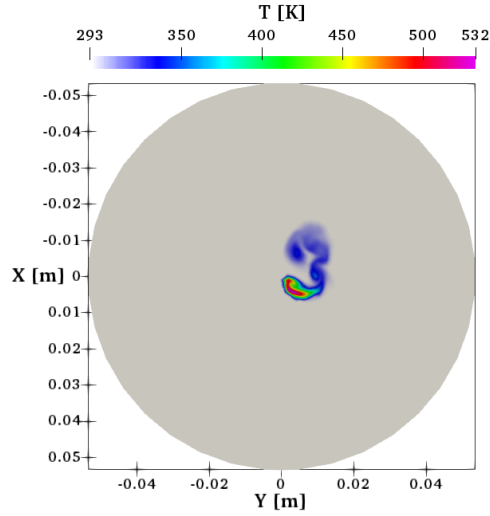
(a) Snapshot, $z = 1\,\mathrm{cm}$    (b) Snapshot, $z = 2\,\mathrm{cm}$
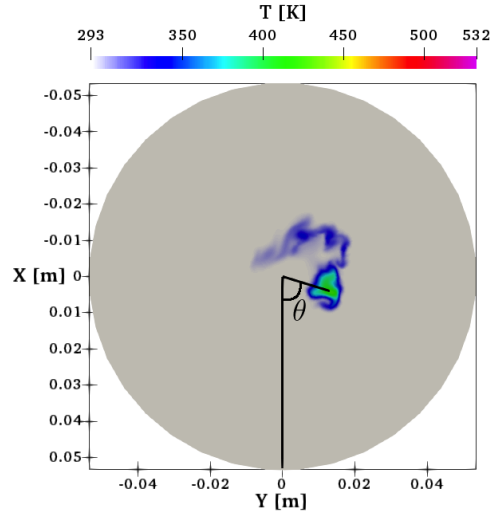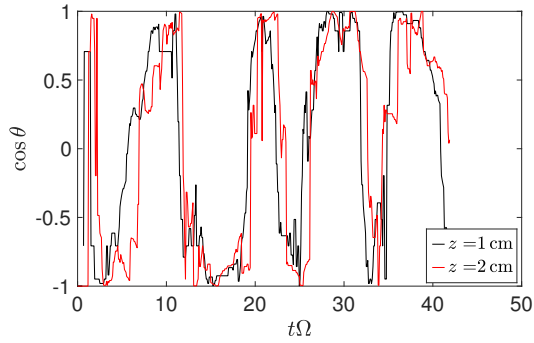
(c) $\cos\theta$ vs. time    (d) $\sin\theta$ vs. time
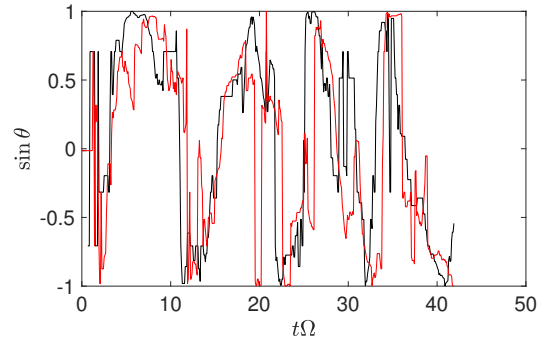
Figure 4.6: Temperature distributions from Run 2 measured along horizontal cross-section planes located $z = 1\,\mathrm{cm}$ and $2\,\mathrm{cm}$ above the source at $t = 2\,\mathrm{s}$. (c) $\cos\theta$ versus $t\Omega$; (d) $\sin\theta$ versus $t\Omega$. The angle $\theta$ is defined in panel (b).
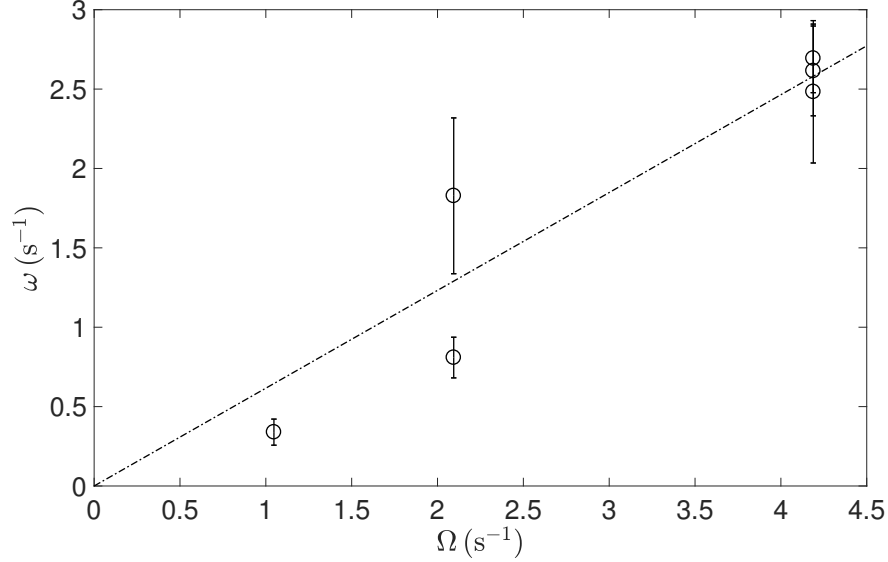
Figure 4.7: Measured plume precession frequency, $\omega$, plotted against the background rotation rate, $\Omega$. The dash dotted line is the best-fit line with a forced intersection of 0.

$z$-axis. The non-dimensional period, $t_p\Omega$, of the precession is estimated from figures 4.6 (c) and (d) by counting the total time between the first and last peaks then dividing by the number of intervening peaks. From this admittedly crude approach, we estimate that $t_p\Omega \approx 10$. The precession frequencies, $\omega$, are determined from the precession periods and then compared across simulations with different $\Omega$; results are compiled in figure 4.7. Although there is some scatter in the data, this figure suggests an approximately linear relationship between $\omega$ and $\Omega$. The best-fit line has a slope of $0.62\pm0.27$, which is moderately larger than the values of 0.52 from experiments reported in Chapter 3 and 0.40 given by Frank *et al.* (2017).

The inclination of the precessing plume can be computed with reference to the polar angle, $\phi$, that the plume makes with respect to the vertical axis. The value of $\phi$ can be calculated trigonometrically provided the planar location of the temperature maximum is known. Denoting as $l_p$ the planar distance from this temperature maximum to the centre of the plane, we find that

$$\phi = \arctan\left(l_p/z\right), \tag{4.16}$$
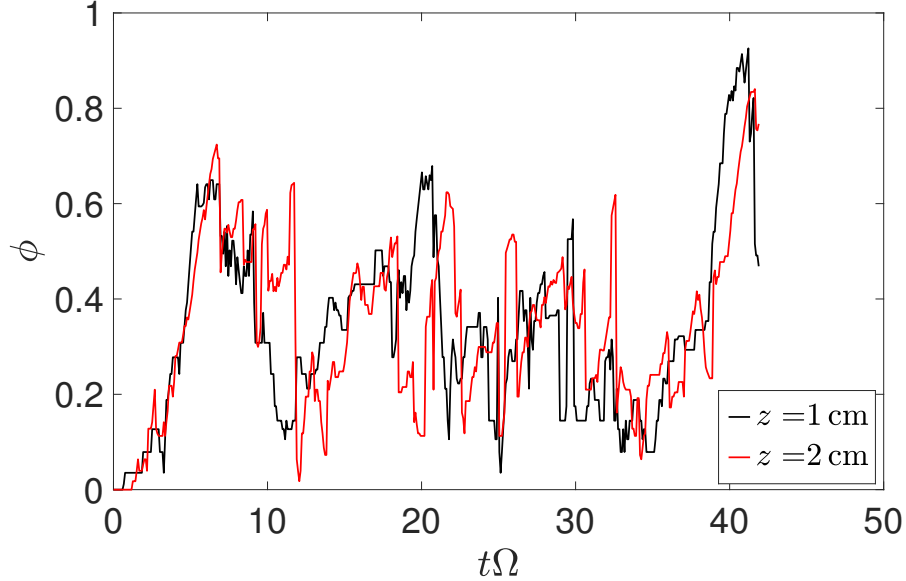
Figure 4.8: The polar angle, $\phi$, measured at $z = 1\,\mathrm{cm}$ and $2\,\mathrm{cm}$ and plotted versus nondimensional time. The parameters are indicated in table 4.2, row 2.

where $z$ indicates the vertical elevation from the virtual source.

From figure 4.8, the polar angle, $\phi$, also exhibits a time-variable behaviour. The mean value of the polar angle, $\bar{\phi}$, is calculated at elevations $z = 1\,\mathrm{cm}$ and $z = 2\,\mathrm{cm}$ in the time period from the onset of precession to the end of each simulation. In figure 4.9, $\bar{\phi}$ is plotted against $\Omega$. In contrast to figure 4.8, we observe relatively little variation of one variable on the other. The average value measured over all six numerical simulations (Runs 2 to 7, inclusive) is $0.34 \pm 0.038$.

**Rotating two-layer ambient**

Table 4.2, rows 8 and 9 list the parameters for the simulations of a plume in a rotating two-layer stratified ambient fluid. The ambient is set with a lower layer of depth $H_l = 4\,\mathrm{cm}$ filled with a reference fluid having a temperature of $T_0$ and density of $\rho_0$. In Run 8, the upper layer has depth $H_u = 11\,\mathrm{cm}$ and is filled with a fluid having a comparatively higher temperature of $T_u = 375\,\mathrm{K}$ and a density of $\rho_u = 0.984\,\mathrm{cm}^3\,\mathrm{s}^{-1}$. The reduced gravity between the upper and
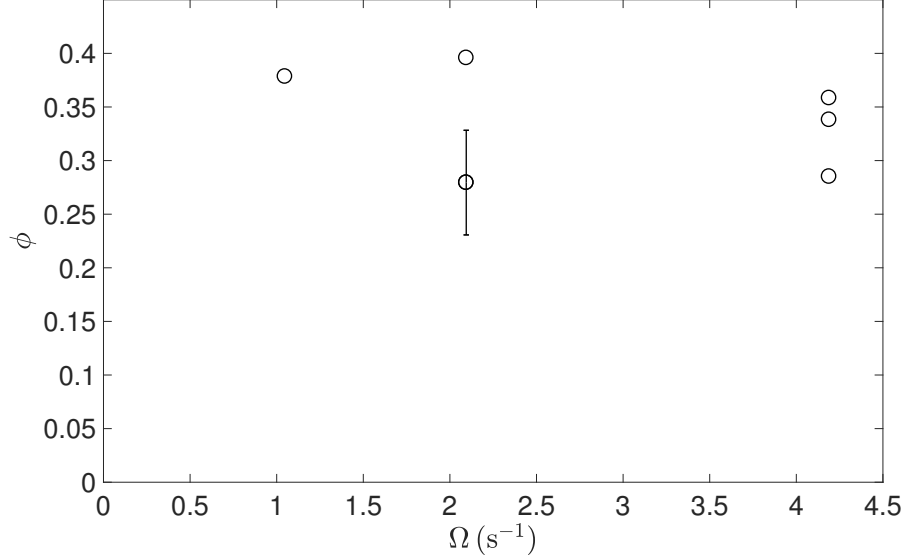
Figure 4.9: The mean value of the polar angle, $\phi$, of the precessed plume from the $z$-axis versus the background rotation rate, $\Omega$. A representative error bar is plotted on one symbol.

lower layers is calculated to be

$$g'_{ul} = g \left( \frac{\rho_0 - \rho_u}{\rho_0} \right) = g\beta \left( T_u - T_0 \right) = 16.07 \, \text{cm s}^{-2}. \tag{4.17}$$

The value of $g'_{ul}$ is comparable with that from the experiments of Chapter 3. Given the plume source buoyancy flux of $F_s = 57.15 \, \text{cm}^4 \, \text{s}^{-3}$, lower layer thickness of $H_l = 4 \, \text{cm}$, virtual source distance, $z_v = 0.2 \, \text{cm}$, and entrainment coefficient $\alpha = 0.22$, the average reduced gravity of the plume at the level of the ambient interface is calculated to be $g'(H_l) = 4.112 \, \text{cm s}^{-2}$. According to (3.5), the corresponding $\Lambda$ value is calculated to be 0.28, which suggests the plume cannot penetrate through the interface initially as it impinges upon the ambient interface.

In figure 4.10, we present snapshot images in vertical cross-sections coincident with the $y - z$ plane. The passive tracer is shown in red and shows the flow evolution from an ascending plume impinging upon the ambient interface to eventual penetration. This mechanism driving this process is described in Chapter 3.

Similar to the laboratory experiments, we consider a horizontal slice along

94

(a) Snapshot, $t = 2\,\mathrm{s}$



(c) Snapshot, $t = 30\,\mathrm{s}$



(b) Snapshot, $t = 15\,\mathrm{s}$



(d) Snapshot, $t = 130\,\mathrm{s}$
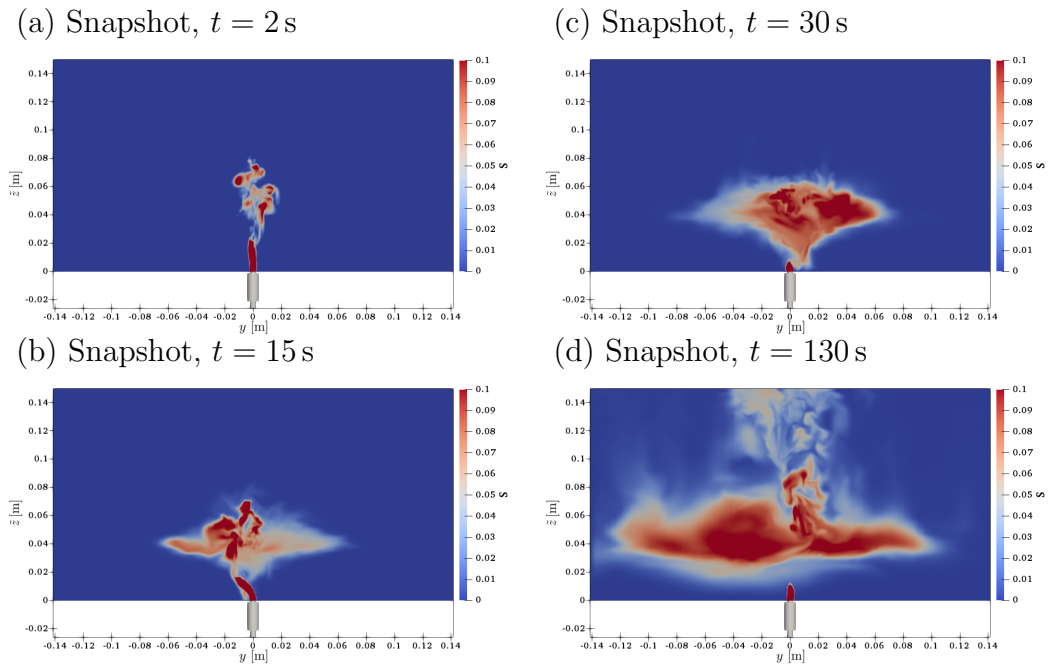


Figure 4.10: Snapshots of a plume in a rotating two-layer fluid corresponding to Run 8. (a) $t = 2\,\mathrm{s}$, the plume rises to the interface and overshoots. (b) $t = 15\,\mathrm{s}$, the overshot plume returns back to its level of neutral buoyancy and intrudes along the ambient interface. (c) $t = 30\,\mathrm{s}$, the thickness of intrusion continuously increases and an anticyclonic lens forms. (d) $t = 130\,\mathrm{s}$, the plume penetrates through the interface.
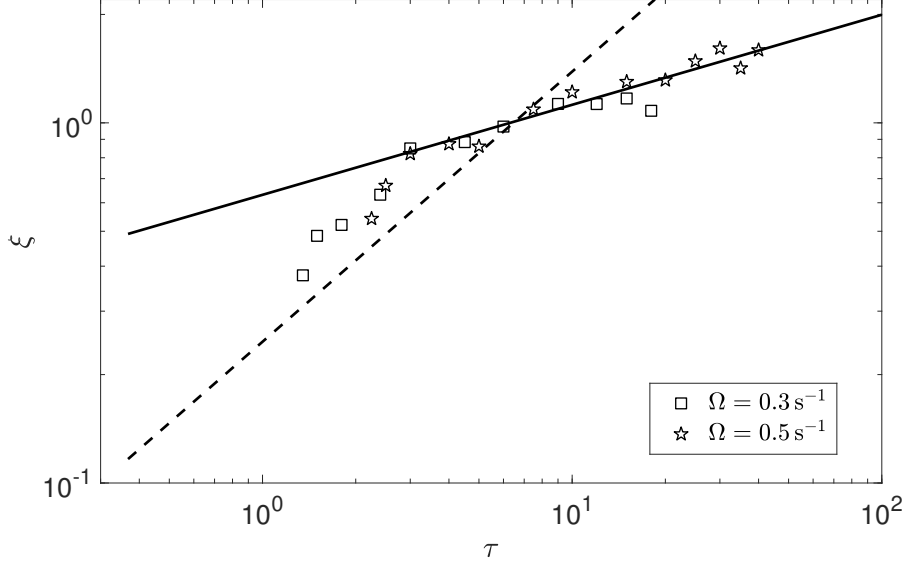
Figure 4.11: Non-dimensional radial position of the intrusion front, $\xi$, vs. non-dimensional time, $\tau$, defined in (3.18). The black dashed and solid lines are the best fit lines from the laboratory experimental measurements described in Chapter 3.

the level of the ambient interface. The maximum area of the lens can be determined with reference to the passive tracer concentration, $C$. A critical concentration value of $C = 0.01$ is regarded as the intrusion (or lens) boundary from which the lens cross-sectional area at the level of the interface can easily be determined by numerical integration. Thereafter, the average radius of the lens can be obtained through (3.22). Figure 4.11 shows the non-dimensional intrusion (or lens) radius, $\xi$, versus non-dimensional time, $\tau$, defined in (3.18). For small times, (3.19) indicates that the discharged plume fluid advances in the form of an intrusive gravity current and $\xi$ follows a $\frac{3}{4}$ power law against $\tau$. While at large times, the intrusion is more properly described as an expanding lens which is in a quasi-geostrophic state and the non-dimensional lens radius $\xi$ follows a $\frac{1}{4}$ power law against $\tau$. The black dashed and solid lines are the best-fit lines given as (3.24) from experiments in Chapter 3. The simulation results match well with the experimental results.

## 4.6 Conclusions

A plume rising through a non-rotating uniform density, a rotating uniform density and a rotating, two-layer stratified ambient fluid is investigated using LES simulations. In the former case, we draw comparisons against the analogue theoretical predictions associated with the MTT model. This comparison, in particular figures 4.3 (a) and 4.4, suggests that the one-equation eddy-viscosity SGS model of LES works well for simulating turbulent plumes.

Consistent with experimental observations, the plume is found to precess in the numerical simulations and the precession frequency shows a linear relationship with background rotation rate, which confirms the experimental observations in Chapter 3. Furthermore, the precession polar angle is found to be a constant independent of the background rotation rate. When the ambient is two-layer stratified, the plume reaches the ambient interface and spreads along it. The Coriolis force limits the intrusion within a small area above the plume source to form a lens. Due to the plume re-entraining fluid from the lens, the plume eventually penetrates through the interface. The front position of the intrusion (or lens) formed from discharged plume fluid shows good agreement with experimental measurements at both small and large times.

# Chapter 5

# Summary and outlook

## 5.1   Discussion and summary

In this thesis I presented laboratory experimental and numerical studies of turbulent plumes in a two-layer stratified ambient fluid in circumstances without (Chapters 2 and 4) and with (Chapters 3 and 4) background rotation. In the former circumstance, I experimentally investigated the scenario of a line-source descending plume evolving in a time-evolving two-layer stratified ambient fluid in which the upper layer was made to deepen due to the outflows at the bottom while inflows at the surface kept the total volume fixed. In the latter circumstance the ambient fluid around a point-source plume evolved in time due to rotation that inhibited the radial spread of discharged plume fluid as it reached the neutral density level at the two-layer fluid interface.

A non-dimensional number $\Lambda$ is used to characterize the ratio between the reduced gravities of the plume and the lower layer fluid with respect to the upper layer fluid. For $\Lambda < 1$ the plume fluid at the interface is lighter than the lower layer and so spreads at the interface. For $\Lambda > 1$ the plume penetrates through the ambient interface and descends into the lower layer. Because a plume's reduced gravity decreases with depth due to entrainment, $\Lambda$ is smaller if the upper layer depth is larger. Indeed, if the upper layer is sufficiently deep so that $\Lambda < 1$ and then the plume spreads at the interface. Conversely, for small upper layer thickness (large $\Lambda$), the plume freely penetrates through

the interface to depth and spreads along the bottom. In the case of a time-evolving ambient fluid as studied in Chapter 2, the upper fluid depth increased in time with the plume initially penetrating to depth. Whether or not the plume eventually transitioned to spread entirely at the interface was characterized by a non-dimensional number $\lambda$. Here $\lambda$ is the limit of $\Lambda$ as the upper layer thickens approaching its time independent value so that the volume flux of the plume crossing the interface equals the outflux from the lower layer. A transition from totally penetrating to totally spreading can only occur when $\lambda < 1$. In this case, there is an intermediate regime, observed for moderate $t$, where a part of the plume fluid is detrained at the interface and the remaining fraction of the plume fluid falls to depth.

Even though I only investigated the transition process from penetrating to spreading, qualitatively, one can also expect a reverse process, from spreading to penetrating, can occur if the inflow and outflow are reversed, namely the outflow is in the upper layer and inflow is in the lower layer. The reverse transition can also occur in the circumstance of marine effluent outfall from the seafloor during the period from summer, when the upper mixed layer is thin, to winter, when the upper mixed layer is thick and hence the distance from the outfall source to the interface decreases.

In order to explore large scale plumes occurring on Earth, the influence of background rotation is taken into account in experiments studying a descending point-source plume in the two-layer stratified ambient fluid. One remarkable phenomenon of a plume in a rotating ambient fluid is that it precesses anticyclonically near the source. The background rotation also influences the rotationally confined lateral intrusions formed by the plume fluid that spreads at the ambient interface. The Coriolis force alters the direction of the intrusion to form an anticyclonically rotating lens which is in quasi-geostrophic balance. From the lens, the plume re-entrains the relatively dense fluid, in a manner similar to a filling box process. Meanwhile the lens gradually increases its radius and thickness because of the continual supply of fluid discharged by the plume.

Even though $\Lambda < 1$ at the onset (so that the plume does not penetrate through the interface), eventually the plume can penetrate through the interface as it becomes sufficiently dense due to the re-entrainment of lens fluid. In contrast, the intrusion from a descending plume spreading at the interface in a laterally unbounded ambient fluid without background rotation propagates indefinitely far away suggesting that the eventual transition to a penetrating regime is impossible. From scaling analysis and also inspired by the work of Kaye & Hunt (2007) and Griffiths & Linden (1981), the advance of the intrusion (or lens) front is modelled as an intrusive gravity current at small times and as a quasi-geostrophic expanding lens at large times. The experimental results supported the suggested superposition of analytical models and transition from one flow regime to the other occurred after one rotation period.

LES simulations with OpenFOAM showed good quantitative agreement with the MTT model predictions for plumes in a non-rotating uniform ambient fluid in terms of the linear relationship of $\frac{w_c^2(z)}{g_c'(z)}$ and $z$. Plume precession is well-captured in the simulations including the Coriolis force in a uniform or two-layer stratified ambient fluid. The precession frequency is comparable though somewhat larger than that measured in experiments. The precession polar angle is measured from simulations and appears to be independent of the background rotation rate. When plotted versus the non-dimensional time $\tau$, the (small time) non-dimensional front position of the intrusive gravity current and the (large time) non-dimensional front position of the expanding lens show good agreement with experimental measurements. These preliminary results suggest that LES simulations are able to capture the essential plume dynamics. As such, analogue LES models can, in future, be used in studying additional aspects of plume rise and spread along an ambient interface. Whereas this statement may seem overly generic, we devote the next subsection to a more detailed discussion of possible extensions to the work already begun in this thesis.

## 5.2 Future work

Some processes involving my research have been observed qualitatively but have not yet to be quantitatively examined. Here I list two topics in particular that would be interesting to examine in the future.

### 5.2.1 Parameterization of plume splitting

In the experiments reported upon in Chapter 2, the plume is found to split at the ambient interface during the transition from penetrating through to spreading along the ambient interface. Although this phenomenon is qualitatively explained, the question of quantitatively describing or parameterizing this splitting phenomenon still remains. For example, what fraction of plume fluid is detrained at the ambient interface when the plume both penetrates into the lower layer and spreads at the interface? As argued in Chapter 2, plume splitting should be affected by the parameter $\Lambda$, which characterizes the ratio between the mean value of the reduced gravity of the plume at the ambient interface level and the reduced gravity between upper and lower layer fluids. Other parameters may also play a role in the dynamics of plume splitting, such as the thickness of the ambient interface, the plume radius and the mean momentum at the interface level. Moreover, the splitting fluid intrudes along the ambient interface and modifies the density profile of the initial two-layer stratification around the plume. Of course, whatever fluid is discharged by the plume can be re-entrained by the plume at some later instant of time. These detrainment and re-entrainment processes make it challenging to analyze detrainment under a specific ambient stratification profile. Therefore as a first step, the task is to create an ideal experiment, in which the modification to the ambient stratification by detrainment should be avoided. Once the above task solved, it should be possible to develop a parameterization to describe the plume detrainment rate into an intrusion at the detrainment level in arbitrary ambient density stratification. Such a parameterization could then be coupled with a

| Expt. | $\Omega$ | $\rho_l$ | $\rho_s$ | $Q_s$ | $H_u$ | $\Lambda$ | $\mathrm{Fr}_i$ | $\mathrm{Ro}(H_u)$ | $T_p$ |
|---|---|---|---|---|---|---|---|---|---|
| | $\mathrm{s}^{-1}$ | $\mathrm{g\ cm}^{-3}$ | $\mathrm{g\ cm}^{-3}$ | $\mathrm{cm}^3\ \mathrm{s}^{-1}$ | cm | | | | s |
| T1 | 0.3 | 1.00765 | 1.07064 | 0.59 | 6.99 | 0.289 | 2.84 | 5.16 | 110 |

Table 5.1: Parameters for the tornado-appearing experiment. Variables are the same as in table 3.1.

filling box model and be applied to the experiments reported in Chapter 2 with the relations between $\lambda$ and the start/end times of the transition in (2.27) being predicted from this new model.

### 5.2.2 Plume "tornado" phenomenon

In most experiments of a plume in a rotating environment, the plume near the source was observed to precess while eddies in the plume acted efficiently to entrain ambient fluid causing its width to increase with depth. However, in several of the laboratory experiments with a rotating uniform or two-layer stratified ambient fluid, an initially precessing plume was observed to develop into a tubular vortex, referred to here as a "tornado". (Frank (pers. comm.) also observed this phenomenon in few of her experiments of plumes in a rotating uniform ambient fluid.) One example is shown in figure 5.1 and the parameters are given in table 5.1. Remarkably, these parameter values are close to those of Experiments 14 and 15 in table 3.1, but the plume in Experiment T1 exhibited a very different behaviour, which we now describe in detail.

At small times the plume was less dense than the lower layer ambient fluid ($\Lambda < 1$), and so it spread along the interface and formed a lens, as shown in figure 5.1 (a). The plume also precessed anticyclonically near the source at early times, which was the same behaviour observed for the corresponding experiments reported upon in Chapter 3. Later, however, the precessing plume evolved into a tubular vortex in the upper layer, as shown in figure 5.1 (b). The radius of this vortex was smaller than that of the plume at the ambient interface level, which suggested the entrainment was suppressed likely because of strong cyclonic flows surrounding and within the plume. The density of fluid in the

(a) Side view, $t = 40\,\mathrm{s}$

(b) Side view, $t = 85\,\mathrm{s}$

(c) Side view, $t = 170\,\mathrm{s}$

(d) Side view, $t = 240\,\mathrm{s}$
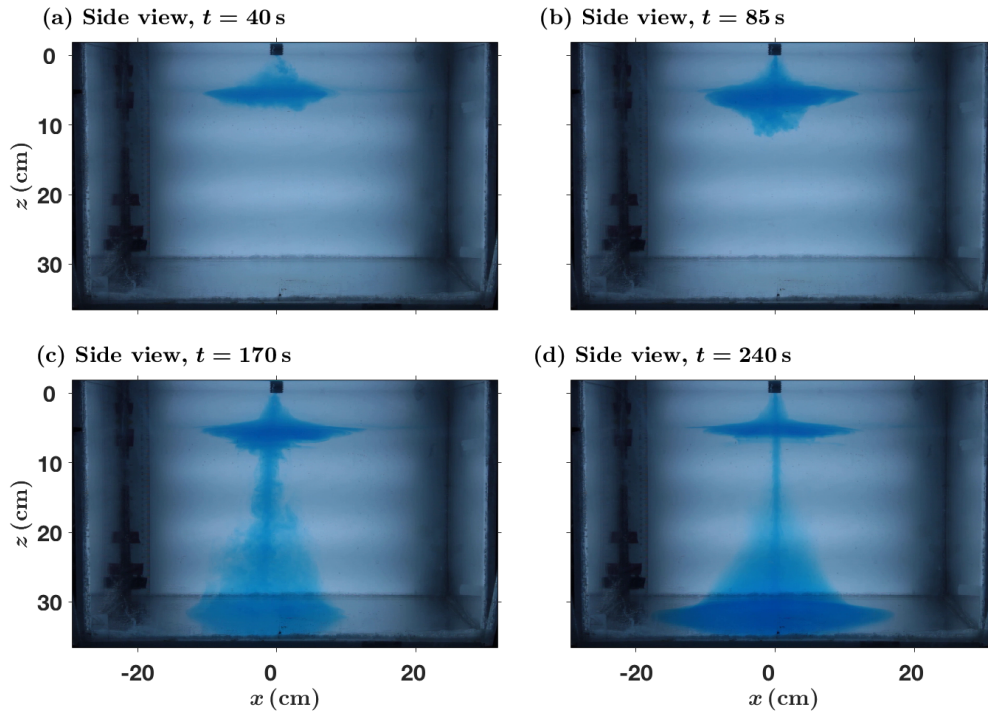
Figure 5.1: Snapshots at different times from the side-view movie of Experiment T1 (see table 5.1). (a): Similar to figure 3.2 (a), the plume fluid spreads laterally after reaching the ambient interface. Thereafter, however, (b) a tubular vortex appears within the lens in the upper layer. (c): The tubular vortex penetrates through the ambient interface and reaches the bottom, forming a coherent vortex from the nozzle to the bottom. (d): The tubular vortex becomes axisymmetric and maintains its shape for another two minutes.

vortex consequently was much larger than that in an entraining plume at the same level and so the vortex penetrated through the ambient interface more quickly. Indeed, the onset of the penetration through the ambient interface in Experiment T1 was 100 s, which was much earlier than the plume penetration time of 232 s in Experiment 14 (table 3.1). This despite the fact that $\Lambda = 0.289$ in Experiment T1 (table 5.1) was even smaller than $\Lambda = 0.364$ in Experiment 14 (table 3.1). After the onset of penetration, the tornado extended over the entire depth of the ambient fluid between the nozzle and the bottom, as shown in figure 5.1 (c). The tornado continued to develop to be axisymmetric about the vertical axis and maintained this state for about two minutes, as shown in figure 5.1 (d). Eventually the tornado shifted laterally so as not to be situated below the nozzle. Thereafter the plume precessed again and exhibited entraining eddies along its length.

Efforts have been made to investigate the mechanism of the tornado and its formation. The first step to control experimental conditions very precisely to repeat this tornado experiment regularly did not, alas, succeed: the plume tornado only appeared occasionally and could not reliably be reproduced even after setting identical experiment parameters, covering the tank opening and allowing a long spin-up time. So far attempts to reproduce the tornado phenomenon in numerical simulations have also been unsuccessful. Such non-repeatability coupled with the eventual disappearance of the tornado even in nominally "successful" experiments like that of figure 5.1 makes it a challenge to diagnose the conditions leading to tornado formation and its governing properties.

## 5.3   Final remarks

Classical plume theory and its extensions in uniform or linearly stratified ambient fluid lead to flows that are statistically steady in the long time limit, $t \to \infty$. The splitting phenomenon reported in this thesis demonstrates the inadequacy of this modelling approach for plumes in a time-evolving ambient where the plume transitions between interface spreading and penetrating. In this thesis,

the investigation of the plume in a time-evolving ambient fluid may help in the design of marine effluent diffusers and of natural ventilation systems. A further contribution of this thesis is to illustrate the significant differences of plume/ambient behaviour once rotation is introduced. Indeed, both the precession of rotating plumes and tornado formation illustrate that there are still poorly understood physical processes governing plumes in a rotating ambient fluid. The study in this thesis reveals that the background rotation can force a transition from plume spreading to interfacial penetration. This has important implications when gauging the efficacy of deep convection in marine settings.

# Appendix A

# Turbulent entrainment

Plumes in environments usually appear to be fully turbulent, characterized by a large Reynolds number. The radius of an ascending or descending turbulent plume increases as the plume flows away from the source. This spread is due to the turbulent entrainment of ambient fluid. Laboratory experiments (Westerweel *et al.*, 2005; Chauhan *et al.*, 2014) and numerical simulations (van Reeuwijk & Holzner, 2014) have shown that the entrainment at the interface between a turbulent flow and a non-turbulent ambient fluid consists of two processes, namely "nibbling" and "engulfment". Da Silva *et al.* (2014) described the nibbling as a viscous diffusive process resulting from small-scale motions. By contrast, the engulfment is an enveloping processes driven by large-scale eddies. From relevant studies of turbulent jets, e.g. Mathew & Basu (2002); Westerweel *et al.* (2005), nibbling contributes much more than engulfment to the entrainment. However, precisely the opposite conclusion was obtained by other researchers. For example, in their experimental study of turbulent plumes, Burridge *et al.* (2017) argued that the nibbling has been misinterpreted because all entrained fluid must undergo the nibbling process in order to reach to the ultimate mixing state. As such, Burridge *et al.* (2017) redefined engulfment as any transport of ambient fluid into the extent of the plume with scales greater than the Taylor micro-scale. Based on this redefinition, Burridge *et al.* (2017) found that almost all of the entrainment of ambient fluid can be associated with engulfment.

As explained by Sreenivas & Prasad (2000), the reduced gravity of a plume in a uniform ambient fluid decreases downstream, which results in an unstable stratification within the plume. Due to this unstable stratification, a baroclinic torque enhances the production of vortices that make the plume entrain more fluid from the ambient than a turbulent jet. Jets are, of course, similar to plumes but are driven by a source momentum flux rather than by a source buoyancy flux.

# Appendix B

# Integral model of plume

According to experimental measurements, the radial distributions of vertical velocity and reduced gravity of a point-source plume follow a Gaussian-type profile (Ezzamel *et al.*, 2015; George *et al.*, 1977; Paillat & Kaminski, 2014; Ramaprian & Chandrasekhara, 1989). The time-averaged vertical velocity, $w_G(r, z)$ and reduced gravity, $g'_G(r, z)$, can be expressed in terms of axisymmetric Gaussian functions as

$$w_G(r, z) = w_c(z)\exp\left(-\frac{r^2}{b_G(z)^2}\right), \tag{B.1}$$

$$g'_G(r, z) = g'_c(z)\exp\left(-\frac{r^2}{b_G(z)^2}\right), \tag{B.2}$$

where $z$ is the vertical coordinate with the positive direction downstream of the plume source, $r$ is the radial coordinate from the horizontal centre of the plume, $w_c(z)$ and $g'_c(z)$ respectively are the vertical velocity and reduced gravity along the centre-line of the plume, and $b_G(z)$ is the plume radius. The plume volume, momentum and buoyancy fluxes are then expressed, respectively, as

$$Q(z) = 2\pi \int_0^\infty wr\mathrm{d}r = \pi w_c(z)b_G^2(z), \tag{B.3}$$

$$M(z) = 2\pi \int_0^\infty w^2 r\mathrm{d}r = \frac{\pi}{2}w_c^2(z)b_G^2(z), \tag{B.4}$$

$$F(z) = 2\pi \int_0^\infty wg'r\mathrm{d}r = \frac{\pi}{2}g'_c(z)w_c(z)b_G^2(z). \tag{B.5}$$

However, for analytical convenience, theoreticians often consider top-hat descriptions (Kumagai, 1984; Ma *et al.*, 2017; Morton, 1957), according to which

the time-averaged vertical velocity, $w(r, z)$, reduced gravity, $g'(r, z)$, in the top-hat profiles are written as

$$w(r, z) = \begin{cases} w(z), & \text{if } r \leqslant b(z), \\ 0, & \text{if } r > b(z), \end{cases} \tag{B.6}$$

$$g'(r, z) = \begin{cases} g'(z), & \text{if } r \leqslant b(z), \\ 0, & \text{if } r > b(z), \end{cases} \tag{B.7}$$

The plume volume, momentum and buoyancy fluxes are obtained from the top-hat plume to be

$$Q(z) = 2\pi \int_0^\infty wr\mathrm{d}r = \pi w(z)b^2(z), \tag{B.8}$$

$$M(z) = 2\pi \int_0^\infty w^2 r\mathrm{d}r = \pi w^2(z)b^2(z), \tag{B.9}$$

$$F(z) = 2\pi \int_0^\infty wg'r\mathrm{d}r = \pi g'(z)w(z)b^2(z). \tag{B.10}$$

From equations (B.3) to (B.5) and equations (B.8) to (B.10), the relations between the quantities $w_c(z)$, $g'_c(z)$ and $b_G(z)$ of a Gaussian plume and the analogue quantities of $w(z)$, $g'(z)$ and $b(z)$ of a top-hat plume can be found as

$$w_c(z) = 2w(z), \tag{B.11}$$

$$g'_c(z) = 2g'(z) \tag{B.12}$$

$$b_G(z) = \frac{1}{\sqrt{2}}b(z). \tag{B.13}$$

The foundational work of modelling a turbulent point-source plume using integral quantities like $Q$, $M$ and $F$ was first done by Morton *et al.* (1956). They derived conservation laws for the fluxes of volume, momentum and buoyancy, assuming a Boussinesq, self-similar plume satisfying the Taylor's entrainment hypothesis, which supposes the mean entrainment inflow into the plume is proportional to the characteristic vertical velocity at each height (Turner, 1986). Expressed mathematically, the conservation laws in question read as follows:

$$\frac{\mathrm{d}Q}{\mathrm{d}z} = 2\alpha\pi^{1/2}M^{1/2}, \tag{B.14}$$

$$\frac{\mathrm{d}M}{\mathrm{d}z} = \frac{FQ}{M}, \tag{B.15}$$

$$\frac{\mathrm{d}F}{\mathrm{d}z} = -Q\frac{\mathrm{d}g'_0}{\mathrm{d}z}. \tag{B.16}$$

Here $g_0'(z) = g(\rho_0(z) - \rho_{00})/\rho_{00}$ measures the reduced gravity of the ambient fluid of density $\rho_0(z)$ with respect to the reference density $\rho_{00}$, where $g$ is the acceleration due to gravity. The entrainment coefficient for a top-hat plume is denoted by $\alpha$ and $\alpha_G$ for a Gaussian plume, and it can be shown that $\alpha$ and $\alpha_G$ have the following relationship

$$\alpha = \sqrt{2}\alpha_G. \tag{B.17}$$

The entrainment coefficient was measured experimentally by numerous researchers including Morton *et al.* (1956), Baines & Turner (1969), George *et al.* (1977), Baines (1983) and Ezzamel *et al.* (2015) and Carazzo *et al.* (2006) summarized the typical values of $\alpha$ for the top-hat plumes varying between 0.1 and 0.16. For the top-hat model of interest here, we choose a moderate value as $\alpha = 0.14$.

## MTT model predictions

If the ambient has uniform density, (B.14) to (B.16) can be solved analytically yielding explicit expressions for $Q(z)$, $M(z)$ and $F(z)$ as follows

$$Q(z) = \frac{6\alpha}{5}\left(\frac{9\alpha}{10}\right)^{\frac{1}{3}} \pi^{\frac{2}{3}} F_s^{1/3} z^{5/3}, \tag{B.18}$$

$$M(z) = \left(\frac{9\alpha}{10}\right)^{\frac{2}{3}} \pi^{\frac{1}{3}} F_s^{2/3} z^{4/3}, \tag{B.19}$$

$$F(z) = F_s. \tag{B.20}$$

From equations (B.8) to (B.10), $g'(z)$, $w(z)$, and $b(z)$ of a top-hat plume can be derived, i.e.

$$g'(z) = \frac{5}{6\alpha}\left(\frac{10}{9\alpha}\right)^{\frac{1}{3}} \pi^{-\frac{2}{3}} F_s^{2/3} z^{-5/3}, \tag{B.21}$$

$$w(z) = \frac{5}{6\alpha}\left(\frac{9\alpha}{10}\right)^{\frac{1}{3}} \pi^{-\frac{1}{3}} F_s^{1/3} z^{-1/3}, \tag{B.22}$$

$$b(z) = \frac{6}{5}\alpha z. \tag{B.23}$$

Correspondingly, $w_c(z)$, $g'_c(z)$ and $b_G(z)$ of a Gaussian plume are obtained from (B.11) to (B.13) as follows

$$w_c(z) = \frac{5}{3\alpha} \left( \frac{9\alpha}{10} \right)^{\frac{1}{3}} \pi^{-\frac{1}{3}} F_s^{1/3} z^{-1/3}, \tag{B.24}$$

$$g'_c(z) = \frac{5}{3\alpha} \left( \frac{10}{9\alpha} \right)^{\frac{1}{3}} \pi^{-\frac{2}{3}} F_s^{2/3} z^{-5/3}, \tag{B.25}$$

$$b_G(z) = \frac{6}{5\sqrt{2}} \alpha z. \tag{B.26}$$

# Appendix C

# Discretization and Turbulence Model

Owing to the non-linear advection term, $(\vec{u} \cdot \nabla)\,\vec{u}$, it is impractical to seek analytical solutions to equation (4.3) in the scenario of a turbulent plume. Instead (4.3) is solved with numerical methods. For convenience and for now omitting the body force terms, the terms in (4.3) are rewritten using Einstein notation as

$$\frac{\partial u_i}{\partial t} + u_j \frac{\partial u_i}{\partial x_j} = \frac{1}{\rho_0}\frac{\partial p}{\partial x_i} + \nu \frac{\partial^2 u_i}{\partial x_j \partial x_j}. \qquad (C.1)$$

In numerical computation, the terms in equation (C.1) must be discretized. To give an example, $\frac{\partial u_i}{\partial t}$ can be discretized with the first order finite difference scheme as

$$\frac{\partial u_i}{\partial t} \approx \frac{u_i(t + \Delta t) - u_i(t)}{\Delta t} = \frac{1}{\Delta t}\int_t^{t+\Delta t}\frac{\partial u_i}{\partial t}\mathrm{d}t. \qquad (C.2)$$

Equation (C.2) illustrates that the discretization of the time derivative, $\frac{\partial u_i}{\partial t}$, is identical to a time average operation, $\frac{\int_t^{t+\Delta t}\frac{\partial u_i}{\partial t}\mathrm{d}t}{\Delta t}$, in the range of $[t, t + \Delta t]$. Similarly, the discretization of the spatial derivative term can be regarded as the spatial average in the range of $[x_j, x_j + \Delta x_j]$. Unfortunately, complications arise when computing averages of $u_j\frac{\partial u_i}{\partial x_j}$. Consequently, and as we explain next, special care is required when considering these nonlinear terms.

# Reynolds-Averaged Navier Stokes equation

An ensemble average is the average among a collection of experiments/realizations with identical conditions except for uncontrolled random noise. The ensemble average of a variable is denoted with a overline, e.g. $\overline{u}_i$. The instantaneous variable can be expressed as the sum the ensemble average and the fluctuation, i.e.

$$u_i = \overline{u}_i + u'_i,$$
$$p = \overline{p} + p',$$
(C.3)

where $u'_i$ and $p'$ are the fluctuations of velocity and pressure, respectively. It can be shown that

$$\overline{\overline{u}}_i = \overline{u}_i; \quad \overline{u'_i} = 0; \quad \overline{\overline{p}} = \overline{p}; \quad \overline{p'} = 0.$$
(C.4)

If a turbulent flow is statistically stationary[1], homogeneous, and isotropic, the ensemble average is equivalent to a temporal or spatial average over an infinitely large time or space interval, respectively (Kajishima & Taira, 2017). By extension, it is also assumed that the temporal or spatial average over a sufficiently large finite temporal or spatial interval is a reliable approximate to the ensemble average. Taking the ensemble average of (C.1), yields

$$\overline{\frac{\partial u_i}{\partial t}} + \overline{u_j \frac{\partial u_i}{\partial x_j}} = \overline{\frac{1}{\rho_0} \frac{\partial p}{\partial x_i}} + \overline{\nu \frac{\partial^2 u_i}{\partial x_j \partial x_j}}.$$
(C.5)

Substituting (C.3) into (C.5), yields

$$\overline{\frac{\partial \left(\overline{u}_i + u'_i\right)}{\partial t}} + \overline{\left(\overline{u}_j + u'_j\right) \frac{\partial \left(\overline{u}_i + u'_i\right)}{\partial x_j}} = \overline{\frac{1}{\rho_0} \frac{\partial \left(\overline{p} + p'\right)}{\partial x_i}} + \overline{\nu \frac{\partial^2 \left(\overline{u}_i + u'_i\right)}{\partial x_j \partial x_j}}.$$
(C.6)

The operation of differentiation can commute with the operation of ensemble averaging, which yields

$$\frac{\partial \overline{u}_i}{\partial t} + \overline{u}_j \frac{\partial \overline{u}_i}{\partial x_j} + \overline{u'_j \frac{\partial u'_i}{\partial x_j}} = \frac{1}{\rho_0} \frac{\partial \overline{p}}{\partial x_i} + \nu \frac{\partial^2 \overline{u}_i}{\partial x_j \partial x_j}.$$
(C.7)

As shown in (C.7), the fluctuation variables are eliminated in all the linear terms after averaging. However, this is not so with the nonlinear term because the

---

[1]A stationary process means the statistical properties of this process, such as mean, variance and autocorrelation, etc., do not change in time.

term $\overline{u'_j \frac{\partial u'_i}{\partial x_j}}$ remains. For a turbulent flow, the fluctuation term is comparable to other terms in (C.7) and thereby it is necessary to retain $\overline{u'_j \frac{\partial u'_i}{\partial x_j}}$ in order to simulate a realistic flow.

Taking ensemble averages in the continuity equation (4.1) and using Einstein notation, yields

$$\overline{\frac{\partial u_j}{\partial x_j}} = \overline{\frac{\partial \bar{u}_j + u'_j}{\partial x_j}} = \frac{\partial \bar{u}_j}{\partial x_j} + \frac{\partial \bar{u}'_j}{\partial x_j} = 0. \tag{C.8}$$

Because $\frac{\partial \bar{u}'_j}{\partial x_j} = 0$, we have

$$\frac{\partial \bar{u}_j}{\partial x_j} = 0, \tag{C.9}$$

and consequently

$$\frac{\partial u'_j}{\partial x_j} = 0. \tag{C.10}$$

Equations (C.9) and (C.10) state that both averaged and fluctuation velocities remain divergence-free. Multiplying (C.10) with $u'_i$ and taking the ensemble average, the result can then be added to the third term of (C.7), whereby

$$\frac{\partial \bar{u}_i}{\partial t} + \bar{u}_j \frac{\partial \bar{u}_i}{\partial x_j} = \frac{1}{\rho_0} \frac{\partial \bar{p}}{\partial x_i} + \nu \frac{\partial^2 \bar{u}_i}{\partial x_j \partial x_j} - \frac{\partial \overline{u'_i u'_j}}{\partial x_j}. \tag{C.11}$$

Here, the term $-\frac{\partial \overline{u'_i u'_j}}{\partial x_j}$ from the right hand side of (C.11) is moved from the left hand side of the original equation. The term in question term can be combined with the molecular viscous stress tensor term, $\nu \frac{\partial^2 \bar{u}_i}{\partial x_j \partial x_j}$, i.e. $\frac{\partial}{\partial x_j} \left( \nu \frac{\partial \bar{u}_i}{\partial x_j} - \overline{u'_i u'_j} \right)$. Because the variable $-\overline{u'_i u'_j}$ has a similar effect to the molecular viscous stress tensor, $\nu \frac{\partial \bar{u}_i}{\partial x_j}$, in (C.11), $-\overline{u'_i u'_j}$ is referred to as the Reynolds stress and (C.11) is known as the Reynolds-Averaged Navier Stokes equation (RANS).

Equation (C.11) was first derived by Reynolds (1895). For a fully 3D flow, the Reynolds stress introduces six additional unknowns, namely $\overline{u'_1 u'_1}$, $\overline{u'_2 u'_2}$, $\overline{u'_3 u'_3}$, $\overline{u'_1 u'_2}$, $\overline{u'_1 u'_3}$ and $\overline{u'_2 u'_3}$. In order to close the system, many efforts have been invested into modelling the Reynolds stress with mean flow quantities. Boussinesq (1877) proposed a linear relation between the Reynolds stress and the mean flow for an incompressible fluid as follows

$$-\overline{u'_i u'_j} = \nu_t \left( \frac{\partial \bar{u}_i}{\partial x_j} + \frac{\partial \bar{u}_j}{\partial x_i} \right) - \frac{2}{3} k \delta_{ij}. \tag{C.12}$$

114

Here $k = \frac{1}{2}\overline{u'_i u'_i}$ is the turbulent kinetic energy, $\delta_{ij}$ is the Kronecker delta function given by

$$\delta_{ij} = \begin{cases} 0 & \text{if } i \neq j, \\ 1 & \text{if } i = j, \end{cases} \tag{C.13}$$

and $\nu_t$ is referred to as the eddy viscosity, which should be obtained from separate analyses or treated as an empirical parameter.

Different models have been developed in order to formulate the eddy viscosity, $\nu_t$, in different turbulent flow scenarios. Such models can be categorized as zero-equation (Baldwin & Lomax, 1978; Johnson & King, 1985), one-equation (Baldwin & Barth, 1991; Spalart & Allmaras, 1992) and two-equation models (Jones & Launder, 1972; Launder & Sharma, 1974; Wilcox, 1988; Menter, 1993) according to the number of additional equations that must be considered when solving for $\nu_t$.

Among the two-equation models, $k$-$\epsilon$ is widely adopted in industry and implemented in most commercial CFD softwares. As above, $k$ stands for the turbulent kinetic energy and $\epsilon$ is the dissipation rate of $k$. This model was developed by Jones & Launder (1972) to simulate the phenomenon of laminarization found in turbulent boundary layers with high Reynolds number. Launder & Sharma (1974) revised this model and derived what is now considered to be the standard $k$-$\epsilon$ model.

Based on the first hypothesis in the paper by Kolmogorov (1941), the length scale, $\eta$, of the smallest eddy in turbulent flows with high Reynolds number can be determined from the kinematic viscosity, $\nu$, and the energy dispassion rate, $\epsilon$. At length scales less than $\eta$, the flow is dominated by molecular viscosity and the flow can therefore be regarded as laminar. Direct numerical simulations can solve the full Navier-Stokes equation if they can be run at spatial resolutions having the order of $\eta$ (Moin & Mahesh, 1998). However such high resolution can require prohibitively large memory and long computation times to produce a simulation of even modest duration.

# Large Eddy Simulation

To avoid the restrictions of DNS, researchers have developed Large Eddy Simulation (LES) to keep the fluctuating quantities in their simulations of turbulent flows while reducing computational costs. LES was first proposed by Smagorinsky (1963) to simulate the atmosphere's general circulation. The numerical method has since been refined by many others including (Lilly, 1967; Deardorff, 1974; Schumann, 1975; Bardina *et al.*, 1980; Yoshizawa, 1986; Meneveau *et al.*, 1996). Review papers about LES have been written by Mason (1994) and Yang (2015).

In RANS, ensemble averages are used in (C.1) to yield (C.5). For a statistically steady turbulent flow, RANS effectively filters all the fluctuating properties of the turbulent flow in the temporal space. In this regard, the concept behind LES is to filter (C.1) in space rather than in time. Furthermore, LES only filters the variables in (C.1) with smaller scales than $\Delta x_i$, while it allows fluctuations with large spatial scales (like large eddies) to remain unchanged in the solutions. In fact, motions with small spatial scales typically also have small temporal scales, and therefore LES indirectly filters fluctuations with high frequencies. Similar to (C.3), in LES $u_i$ and $p$ can be separated to filtered parts and fluctuating parts as

$$u_i = \langle u_i \rangle + u_i', \\ p = \langle p \rangle + p'. \tag{C.14}$$

Here the filtered parts are denoted by the angled brackets, $\langle \rangle$, and the fluctuating parts are still denoted with primes, $'$. Substituting (C.14) into (C.1) and applying a filter operation to the resulting equation (Kajishima & Taira, 2017), yields

$$\frac{\partial \langle u_i \rangle}{\partial t} + \langle u_j \rangle \frac{\partial \langle u_i \rangle}{\partial x_j} = -\frac{1}{\rho_0} \frac{\partial \langle p \rangle}{\partial x_i} + \nu \frac{\partial^2 \langle u_i \rangle}{\partial x_j \partial x_j} + \frac{\partial \tau_{ij}}{\partial x_j}. \tag{C.15}$$

Here $\tau_{ij}$ is the residual stress that results from filtering the non-linear term, and is given by

$$\tau_{ij} = - \left( \langle u_i u_j \rangle - \langle u_i \rangle \langle u_j \rangle \right). \tag{C.16}$$

The residual stress, $\tau_{ij}$, equals $- \langle u_i' u_j' \rangle$ only if the filter is a Reynolds operator,

see Sagaut *et al.* (2006) for the definition. The effects of the small scale processes on the large scale motions are represented by $\tau_{ij}$ and are accounted for numerically using any one of a number of subgrid-scale (SGS) models. Among the common SGS models are the eddy viscosity model (Smagorinsky, 1963), dynamic model (Germano, 1992), similarity model (Bardina *et al.*, 1980) and one-equation viscosity model (Yoshizawa & Horiuti, 1985).

LES simulations applied to plumes are very sensitive to the inlet boundary condition of velocity, which is expected to have temporal and spatial correlations on the inlet boundary. Tabor & Baba-Ahmadi (2010) summarized the common methods for generating inlet boundary conditions for LES simulations. These can be categorized into two types: synthesis methods and precursor methods. The former superimpose the mean flow at the inlet boundary with some artificial fluctuations containing some spatial and temporal correlations. For the precursor methods, an additional simulation is performed separately and the data are stored to be used as the inflow boundary conditions for the LES simulations.

# References

BAINES, P. G. & SPARKS, R. S. J. 2005 Dynamics of giant volcanic ash clouds from supervolcanic eruptions. *Geophys. Res. Lett.* **32** (24), l24808.

BAINES, W. D. 1975 Entrainment by a plume or jet at a density interface. *J. Fluid Mech.* **68** (2), 309–320.

BAINES, W. D. 1983 A technique for the direct measurement of volume flux of a plume. *J. Fluid Mech.* **132**, 247–256.

BAINES, W. D., CORRIVEAU, A. F. & REEDMAN, T. J. 1993 Turbulent fountains in a closed chamber. *J. Fluid Mech.* **255**, 621–646.

BAINES, W. D. & TURNER, J. S. 1969 Turbulent buoyant convection from a source in a confined region. *J. Fluid Mech.* **37**, 51–80.

BALDWIN, B. & BARTH, T. 1991 A one-equation turbulence transport model for high reynolds number wall-bounded flows. In *29th Aerospace Sciences Meeting*. American Institute of Aeronautics and Astronautics.

BALDWIN, B. & LOMAX, H. 1978 Thin-layer approximation and algebraic model for separated turbulentflows. In *16th Aerospace Sciences Meeting*. American Institute of Aeronautics and Astronautics.

BARDINA, J., FERZIGER, J. & REYNOLDS, W. 1980 Improved subgrid-scale models for large-eddy simulation. In *13th Fluid and PlasmaDynamics Conference*. American Institute of Aeronautics and Astronautics.

BLOOMFIELD, L. J. & KERR, R. C. 1998 Turbulent fountains in a stratified fluid. *J. Fluid Mech.* **358**, 335–356.

BLOOMFIELD, L. J. & KERR, R. C. 2000 A theoretical model of a turbulent fountain. *J. Fluid Mech.* **424**, 197–216.

BLUTH, G. J. S., DOIRON, S. D., SCHNETZLER, CHARLES, C., KRUEGER, A. J. & WALTER, L. S. 1992 Global tracking of the so2 clouds from the june, 1991 mount pinatubo eruptions. *Geophys. Res. Lett.* **19** (2), 151–154.

BOLSTER, D., MAILLARD, A. & LINDEN, P. F. 2008 The response of natural displacement ventilation to time-varying heat sources. *Energ. Buildings* **40**, 2099–2110.

BOUSSINESQ, J. 1877 *Essai sur la théorie des eaux courantes*. Imprimerie Nationale.

BRITTER, R. 1979 The spread of a negatively buoyant plume in a calm environment. *Atmos. Environ.* **13** (9), 1241 – 1247.

BURRIDGE, H. C., PARKER, D. A., KRUGER, E. S., PARTRIDGE, J. L. & LINDEN, P. F. 2017 Conditional sampling of a high péclet number turbulent plume and the implications for entrainment. *J. Fluid Mech.* **823**, 26–56.

CAMASSA, R., LIN, Z., MCLAUGHLIN, R. M., MERTENS, K., TZOU, C., WALSH, J. & WHITE, B. 2016 Optimal mixing of buoyant jets and plumes in stratified fluids: theory and experiments. *J. Fluid Mech.* **790**, 71–103.

CARAZZO, G., KAMINSKI, E. & TAIT, S. 2006 The route to self-similarity in turbulent jets and plumes. *J. Fluid Mech.* **547**, 137–148.

CARLOTTI, P. & HUNT, G. R. 2017 An entrainment model for lazy turbulent plumes. *J. Fluid Mech.* **811**, 682–700.

CAULFIELD, C. P. & WOODS, A. W. 2002 The mixing in a room by a localized finite-mass-flux source of buoyancy. *J. Fluid Mech.* **471**, 33–50.

CHAUHAN, K., PHILIP, J., DE SILVA, C. M., HUTCHINS, N. & MARUSIC, I. 2014 The turbulent/non-turbulent interface and entrainment in a boundary layer. *J. Fluid Mech.* **742**, 119–151.

CHEN, L. F., ZANG, J., HILLIS, A. J., MORGAN, G. C. J. & PLUMMER, A. R. 2014 Numerical investigation of wave–structure interaction using openfoam. *Ocean Eng.* **88**, 91–109.

CLARKE, R. A. & GASCARD, J.-C. 1983 The formation of labrador sea water. part i: Large-scale processes. *J. Phys. Oceanogr.* **13** (10), 1764–1778.

COOPER, P. & LINDEN, P. F. 1996 Natural ventilation of an enclosure containing two buoyancy sources. *J. Fluid Mech.* **311**, 153–176.

CORTÉS, A., RUEDA, F. J. & WELLS, M. G. 2014 Experimental observations of the splitting of a gravity current at a density step in a stratified water body. *J. Geophys. Res.: Oceans* **119** (2), 1038–1053.

COURTOIS, P., HU, X., PENNELLY, C., SPENCE, P. & MYERS, P. G. 2017 Mixed layer depth calculation in deep convection regions in ocean numerical models. *Ocean Model.* **120**, 60–78.

DA SILVA, C. B., HUNT, J. C. R., EAMES, I. & WESTERWEEL, J. 2014 Interfacial layers between regions of different turbulence intensity. *Annu. Rev. Fluid Mech.* **46** (1), 567–590.

DAI, Z., TSENG, L.-K. & FAETH, G. M. 1994 Structure of round, fully developed, buoyant turbulent plumes. *J. Heat Transfer* **116** (2), 409.

DAVIERO, G. J. & ROBERTS, P. J. 2006 Marine wastewater discharges from multiport diffusers. iii: Stratified stationary water. *J. Hydraul. Eng.* **132** (4), 404–410.

DEARDORFF, J. W. 1974 Three-dimensional numerical study of the height and mean structure of a heated planetary boundary layer. *Bound.-Lay. Meteorol.* **7** (1), 81–106.

DEVENISH, B. J., ROONEY, G. G. & THOMSON, D. J. 2010 Large-eddy simulation of a buoyant plume in uniform and stably stratified environments. *J. Fluid Mech.* **652**, 75–103.

120

EZZAMEL, A., SALIZZONI, P. & HUNT, G. R. 2015 Dynamical variability of axisymmetric buoyant plumes. *J. Fluid Mech.* **765**, 576–611.

FABREGAT TOMÀS, A., POJE, A. C., ÖZGÖKMEN, T. M. & DEWAR, W. K. 2016 Effects of rotation on turbulent buoyant plumes in stratified environments. *J. Geophys. Res.: Oceans* **121** (8), 5397–5417.

FERNANDO, H. J. S., CHEN, R.-R. & AYOTTE, B. A. 1998 Development of a point plume in the presence of background rotation. *Phys. Fluids* **10** (9), 2369–2383.

FLYNN, M. R. & CAULFIELD, C. P. 2006 Natural ventilation in interconnected chambers. *J. Fluid Mech.* **564**, 139–158.

FOX, D. G. 1970 Forced plume in a stratified fluid. *J. Geophys. Res.* **75** (33), 6818–6835.

FRANK, D., LANDEL, J. R., DALZIEL, S. B. & LINDEN, P. F. 2017 Anticyclonic precession of a plume in a rotating environment. *Geophys. Res. Lett.* **44** (18), 9400–9407, 2017GL074191.

GEORGE, W. K., ALPERT, R. L. & TAMANINI, F. 1977 Turbulence measurements in an axisymmetric buoyant plume. *Int. J. Heat and Mass Transfer* **20** (11), 1145 – 1154.

GERMAN, C. & SEYFRIED, W. 2013 *Hydrothermal Processes*, , vol. 8, pp. 191–233. Elsevier Inc.

GERMANO, M. 1992 Turbulence: the filtering approach. *J. Fluid Mech.* **238**, 325–336.

GERMELES, A. E. 1975 Forced plumes and mixing of liquids in tanks. *J. Fluid Mech.* **71**, 601–623.

GRIFFITHS, R. W. & LINDEN, P. F. 1981 The stability of vortices in a rotating, stratified fluid. *J. Fluid Mech.* **105**, 283–316.

HALLWORTH, M., HUPPERT, H. & UNGARISH, M. 2001 Axisymmetric gravity currents in a rotating system: experimental and numerical investigations. *J. Fluid Mech.* **447**, 1–29.

HELFRICH, K. R. 1994 Thermals with background rotation and stratification. *J. Fluid Mech.* **259**, 265–280.

HELFRICH, K. R. & BATTISTI, T. M. 1991 Experiments on baroclinic vortex shedding from hydrothermal plumes. *J. Geophys. Res.: Oceans* **96** (C7), 12511–12518.

HIGUERA, P., LIU, P. L. F., LIN, C., WONG, W. Y. & KAO, M. J. 2018 Laboratory-scale swash flows generated by a non-breaking solitary wave on a steep slope. *J. Fluid Mech.* **847**, 186–227.

HOLDSWORTH, A. M. & MYERS, P. G. 2015 The influence of high-frequency atmospheric forcing on the circulation and deep convection of the labrador sea. *J. Climate* **28** (12), 4980–4996.

HUANG, S. & LI, Q. S. 2009 A new dynamic one-equation subgrid-scale model for large eddy simulations. *Int. J. Numer. Methods Eng.* **81** (7), 835–865.

HUGHES, G. O. & GRIFFITHS, R. W. 2006 A simple convective model of the global overturning circulation, including effects of entrainment into sinking regions. *Ocean Model.* **12** (1), 46–79.

HUNT, C. D., MANSFIELD, A. D., MICKELSON, M. J., ALBRO, C. S., GEYER, W. R. & ROBERTS, P. J. 2010 Plume tracking and dilution of effluent from the boston sewage outfall. *Mar. Environ. Res.* **70** (2), 150 – 161.

HUNT, C. D., MANSFIELD, A. D., ROBERTS, P. J. W., ALBRO, C. A., GEYER, W. R., STEINHAUER, W. S. & MICKELSON, M. J. 2002 Massachusetts water resources authority outfall effluent dilution: July 2001. *Tech. Rep.* ENQUAD 2002-07. Boston: Massachusetts Water Resources Authority.

HUNT, G. R. & KAYE, N. G. 2001 Virtual origin correction of lazy turbulent plumes. *J. Fluid Mech.* **435**, 377–396.

HUNT, G. R. & LINDEN, P. F. 2001 Steady-state flows in an enclosure ventilated by buoyancy forces assisted by wind. *J. Fluid Mech.* **426**, 355–386.

JOHNSON, D. A. & KING, L. S. 1985 A mathematically simple turbulence closure model for attached and separated turbulent boundary layers. *AIAA J.* **23** (11), 1684–1692.

JONES, H. & MARSHALL, J. 1993 Convection with rotation in a neutral ocean: A study of open-ocean deep convection. *J. Phys. Oceanogr.* **23** (6), 1009–1039.

JONES, W. & LAUNDER, B. 1972 The prediction of laminarization with a two-equation model of turbulence. *Int. J. Heat Mass Transf.* **15** (2), 301 – 314.

JULIEN, K., LEGG, S., MCWILLIAMS, J. & WERNE, J. 1999 Plumes in rotating convection. Part 1. Ensemble statistics and dynamical balances. *J. Fluid Mech.* **391**, 151–187.

KAJISHIMA, T. & TAIRA, K. 2017 *Large-Eddy Simulation*, pp. 269–307. Cham: Springer International Publishing.

KAYE, N. B. & FLYNN, M. R. 2012 Flow through buildings. In *Handbook of Environmental Fluid Dynamics, Volume Two: Systems, Pollution, Modelling, and Measurements* (ed. H. J. S. Fernando), pp. 97–109. Boca Raton, FL: CRC Press.

KAYE, N. B. & HUNT, G. R. 2004 Time-dependent flows in an emptying filling box. *J. Fluid Mech.* **520**, 135–156.

KAYE, N. B. & HUNT, G. R. 2007 Overturning in a filling box. *J. Fluid Mech.* **576**, 297–323.

KOLMOGOROV, A. N. 1941 The Local Structure of Turbulence in Incompressible Viscous Fluid for Very Large Reynolds Numbers. *C. R. Acad. Sci. URSS* **30**, 301–305.

Kotsovinos, N. E. 1975 A study of the entrainment and turbulence in a plane buoyant jet. PhD thesis, California Institute of Technology.

Kulkarni, A., Murphy, F. & Manohar, S. 1993 Interaction of buoyant plumes with two-layer stably stratified media. *Exp. Therm. Fluid Sci.* **7** (3), 241 – 248.

Kumagai, M. 1984 Turbulent buoyant convection from a source in a confined two-layered region. *J. Fluid Mech.* **147**, 105–131.

Kumar, R. & Dewan, A. 2014 Urans computations with buoyancy corrected turbulence models for turbulent thermal plume. *Int. J. Heat Mass Transf.* **72**, 680–689.

Lagzi, I., Mészáros, R., Gelybó, G. & Leelőssy, A. 2013 *Atmospheric Chemistry*. Eötvös Loránd University.

Launder, B. & Sharma, B. 1974 Application of the energy-dissipation model of turbulence to the calculation of flow near a spinning disc. *Lett. Heat Mass Trans.* **1** (2), 131 – 137.

Lee, S.-L. & Emmons, H. W. 1961 A study of natural convection above a line fire. *J. Fluid Mech.* **11**, 353–368.

Lilly, D. K. 1967 The representation of small scale turbulence in numerical simulation experiments. In *IBM Scientific Computing Symposium on environmental sciences*, pp. 195–210. Yorktown heights.

Lin, Y. J. P. & Linden, P. F. 2005 The entrainment due to a turbulent fountain at a density interface. *J. Fluid Mech.* **542**, 25–52.

Linden, P. F. 1999 The fluid mechanics of natural ventilation. *Annu. Rev. Fluid Mech.* **31** (1), 201–238.

Linden, P. F. & Cooper, P. 1996 Multiple sources of buoyancy in a naturally ventilated enclosure. *J. Fluid Mech.* **311**, 177–192.

LINDEN, P. F. & KAYE, N. B. 2006 Interacting turbulent plumes in a naturally ventilated enclosure. *Int. J. Vent.* **4** (4), 301–310.

LINDEN, P. F., LANE-SERFF, G. F. & SMEED, D. A. 1990 Emptying filling boxes: the fluid mechanics of natural ventilation. *J. Fluid Mech.* **212**, 309–335.

LOZIER, M. S. 2011 Overturning in the north atlantic. *Annu. Rev. Mar. Sci.* **4** (1), 291–315.

LYSENKO, D. A., ERTESVAG, I. S. & RIAN, K. E. 2012 Large-Eddy Simulation of the Flow Over a Circular Cylinder at Reynolds Number 3900 Using the OpenFOAM Toolbox. *Flow Turbul. Combust.* **89** (4), 491–518.

LYSENKO, D. A., ERTESVÅG, I. S. & RIAN, K. E. 2013 Modeling of turbulent separated flows using openfoam. *Comput. Fluids* **80**, 408–422.

MA, Y., FLYNN, M. R. & SUTHERLAND, B. R. 2017 Convection from a line-source into a two-layer stratified ambient fluid. *J. Fluid Mech.* **818**, 46–67.

MARSHALL, J. & SCHOTT, F. 1999 Open-ocean convection: Observations, theory, and models. *Rev. Geophys.* **37** (1), 1–64.

MASON, P. J. 1994 Large-eddy simulation: A critical review of the technique. *Q. J. Roy. Meteorol. Soc.* **120** (515), 1–26.

MATHEW, J. & BASU, A. 2002 Some characteristics of entrainment at a cylindrical turbulence boundary. *Phys. Fluids* **14** (7), 2065–2072.

MCNUTT, M., CAMILLI, R., GUTHRIE, G., HSIEH, P., LABSON, V., LEHR, W., MACLAY, D., RATZEL, A. & SOGGE, M. 2011 *Assessment of Flow Rate Estimates for the Deepwater Horizon/Macondo Well Oil Spill*. U.S. Department of the Interior.

MENEVEAU, C., LUND, T. S. & CABOT, W. H. 1996 A lagrangian dynamic subgrid-scale model of turbulence. *J. Fluid Mech.* **319**, 353–385.

MENTER, F. 1993 Zonal two equation k-w turbulence models for aerodynamic flows. In *23rd Fluid Dynamics, Plasmadynamics, and Lasers Conference*. American Institute of Aeronautics and Astronautics.

MOIN, P. & MAHESH, K. 1998 Direct numerical simulation: A tool in turbulence research. *Annu. Rev. Fluid Mech.* **30** (1), 539–578.

MORTON, B. R. 1957 Buoyant plumes in a moist atmosphere. *J. Fluid Mech.* **2** (2), 127–144.

MORTON, B. R. 1959 Forced plumes. *J. Fluid Mech.* **234**, 1–23.

MORTON, B. R., TAYLOR, G. I. & TURNER, J. S. 1956 Turbulent gravitational convection from maintained and instantaneous sources. *Proc. Roy. Soc. A* **234**, 1–23.

MOTT, R. W. & WOODS, A. W. 2009 On the mixing of a confined stratified fluid by a turbulent buoyant plume. *J. Fluid Mech.* **623**, 149–165.

MULLARNEY, J. C., GRIFFITHS, R. W. & HUGHES, G. O. 2004 Convection driven by differential heating at a horizontal boundary. *J. Fluid Mech.* **516**, 181–209.

MUNK, W. H. 1966 Abyssal recipes. *Deep-Sea Res.* **13**, 707–730.

NOH, Y., FERNANDO, H. J. S. & CHING, C. Y. 1992 Flows induced by the impingement of a two-dimensional thermal on a density interface. *J. Phys. Oceanogr.* **22** (10), 1207–1220.

OKADA, N., IKEDA, M. & MINOBE, S. 2004 Numerical experiments of isolated convection under polynya. *J. Oceanogr.* **60** (6), 927–943.

PAILLAT, S. & KAMINSKI, E. 2014 Entrainment in plane turbulent pure plumes. *J. Fluid Mech.* **755**.

PHAM, M. V., PLOURDE, F. & DOAN, K. S. 2007 Direct and large-eddy simulations of a pure thermal plume. *Phys. Fluids* **19** (12), 125103.

PLOURDE, F., PHAM, M. V., KIM, S. D. & BALACHANDAR, S. 2008 Direct numerical simulations of a rapidly expanding thermal plume: structure and entrainment interaction. *J. Fluid Mech.* **604**, 99–123.

RAMAPRIAN, B. R. & CHANDRASEKHARA, M. S. 1989 Measurements in vertical plane turbulent plumes. *J. Fluids Eng.* **111** (1), 69–77.

VAN REEUWIJK, M. & HOLZNER, M. 2014 The turbulence boundary of a temporal jet. *J. Fluid Mech.* **739**, 254–275.

VAN REEUWIJK, M., SALIZZONI, P., HUNT, G. R. & CRASKE, J. 2016 Turbulent transport and entrainment in jets and plumes: A dns study. *Phys. Rev. Fluids* **1** (7), 074301–.

REYNOLDS, O. 1895 On the dynamical theory of incompressible viscous fluids and the determination of the criterion. *Philos. Trans. Royal Soc. A: Mathematical, Physical and Engineering Sciences* **186**, 123–164.

RICHARDS, T. S., AUBOURG, Q. & SUTHERLAND, B. R. 2014 Radial intrusions from turbulent plumes in uniform stratification. *Phys. Fluids* **26** (3), 036602.

ROBERTS, P. J. W., HUNT, C. D., MICKELSON, M. J. & TIAN, X. 2011 Field and model studies of the boston outfall. *J. Hydraul. Eng.* **137** (11), 1415–1425.

ROBOCK, A. 2000 Volcanic eruptions and climate. *Rev. Geophys.* **38** (2), 191–219.

ROES, M. A. 2014 Buoyancy-driven convection in a ventilated porous medium. Master's thesis, Univ. of Alberta.

ROOHI, E., ZAHIRI, A. P. & PASSANDIDEH-FARD, M. 2013 Numerical simulation of cavitation around a two-dimensional hydrofoil using vof method and les turbulence model. *Appl. Math. Model.* **37** (9), 6469–6488.

SAGAUT, P., MENEVEAU, C. & SAGAUT, P. 2006 *Large Eddy Simulation for Incompressible Flows : An Introduction*. Berlin, Heidelberg, GERMANY: Springer.

SCHUMANN, U. 1975 Subgrid scale model for finite difference simulations of turbulent flows in plane channels and annuli. *J. Comput. Phys.* **18** (4), 376 – 404.

SHRINIVAS, A. B. & HUNT, G. R. 2014 Unconfined turbulent entrainment across density interfaces. *J. Fluid Mech.* **757**, 573–598.

SMAGORINSKY, J. 1963 General circulation experiments with the primitive equations. *Mon. Weather Rev.* **91** (3), 99–164.

SPALART, P. & ALLMARAS, S. 1992 A one-equation turbulence model for aerodynamic flows. In *30th Aerospace Sciences Meeting and Exhibit*. American Institute of Aeronautics and Astronautics.

SPEER, K. & MARSHALL, J. 1995 The growth of convective plumes at sea-floor hot-springs. *J. Mar. Res.* **53** (6), 1025–1057.

SREENIVAS, K. R. & PRASAD, A. K. 2000 Vortex-dynamics model for entrainment in jets and plumes. *Phys. Fluids* **12** (8), 2101–2107.

STEIN, C. A. & STEIN, S. 1994 Constraints on hydrothermal heat flux through the oceanic lithosphere from global heat flow. *J. Geophys. Res.: Solid Earth* **99** (B2), 3081–3095.

SUZUKI, Y. J., COSTA, A., CERMINARA, M., ESPOSTI ONGARO, T., HERZOG, M., VAN EATON, A. R. & DENBY, L. C. 2016 Inter-comparison of three-dimensional models of volcanic plumes. *J. Volcanol. Geotherm. Res.* **326**, 26–42.

TABOR, G. & BABA-AHMADI, M. 2010 Inlet conditions for large eddy simulation: A review. *Comput. Fluids* **39** (4), 553 – 567.

TATE, P. M., SCATURRO, S. & CATHERS, B. 2016 *Marine Outfalls*, pp. 711–740. Cham: Springer International Publishing.

TIAN, X., ROBERTS, P. J. & DAVIERO, G. J. 2006 Marine wastewater discharges from multiport diffusers. iv: Stratified flowing water. *J. Hydraul. Eng.* **132** (4), 411–419.

TURNER, J. S. 1986 Turbulent entrainment: the development of the entrainment assumption, and its application to geophysical flows. *J. Fluid Mech.* **173**, 431–471.

UNGARISH, M. & HUPPERT, H. 1998 The effects of rotation on axisymmetric gravity currents. *J. Fluid Mech.* **362**, 17–51.

WALLACE, R. B. & SHEFF, B. B. 1987 Two-dimensional buoyant jets in two-layer ambient fluid. *J. Hydraul. Eng.* **113** (8), 992–1005.

WANG, Y., CHATTERJEE, P. & DE RIS, J. L. 2011 Large eddy simulation of fire plumes. *P. Combust. Inst.* **33** (2), 2473–2480.

WELLS, M. G. & WETTLAUFER, J. S. 2007 The long-term circulation driven by density currents in a two-layer stratified basin. *J. Fluid Mech.* **572**, 37–58.

WESTERWEEL, J., FUKUSHIMA, C., PEDERSEN, J. M. & HUNT, J. C. R. 2005 Mechanics of the turbulent-nonturbulent interface of a jet. *Phys. Rev. Lett.* **95**, 174501.

WHITE, J. D. L., SCHIPPER, C. I., KANO, K. & SIGURDSSON, H. 2015 *Chapter 31 - Submarine Explosive Eruptions*, pp. 553–569. Amsterdam: Academic Press.

WILCOX, D. C. 1988 Reassessment of the scale-determining equation for advanced turbulence models. *AIAA J.* **26** (11), 1299–1310.

WILSON, T. M., JENKINS, S., STEWART, C., SHRODER, J. F. & PAPALE, P. 2015 *Chapter 3 - Impacts from Volcanic Ash Fall*, pp. 47–86. Boston: Elsevier.

WOODS, A. W. 2010 Turbulent plumes in nature. *Annu. Rev. Fluid Mech.* **42**, 391–412.

WORSTER, M. G. & HUPPERT, H. E. 1983 Time-dependent density profiles in a filling box. *J. Fluid Mech.* **132**, 457–466.

YAMAMOTO, H., CENEDESE, C. & CAULFIELD, C. P. 2011 Laboratory experiments on two coalescing axisymmetric turbulent plumes in a rotating fluid. *Phys. Fluids* **23** (5), 056601.

YANG, D., CHEN, B., SOCOLOFSKY, S. A., CHAMECKI, M. & MENEVEAU, C. 2016*a* Large-eddy simulation and parameterization of buoyant plume dynamics in stratified flow. *J. Fluid Mech.* **794**, 798–833.

YANG, Q., DIXON, T. H., MYERS, P. G., BONIN, J., CHAMBERS, D., VAN DEN BROEKE, M. R., RIBERGAARD, M. H. & MORTENSEN, J. 2016*b* Recent increases in arctic freshwater flux affects labrador sea convection and atlantic overturning circulation. *Nat. Commun.* **7**, 10525 EP –.

YANG, Z. 2015 Large-eddy simulation: Past, present and the future. *Chinese J. Aeronaut.* **28** (1), 11 – 24.

YASHAYAEV, I. & LODER, J. W. 2009 Enhanced production of Labrador Sea Water in 2008. *Geophys. Res. Lett.* **36** (1), l01606.

YOSHIZAWA, A. 1986 Statistical theory for compressible turbulent shear flows, with the application to subgrid modeling. *Phys. Fluids* **29** (7), 2152–2164.

YOSHIZAWA, A. & HORIUTI, K. 1985 A statistically-derived subgrid-scale kinetic energy model for the large-eddy simulation of turbulent flows. *J. Phys. Soc. Jpn.* **54** (8), 2834–2839.

YUANA, L.-M. & COX, G. 1996 An experimental study of some line fires. *Fire Saf. J.* **27** (2), 123 – 139.

ZENG, Q., GONZALEZ-AVILA, S. R., VOORDE, S. T. & OHL, C.-D. 2018 Jetting of viscous droplets from cavitation-induced rayleigh–taylor instability. *J. Fluid Mech.* **846**, 916–943.

Zhou, X., Luo, K. H. & Williams, J. J. 2001 Large-eddy simulation of a turbulent forced plume. *Eur. J. Mech.* **20** (2), 233 – 254.